Constraining Weakly Interacting Slim Particles with a Massive Star and in the Laboratory

Dissertation

zur Erlangung des Doktorgrades

des Department Physik

der Universität Hamburg

vorgelegt von

Jan Eike von Seggern

aus Delmenhorst

Hamburg

2013

Gutachter der Dissertation:	Prof. Dr. Dieter Horns Dr. Axel Lindner
Gutachterin/Gutachter der Disputation:	Prof. Dr. Erika Garutti Prof. Dr. Dieter Horns
Datum der Disputation:	16. Januar 2014
Vorsitzender des Prüfungsausschusses:	Dr. Georg Steinbrück
Vorsitzender des Promotionsausschusses:	Prof. Dr. Peter Hauschildt
Dekan:	Prof. Dr. Heinrich Graener

Abstract

This doctoral thesis is devoted to constraining the allowed parameter space of weakly interacting slim particles (WISPs). WISPs are predicted by many extensions of the Standard Model of Particle Physics (SM): The Peccei-Quinn solution of the strong CP-problem of quantum chromo dynamics requires the existence of an axion; some embeddings of the SM into string theories predict a large number of axion-like particles (ALPs), the so called axi-verse, and hidden photons (HPs). Cosmological and astrophysical observables are sensitive to the existence of WISPs. Measurements of these observables allow to constrain the allowed WISP parameter space. In addition dedicated laboratory based experiments exist. Although the parameter space excluded by these experiments is generally smaller than the regions excluded by measurements of cosmological or astrophysical observables, the results from these experiment are valuable complements to these measurements because they are less model dependent.

In this thesis, I present my work that helps to constrain the WISP parameter space in two ways: First, the existence of ALPs implies their production in stellar cores. The oscillation of ALPs with photons in the galactic magnetic field (GMF) suggest an X-ray flux from red supergiant (RSG) stars. RSGs are expected to emit no X-rays if ALPs do not exist. An upper limit for the X-ray count rate from the nearby RSG α-Ori (Betelgeuse) is estimated from observations of α-Ori with the Chandra X-ray Telescope. The interior of α-Ori is modelled with the "Evolve ZAMS" code. Based on this, the corresponding ALP production rate is calculated. Using current estimates of the value of the regular component of the GMF, the resulting X-ray flux density at Earth from ALP-photon oscillations and the corresponding count rates with the Chandra instruments are calculated. Comparison of this estimate with the upper limit from the Chandra measurements allows to exclude values of the ALP-photon coupling above $2.1 \times 10^{-11}\,\mathrm{GeV}^{-1}$ for masses below $2.6 \times 10^{-11}\,\mathrm{eV}$.

Second, a CCD (PI 1024B) camera is characterized in preparation of the "Any Light Particle Search II" experiment (ALPS-II), which is a "light shining through a wall" experiment searching for WISPs that is currently under preparation at DESY in Hamburg. This characterization includes the measurement of the fixed pattern noise (FPN), the read-out noise and dark count rate. It is found that clock-induced charges cause a spatial variation of the FPN and the read-out noise over the CCD chip area. The dark count rate is found to spatially vary, too, which is caused by a non-uniform thermal load on the CCD chip. In addition the quantum efficiency at 1064 nm, the wavelength used in ALPS-II, is measured to be 1.2 %.

Based on these results, an analysis algorithm for the CCD data is developed and the sensitivity of ALPS-II if using the CCD is compared to the sensitivity if the experiment uses a transition edge sensor (TES) as detector as planned. I find that the sensitivity with CCD on the ALP-photon coupling is one order of magnitude worse than the sensitivity with TES. This deterioration of the sensitivity is caused in equal parts by the lower quantum efficiency and higher dark count rate of the CCD compared to the TES.

Zusammenfassung

In dieser Arbeit wird der erlaubte Parameterraum für schwach wechselwirkende, leichte Teilchen (WISP) eingeschränkt. WISP werden von vielen Erweiterungen des Standardmodells der Teilchenphysik (SM) vorhergesagt: Die Lösung des starken CP-Problems durch Peccei und Quinn verlangt die Existenz eines Axions; Einbettungen des SM in Stringtheorien sagen eine Reihe von Axion-artigen Teilchen (ALPs), das sogenannte Axiversum, und versteckter Photonen (HPs) vorher. Kosmologische und astrophysikalische Observablen sind sensitiv auf die Existenz von WISPs. Messungen dieser Observablen ermöglichen es den erlaubten WISP-Parameterraum einzugrenzen. Zusätzlich gibt es Laborexperimente. Der von Laborexperimenten ausgeschlossene Parameterraum ist meistens kleiner als die Bereiche, die durch Messungen von kosmologischen und astrophysikalischen Observablen ausgeschlossen werden können. Die Ergebnisse von Laborexperimenten sind aber dennoch sehr wertvolle Ergänzungen zu diesen Messungen, da sie weniger modellabhängig sind.

Ich stelle in dieser Arbeit meine Ergebnisse vor, die auf zwei Weisen helfen, den WISP-Parameterraum einzugrenzen: Erstens bedingt die Existenz von ALPs, dass diese in Kernen von Sternen produziert werden. Im galaktischen Magnetfeld (GMF) oszillieren diese ALPs mit Photon, so dass Sterne, die ohne ALPs keine Röntgenstrahlung emittieren wie z.B. rote Superriesen, im Röntgenbereich sichtbar sein sollten. Aus Beobachtungen des nahen roten Superriesen α-Ori (Beteigeuze) mit dem Chandra Röntgenteleskop werden obere Grenzen auf die Zählraten von Röntgenphotonen von α-Ori mit den Chandra Beobachtungsinstrumenten abgeleitet. Der innere Aufbau von α-Ori wird mit Hilfe des "Evolve ZAMS" Programms simuliert. Basierend auf dieser Simulation wird die Rate der produzierten ALPs berechnet. Unter Verwendung von Abschätzungen der Feldstärke des GMF wird die Flussdichte von Röntgenphotonen auf Grund von ALP-Photon Oszillationen berechnet und die daraus resultierende Zählrate mit den Chandra Beobachtungsinstrumenten abgeschätzt. Der Vergleich dieser Abschätzung mit der oberen Grenze auf die Zählrate erlaubt es Werte für die ALP-Photon Kopplung oberhalb von $2.1 \times 10^{-11}\,\mathrm{GeV}^{-1}$ auszuschließen.

Zweitens wird zur Vorbereitung des "Any Light Particle Search II" Experiments (ALPS-II) eine CCD Kamera (PI 1024B) charakterisiert. ALPS-II is ein "Licht durch die Wand" Experiment, das gegenwärtig am DESY in Hamburg vorbereitet wird. Die Charakterisierung umfasst die Messung des fixed pattern noise (FPN), des Ausleserauschens und der Dunkelzählrate. Dabei stellt sich heraus, dass FPN und Ausleserauschen auf Grund von clock-induced charges auf der Chipfläche der CCD unterschiedlich sind. Die Dunkelzählrate ist ebenfalls über die Chipfläche unterschiedlich, was durch eine ungleichmäßige thermische Last auf den CCD Chip verursacht wird. Zusätzlich wird die Quanteneffizienz bei 1064 nm, der in ALPS-II verwendeten Wellenlänge, bestimmt (1.2 %).

Anhand dieser Ergebnisse wird ein Algorithmus für die Analyse der CCD Daten entwickelt. Die Sensitivität von ALPS-II mit der CCD als Detektor wird mit der Sensitivität mit einem Übergangskantensensor (TES) verglichen. Die Sensitivität mit der CCD ist eine Größenordnung schlechter als die Sensitivität mit TES. Diese Verschlechterung ist zu gleichen Teilen durch die geringere Quanteneffizienz und höhere Dunkelzählrate der CCD im Vergleich mit dem TES verursacht.

Contents

Chapter 1

Introduction

> [...] *there are known knowns; there are things we know we know. We also know there are known unknowns; that is to say we know there are some things we do not know. But there are also unknown unknowns – the ones we don't know we don't know.*
>
> Donald Rumsfeld

Looking into the stars has, for all we know, inspired humans since the dawn of human culture. For millenia, the motion of the celestial objects was attributed to the acting of deities. Only in the past five centuries, it was discovered that the motion of Sun, Moon, planets and stars follow mathematical rules. This discovery fundamentally changed our perception of Nature.

Our understanding of the Universe has much improved during this time. Nowadays, we are not limited to describing the motion of the observed celestial objects. Instead, modern cosmology can describe the history of the Universe. The observation of the large scale structure of the matter distribution in the Universe, high-precision measurements of the cosmic microwave background with space observatories and the discovery of an accelerated expansion of the Universe has led to the ΛCDM model, which is considered the standard model of cosmology. The name-giving ingredients are cold dark matter (CDM) and dark energy (Λ).

Roughly at the same time when Edwin Hubble found that the Universe is expanding, which laid one of the cornerstones of modern cosmology, cosmic rays were discovered by Victor Hess. His discovery opened the door for the new field of high-energy physics research. The experiments in this field use particle accelerators with ever increasing energy and luminosity to search for unknown particles. This research has led to the development of the Standard Model of Particle Physics (SM) which describes all known fundamental constituents of matter and their interactions, except for gravity.

But with increasing knowledge, the number of known unknowns grew just as well. The SM predicted a number of particles that were subsequently discovered. The most recent example is the discovery of a Higgs particle at the LHC. The SM is therefore considered a highly successful theory. However, the SM exhibits some shortcomings as well. It lacks candidates to describe dark matter or dark energy. Additionally, the SM is unable to explain the smallness of the

θ-parameter of QCD, the so-called strong CP-problem. To solve this problem, extensions to the SM predict an axion, a new very light particle that is very weakly coupled to the SM particles. More fundamentally, we know that the SM is not the ultimate theory of Nature as it does not explain gravity. String theories are possible solutions that unify gravity and the SM. These theories predict among others a number of weakly interacting and very light particles (WISPs), which can form the dark matter in the Universe.

These WISPs are searched for in laboratory experiments. In contrast to the experiments in high-energy physics, the production of these new particles is not limited because the achievable energy in the experiments is too low to produce a WISP, but it is limited simply because the probability for the process of WISP production is so small due to the weak coupling. Therefore, the experiments use high-intensity sources combined with very precise and efficient detectors. ALPS-I was such an experiment. It was successfully conducted at DESY. Based on its success, the ALPS-II experiment is currently being prepared at DESY. Other experiments search for WISPs produced in the Sun with helioscopes or for relic cold dark matter (CDM) axions with haloscopes. Another way to search for WISPs is to estimate their impact on astrophysical and cosmological observables. At present, no WISP has been detected. But existing anomalies in astrophysical observations can be explained by WISPs favouring certain regions in the WISP parameter space, which are in reach of future laboratory WISP searches. Once again, riddles in the sky motivate new laboratory experiments.

In my thesis, I will present results of my work that help to explore the WISP parameter space. These results can be split into two parts. In the first part, I will present an analysis of X-ray observations of α-Ori (Betelgeuse) that allows to exclude a region of the WISP parameters. In doing so, it will become apparent that constraints based on astrophysical observations can have hard-to-quantify model-dependent uncertainties. This makes laboratory experiments, which are less model dependent, desirable. Hence, in the second part, a silicon-based CCD detector (PIXIS CCD) is characterized in preparation of such an experiment, namely the ALPS-II experiment.

Chap. 2 gives a short overview of the SM. It follows a description of the associated strong CP-problem and its solution by introducing a new global axial symmetry that gives rise to the axion. Then, ALPs and hidden photons are introduced as examples of the WISP class. Their propagation and their production in stellar media are presented to the extent which is necessary for the following chapters. The chapter concludes with an overview of the existing constraints and hints from cosmological and astrophysical observations and laboratory based experiments.

Chap. 3 presents the calculation of a constraint on the ALP parameter based on X-ray observations of α-Ori. After a description of the relevant astronomical observations of α-Ori, of the modelling of its interior and of the X-ray observation with Chandra, the expected X-ray flux from α-Ori due to ALPs is calculated. Comparing the observed and expected flux allows to constrain the ALP parameters.

The ALPS-II experiment and its subsystems are presented in Chap. 4 including a concise review of ALPS-I. The sensitivity of ALPS-II is calculated and compared with existing constraints and hints.

The characterization of the PIXIS CCD is described in Chap. 5. First, the working principles of imaging CCD devices are explained. This is followed by the characterization of the PIXIS CCD, which includes measurements of the quantum efficiency for the wavelength used in ALPS-II, the fixed pattern noise, the associated read-out noise, the dark-count rate and the gain. At the end of this chapter, an algorithm to calculate unified confidence intervals is presented and successfully tested. The findings of my work are summarized in a conclusion in Chap. 6.

1 Introduction

Chapter 2

Weakly Interacting Slim Particles

The Standard Model of Particle Physics (SM) is one of most successful theories in Physics. It is a relativistic quantum field theory that describes three of the known four interactions of all known particles to high precision. Theoretical predictions have led to the discovery of a number of new particles. The most recent one is a Higgs particle discovered at the LHC at CERN [1, 2]. Despite of this success story, the SM is not complete: First, the observed baryon density of the Universe cannot be explained by the matter-antimatter asymmetry of the SM [3]. Furthermore, it lacks explanations for the observed dark matter (DM) [4, 5] and dark energy (DE) [6]. The observational hints for DM come from astrophysical and cosmological observations, including rotational curves of spiral galaxies, gravitational lensing, the large-scale structure of the Universe and the cosmic microwave background (CMB) [4, 5]. DE is indicated by the observed accelerating expansion of the Universe [7]. Third, the SM contains 19 parameters with values that need to be determined by experimental observations. More fundamentally, the SM lacks an explanation of the hierarchy problem and a description of gravity and the direction of time.

One of the 19 parameters of the SM is the vacuum angle of quantum chromo dynamics (QCD). All measurements of this parameter are consistent with zero an yield only upper bounds of 10^{-10} [8, 9]. This fine tuning problem is known as the "strong-CP problem". Peccei and Quinn proposed a new axial symmetry as a dynamical solution to this problem [10, 11]. The breaking of this symmetry then gives rise to a new particle, the *axion* [12, 13], which in hindsight has been the first member of a new class of hypothetical, weakly interacting slim particles (WISPs). These particles have in common very low masses and weak couplings to particles of the SM. Other members of this class are axion-like particles (ALPs) and hidden photons (HPs). These particles naturally occur when the symmetries of string theory models are broken to embed the SM.

Based on Povh et al. [14], this chapter will shortly review the Standard Model. After that, the strong CP-problem and its solution as proposed by Peccei and Quinn are described together with axions, ALPs and HPs including existing limits and experimental hints at particular regions in the WISP parameter space.

	Family			Elect. charge	Color	Weak Isospin	
	1	2	3			left-	right-handed
Leptons	ν_e	ν_μ	ν_τ	0	–	1/2	–
	e	μ	τ	-1			0
Quarks	u	c	t	2/3	r,g,b	1/2	0
	d	s	b	$-1/3$			

(a) Fermions

Particle	Charge / Interaction
γ	electric, Q
$W^\pm$, Z^0	weak charge
g	color, $8 \times (c\bar{c})$
H	Yukawa, mass generation

(b) Bosons

Table 2.1: The particle content of the standard model. 12 fermions (a) and 13 bosons (b). (After Povh et al. [14])

2.1 The Standard Model

The Standard Model of Particle Physics contains 25 elementary particles, listed in Tab. 2.1, 12 fermionic matter particles and 13 bosonic particles, which mediate the interactions between the matter particles. The underlying symmetry structure is $SU(3)_C \times SU(2)_I \times U(1)_Y$, where C is the color charge, I the weak isospin, and Y the weak hypercharge.

Six of the matter particles, the leptons, are charged only under I and Y. They are divided into three families, each consisting of a left-handed weak isospin doublet (ℓ, ν_ℓ) and a right-handed singlet ℓ_R ($\ell = e, \mu, \tau$). Thus, the weak interaction couples only to left-handed fermions, which is explained by the V−A (vector-minus-axial-vector) structure of the theory. The electro-weak interaction is mediated by four bosons, the massive $W^\pm$- and Z-boson and the massless photon, γ. The neutrinos, ν_ℓ, carry no electric charge, $Q = I_3 + Y/2 = 0$, and, hence, only interact via the weak interaction.

The six remaining matter particles, the quarks, are again grouped into three families of isospin doublets $(u, d)_L$ and singlets $(u)_R$, $(d)_R$. They additionally carry color charge, r, g or b. The associated *strong* interaction is mediated by gluons, g. The gluons also carry color charges, e.g. $(r\bar{g} + \bar{r}g)/\sqrt{2}$. Hence, the strong interaction is described by a non-Abelian gauge theory. Eight linear independent gluons exist. Because they are color-charged, gluons interact with each other and fundamental three and four gluon vertices exist.

In the framework of the SM, the electro-weak symmetry $SU(2)_I \times U(1)_Y$ is broken by the vacuum expectation value of the Higgs field. This generates the masses of the $W^\pm$ and Z bosons and the quarks and leptons acquire their (constituent) masses by interacting with the Higgs field.

The propagation, i.e. mass eigenstates of the fermions (q and ν_i) are not identical with the eigenstates taking part in the weak interactions (q' and ν_ℓ).

In the quark sector the mapping is done by the CKM[1]matrix and in the lepton sector by the PMNS[2]matrix,

$$\begin{pmatrix} \mathrm{d}' \\ \mathrm{s}' \\ \mathrm{b}' \end{pmatrix} = \underbrace{\begin{pmatrix} V_{\mathrm{ud}} & V_{\mathrm{us}} & V_{\mathrm{ub}} \\ V_{\mathrm{cd}} & V_{\mathrm{cs}} & V_{\mathrm{cb}} \\ V_{\mathrm{td}} & V_{\mathrm{ts}} & V_{\mathrm{tb}} \end{pmatrix}}_{=V_{\mathrm{CKM}}} \begin{pmatrix} \mathrm{d} \\ \mathrm{s} \\ \mathrm{b} \end{pmatrix} , \quad \begin{pmatrix} \nu_{\mathrm{e}} \\ \nu_{\mu} \\ \nu_{\tau} \end{pmatrix} = \underbrace{\begin{pmatrix} U_{\mathrm{e}1} & U_{\mathrm{e}2} & U_{\mathrm{e}3} \\ U_{\mu 1} & U_{\mu 2} & U_{\mu 3} \\ U_{\tau 1} & U_{\tau 2} & U_{\tau 3} \end{pmatrix}}_{=U_{\mathrm{PMNS}}} \begin{pmatrix} \nu_1 \\ \nu_2 \\ \nu_3 \end{pmatrix} .$$

A prominent effect of this "mixing" are neutrino oscillations. Measurements of the elements of both matrices are consistent with the matrices being unitary, which implies that no fourth quark or lepton family exist.

2.1.1 Discrete Symmetries: C,P, and T

In addition to the continuous symmetry structure, the SM is also invariant under CPT-transformation, where C, P and T are discrete symmetries. C describes charge conjugation, i.e. transforming particles into the corresponding anti-particles and vice versa by changing the sign of all internal quantum numbers. Inverting all space coordinates is described by parity conjugation, P. Its eigenvalues are ± 1. Axial vectors and scalars have $\mathrm{P} = 1$, polar vectors and pseudo-scalars $\mathrm{P} = -1$. The third discrete symmetry, T, is inverting the direction of time.

Early experiments showed that the weak interaction is not P-invariant. A famous example is the experiment of Wu et al. [15]. Physicists at that time believed that CP is conserved. However, in the 1960s, CP-violation was found in the decay of neutral kaons [16]. Neutral kaons can oscillate via box diagrams, $\mathrm{K}^0 \leftrightarrow \overline{\mathrm{K}}^0$. Both can decay into a 2π ($\mathrm{CP} = +1$) and 3π ($\mathrm{CP} = -1$) final state. This corresponds to two CP-eigenstates, $\mathrm{K}_{1,2}$, with $\mathrm{CP} = +1$ and -1, respectively, of which K^0 and $\overline{\mathrm{K}}^0$ are linear combinations. As the phase space for the 2π final state is much larger than for the 3π final state, the life time of K_1 is much smaller than that of K_2. Hence, at some large enough distance away from the production of a K^0 beam, only 3π final state are expected. But 2π final states were observed [16]. Hence, the short- and long-lived propagation eigenstates, $\mathrm{K}_{\mathrm{S,L}}$, are linear combinations of the CP eigenstates $\mathrm{K}_{1,2}$. In fact, the rate of 2π final states shows an oscillatory behaviour as a function of the proper time of the individual K^0-, $\overline{\mathrm{K}}^0$-states, which is caused by interference of the CP eigenstates $\mathrm{K}_{1,2}$ [17, 18]. In addition to this "indirect" CP-violation, direct CP-violation has been observed in decays of e.g. K^0 [19], B^0 [20] and more recently D^0 [21]. The CP-violation is caused by the complex phases in the CKM matrix.

[1]Named after Nicola Cabibbo, Makoto Kobayashi and Toshihide Maskawa.
[2]Named after Bruno Pontecorvo, Ziro Maki, Masami Nakagawa and Shoichi Sakata.

2.1.2 The Strong CP-Problem

Using natural units[3] and Einstein notation, the general form of the Lagrangian of the QCD is given by [22, 23],

$$\begin{aligned}\mathcal{L}_{\mathrm{QCD}} = &-\sum_f \bar{\psi}_f \left(i\gamma^\mu D_\mu + m_f e^{i\theta'_f} \right) \psi_f \\ &- \sum_a \left(\frac{1}{4} G^a_{\mu\nu} G^{a,\mu\nu} + \theta \frac{\alpha_\mathrm{s}}{8\pi} G^a_{\mu\nu} \widetilde{G}^{a,\mu\nu} \right) .\end{aligned} \tag{2.1}$$

The first sum is over the quark fields ψ_f, where γ^μ are the Dirac matrices, D_μ the covariant derivative, m_f the real quark masses and θ'_f the phases of the Yukawa coupling of the quark fields to the Higgs field, which generates the quark masses. The second sum runs over the eight generators of $\mathrm{SU(3)_C}$, a, where $G^a_{\mu\nu}$ is the field strength tensor of the gluon, $\widetilde{G}^a_{\mu\nu} = \varepsilon_{\mu\nu\alpha\beta} G^{a,\alpha\beta}/2$ its dual, α_s the strong coupling constant and θ a real parameter. The term proportional to θ (θ-term) arises, because the field configurations of QCD can have different winding numbers, n, that contribute to the path-integrals with weights $f(n) = \exp(i\theta n)$ [22, Sec. 23.6]. Hence, θ is an angle, i.e. $\theta \in [0, 2\pi]$.

$G^a_{\mu\nu} \widetilde{G}^{a,\mu\nu}$ is CP-odd, which can be seen from analogy with electrodynamics, where $F_{\mu\nu}\widetilde{F}^{\mu\nu} \propto \mathbf{E} \cdot \mathbf{B}$. The electric field, $\mathbf{E}$, has $\mathrm{P} = -1$, the magnetic field, $\mathbf{B}$, $\mathrm{P} = +1$, and both have $\mathrm{C} = -1$. Thus, $\mathrm{CP}(\mathbf{E} \cdot \mathbf{B}) = -\mathbf{E} \cdot \mathbf{B}$ and $F_{\mu\nu}\widetilde{F}^{\mu\nu}$ is CP-odd. The same is true for $G^a_{\mu\nu}\widetilde{G}^{a,\mu\nu}$ and, hence, a non-zero θ value results in a CP-violating Lagrangian. Complex quark masses also lead to CP-violation. A chiral transformation of the quark fields

$$\psi_f \to \exp\left(i\gamma^5 \alpha_f\right) \psi_f$$

results in [22, Sec. 23.6]

$$\theta \to \theta + 2\sum_f \alpha_f \qquad \text{and} \qquad m_f e^{i\theta'_f} \to m_f e^{i(\theta'_f + 2\alpha_f)} .$$

Hence, $\theta = 0$ can be arranged by changing θ'_f (or vice versa) and only

$$\bar{\theta} = \theta - \sum \theta'_f = \theta - \arg\det M$$

with (complex) M the quark mass matrix has physical impact. In case of at least one vanishing quark mass $m_f = 0$, the CP-violating θ-term has no effect.

The value of θ is linked to the electric dipole moment of the neutron [8],

$$d_\mathrm{n} \sim \bar{\theta} \frac{e m_*}{m_\mathrm{n}^2} \sim \bar{\theta} \cdot 6 \times 10^{-17}\, e\,\mathrm{cm} ,$$

where e is the elementary charge, $m_* = m_\mathrm{u} m_\mathrm{d}/(m_\mathrm{u} + m_\mathrm{d})$ is the reduced quark mass and m_n is the neutron mass. Recent measurements of $|d_\mathrm{n}| < 2.9 \times 10^{-26}\, e\,\mathrm{cm}$ give a limit [9]

$$|\bar{\theta}| \lesssim 10^{-10} .$$

The question why QCD conserves CP – in contrast to the weak interaction – that is why this parameter of the theory seems to be fine tuned to zero was named the "strong CP-problem".

[3] Natural units ($\hbar = c = k = 1$) are used in Chaps. 2 and 3.

2.2 Axions

This section sketches the Peccei-Quinn solution to the strong CP-problem, which predicts the existence of a new particle, the axion. The existence of the original Peccei-Quinn axion was ruled out shortly after this solution was published. Therefore, modified models were constructed to solve the strong CP-problem which predict so called "invisible" axions. These models and the coupling of these axions to SM particles are presented as well.

2.2.1 Solving the Strong CP-Problem

As seen in the previous section, a simple explanation for the CP-conserving nature of QCD is a massless quark. This is however ruled out by current lattice QCD calculations of the light quark masses, e.g. [24]. For an alternative solution, in 1977, Peccei and Quinn considered a model in which the masses of up- and down-quarks were generated by two Higgs fields. The relative phase of these two fields determine $\bar{\theta}$, rendering $\bar{\theta}(x)$ a scalar field. Its vacuum expectation is zero if the theory obeys a global chiral symmetry, now known as *Peccei-Quinn symmetry*, $\mathrm{U}(1)_{\mathrm{PQ}}$ [10, 11]. Weinberg and Wilczek realized that this gives rise to a pseudoscalar pseudo-Nambu-Goldstone boson [12, 13], the axion[4], defined as $a(x) = f_{\mathrm{a}}\bar{\theta}(x)$, where f_{a} is the axion decay constant that sets the energy scale at which $\mathrm{U}(1)_{\mathrm{PQ}}$ is broken and is linked to the electroweak scale [12]

$$f_{\mathrm{a}} \simeq v_{\mathrm{EW}} = 246\,\mathrm{GeV}\ .$$

The most simple Lagrangian describing the axion is given by [26, Sec. 14.2]

$$\mathcal{L}_{\mathrm{a}} = \frac{1}{2}\left(\partial_\mu a\right)\left(\partial^\mu a\right) - \sum_b \frac{\alpha_{\mathrm{s}}}{8\pi\, f_{\mathrm{a}}}\, a\, G^b_{\mu\nu}\widetilde{G}^{b,\mu\nu}\ . \tag{2.2}$$

the second term replaces the θ-term in Eq. (2.1). Due to this axion-gluon interaction, the axion mixes with the neutral pseudoscalar mesons, π^0, η and η'. This creates an effective potential for the axion. The axion picks up an effective mass, m_{a}, that is, assuming $m_{\mathrm{s}} \gg m_{\mathrm{u,d}}$, given by [26, Sec. 14.2]

$$m_{\mathrm{a}} = \frac{m_{\pi^0} f_\pi}{f_{\mathrm{a}}}\frac{\sqrt{m_{\mathrm{u}} m_{\mathrm{d}}}}{m_{\mathrm{u}} + m_{\mathrm{d}}} \simeq 0.6\,\mathrm{meV} \times \left(\frac{10^{10}\,\mathrm{GeV}}{f_{\mathrm{a}}}\right)\ . \tag{2.3a}$$

Hence, the axion mass and decay constant are related to the π^0 mass, m_{π^0}, and pion decay constant, f_π, by

$$m_{\mathrm{a}}\, f_{\mathrm{a}} \approx m_{\pi^0}\, f_\pi\ . \tag{2.3b}$$

In addition to the coupling to gluons, axions (effectively) couple to quarks, leptons and photons, as described in the following section.

2.2.2 Invisible Axions

The experimental constraints on the Peccei-Quinn model were already strong when it was first compared to experiments [12, 27] and by now it has been

[4] Named after a laundry detergent by F. Wilczek [25].

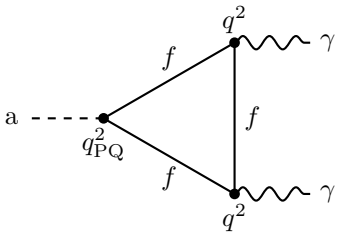

Figure 2.1: Triangle diagram contribution to the axion-photon coupling with fermion f carrying both electric (q) and $\mathrm{U}(1)_{\mathrm{PQ}}$ (q_{PQ}) charge.

ruled out, e.g. [28, 29]. Therefore, more complex models were proposed to solve the strong CP-problem and fit to experimental observations. The historical development is reviewed by Srednicki [30].

The first model adds a new sector to the SM consisting of a number of heavy quarks and a Higgs field that is not charged under the SM $\mathrm{SU}(3)_C \times \mathrm{SU}(2)_I \times \mathrm{U}(1)_Y$. The PQ symmetry involves then only this additional sector [31, 32]. The second model adds an extra singlet Higgs field to the Peccei-Quinn model [33, 34] and no extra heavy quarks. Instead the known fermions are charged under $\mathrm{U}(1)_{\mathrm{PQ}}$. This models are referred to as KSVZ and DFSZ, respectively, after the authors of the papers. In both models, the PQ symmetry is broken by the large vacuum expectation value, v, of the additional Higgs field and its phase becomes the axion. With N referring to the number of families charged under $\mathrm{U}(1)_{\mathrm{PQ}}$ and defined below, the axion decay constant is defined by

$$f_{\mathrm{a}} = \frac{f_{\mathrm{PQ}}}{N} \sim \frac{v}{N} \,,$$

where f_{PQ} is the PQ-breaking scale. As can be seen from Eq. (2.2) the axion-gluon coupling is $\propto 1/f_{\mathrm{a}}$. This is also true for other (effective) couplings of the axion [35], i.e.

$$g_{\mathrm{a}X} \propto \frac{1}{f_{\mathrm{a}}} \,,$$

where X is any particle. Since in these models v can be arbitrary large and $f_{\mathrm{a}} \sim v/N$, the couplings $g_{\mathrm{a}X}$ can be arbitrarily small. Hence, these axions are *invisible* and very light (cf. Eqs. (2.3)). Thus, they are perfect candidates for WISPs.

Coupling to Photons

By virtue of their mixing with pions, axions couple with photons with a generic Lagrangian

$$\mathcal{L}_{\mathrm{a}\gamma} = -\frac{1}{4}\, g_{\mathrm{a}\gamma}\, a\, F_{\mu\nu} \widetilde{F}^{\mu\nu} = g_{\mathrm{a}\gamma}\, a\, \mathbf{E} \cdot \mathbf{B} \,, \tag{2.4}$$

where F is the electromagnetic field strength tensor, $\widetilde{F}$ its dual and $g_{\mathrm{a}\gamma}$ the axion-photon coupling constant. The processes that contribute to this mixing and, thus, also $g_{\mathrm{a}\gamma}$ are model-dependent. If fermions carry both electric and $\mathrm{U}(1)_{\mathrm{PQ}}$ charge, triangle loop diagrams contribute (cf. Fig. 2.1). A general form

of the coupling is given by [35]

$$\begin{aligned} g_{\mathrm{a}\gamma} &= \frac{\alpha_{\mathrm{em}}}{2\pi\, f_{\mathrm{a}}} \left(\frac{E}{N} - \frac{2}{3}\frac{4+z+w}{1+z+w} \right) \\ &\simeq \frac{\alpha_{\mathrm{em}}}{2\pi\, f_{\mathrm{a}}} \left(\frac{E}{N} - 1.92 \right) , \end{aligned} \tag{2.5}$$

where $\alpha_{\mathrm{em}} = e^2/4\pi \approx 1/137$ is the fine-structure constant and z, w light quark mass ratios given by [36]

$$z = \frac{m_{\mathrm{u}}}{m_{\mathrm{d}}} = 0.553 \pm 0.043 \qquad\qquad w = \frac{m_{\mathrm{u}}}{m_{\mathrm{s}}} = (29.1 \pm 3.1) \times 10^{-3} .$$

E and N are model dependent anomaly coefficients,

$$N = \sum_i X_i\, T(R_i) , \qquad\qquad E = \sum_i X_i Q_i^2 D(R_i) ,$$

with X_i the $\mathrm{U}(1)_{\mathrm{PQ}}$ charge of particle species i, R_i its $\mathrm{SU}(3)_{\mathrm{C}}$ representation with index[5] T and dimension D. E.g. in the KSVZ model with one additional heavy quark one has $i = q, \overline{q}$, $Q_i = \pm m/3$ and $T(3) = 1/2$, $D(3) = 3$, which results in

$$\left(\frac{E}{N}\right)_{\mathrm{KSVZ}} = \frac{2\, X\, \dfrac{m^2}{9}\, 3}{2\, X\, \dfrac{1}{2}} = \frac{2}{3}\, m^2 \qquad (m = 0, 1, 2, 3) .$$

For leptons, i.e. color singlets, one has $T = 0$, $D = 1$ and $Q = 0, 1$. Hence, in the DFSZ model one finds

$$\left(\frac{E}{N}\right)_{\mathrm{DFSZ}} = \frac{\displaystyle\sum_{q=\mathrm{d,s,b}} 3\,\frac{1}{9} + \sum_{q=\mathrm{u,c,t}} 3\,\frac{4}{9} + \sum_{\ell=\mathrm{e},\mu,\tau} 1}{\displaystyle\sum_{q=\mathrm{d,s,b}} \frac{1}{2} + \sum_{q=\mathrm{u,c,t}} \frac{1}{2} + \sum_{\ell=\mathrm{e},\mu,\tau} 0} = \frac{8}{3} .$$

Other models can be constructed that have $E/N = 2$ [37], i.e. almost cancelling the second term in the parentheses of Eq. (2.5).

The coupling of axions to photons is important for experimental tests of these models, because high-intensity photon fields are easily prepared in experiments. The parameter space spanned by these axion models in the mass-coupling plane is shown below in Fig. 2.3.

Coupling to Fermions

The generic axion-fermion coupling is given by a pseudoscalar or derivative axial-vector interaction [26, Sec. 14.3]

$$\mathcal{L}_{\mathrm{a}f} = -i\, \frac{C_f m_f}{f_{\mathrm{a}}}\, \bar{\Psi}_f \gamma_5 \Psi_f\, a \qquad \text{or} \qquad \frac{C_f}{2 f_{\mathrm{a}}}\, \bar{\Psi}_f \gamma^\mu \gamma_5 \Psi_f\, \partial_\mu a ,$$

[5] The index T of a representation R is defined as $\mathrm{Tr}(t_R^a\, t_R^b) = T(R)\delta^{ab}$, where t_R^a are the matrices of the representations.

Model	C_u	C_d	C_s	C_p	C_n
DFSZ	$\sin^2\beta/N$	$\cos^2\beta/N$		$-0.10-0.45\cos^2\beta$	$-0.18+0.39\cos^2\beta$
KSVZ	0	0	0	-0.39	-0.04

Table 2.2: Effective $\mathrm{U}(1)_\mathrm{PQ}$ charges of the nucleons in invisible axion models [26, Sec. 14.3].

where C_f is the effective $\mathrm{U}(1)_\mathrm{PQ}$ charge of fermion f. For instance, in the KSVZ model, leptons carry no $\mathrm{U}(1)_\mathrm{PQ}$ charge, hence, $C_\mathrm{e}^\mathrm{KSVZ}=0$ up to radiative corrections [35]. On the other hand, leptons are $\mathrm{U}(1)_\mathrm{PQ}$ charged in the DFSZ model and with $x=v_1/v_2$ being the ratio of the vacuum expectation values of the two PQ-Higgs doublets and

$$\cos^2\beta=\frac{x^2}{1+x^2} \tag{2.6}$$

one gets [26, Sec. 14.3]

$$C_\mathrm{e}^\mathrm{DFSZ}=\frac{\cos^2\beta}{N}\ .$$

The coupling to nucleons are given by [26, Sec. 14.3]

$$\begin{aligned}C_\mathrm{p}=&(C_\mathrm{u}-\eta)\Delta u+(C_\mathrm{d}-\eta z)\Delta d+(C_\mathrm{s}-\eta w)\Delta s\ ,\\ C_\mathrm{n}=&(C_\mathrm{u}-\eta)\Delta d+(C_\mathrm{d}-\eta z)\Delta u+(C_\mathrm{s}-\eta w)\Delta s\ ,\end{aligned}$$

where w, z are the quark mass ratios used above, $\eta=1/(1+z+w)$, Δq the proton-spin portion carried by quark flavour q, and C_q the $\mathrm{U}(1)_\mathrm{PQ}$ charges of the different quark flavours as given in Tab. 2.2.

2.3 Axion-like Particles and Hidden Photons

Axion-like Particles

In the previous section models were presented that solve the strong CP-problem by adding new Higgs fields to the SM that are charged under a chiral U(1). The axion is then the pseudo Nambu-Goldstone boson of this broken symmetry. Axions can also appear in compactifications of string theories [38–40]. More over these compactifications can create a whole "axiverse", i.e. a number of axion-like particles (ALPs) [41–43]. They have similar properties as the axion and, hence, corresponding Lagrangians of the form [44]

$$\begin{aligned}\mathcal{L}=&\frac{1}{2}\partial_\mu a_i\partial^\mu a_i-\frac{\alpha_\mathrm{s}}{8\pi\,f_{\mathrm{a}i}}C_{i\mathrm{g}}\,a_i G^b_{\mu\nu}\widetilde{G}^{b,\mu\nu}-\frac{\alpha_\mathrm{em}}{8\pi\,f_{\mathrm{a}i}}C_{i\gamma}\,a_i F_{\mu\nu}\widetilde{F}^{\mu\nu}\\ &+\sum_f\bar{\Psi}_f\left(\gamma^\mu\frac{1}{2}(C_{\mathrm{R}fi}+C_{\mathrm{L}fi})\gamma_5+\gamma^\mu\frac{1}{2}(C_{\mathrm{R}fi}-C_{\mathrm{L}fi})\right)\Psi_f\,\frac{\partial_\mu a_i}{f_{\mathrm{a}i}}\ ,\end{aligned}$$

where $f_{\mathrm{a}i}$ is the decay constant of the ith ALP, a_i, and the C's are dimensionless coupling constants of this field to the various SM fields, namely to gluons ($C_{i\mathrm{g}}$), photons ($C_{i\gamma}$), right- ($C_{\mathrm{R}fi}$) and left-handed $C_{\mathrm{L}fi}$ fermion f. These couplings are assumed to be of order unity. Only derivative couplings to the fermion fields,

Ψ_f, are allowed because the axial symmetry $\mathrm{a} \to \mathrm{a} + \mathrm{const}$ can only be violated by the anomalous couplings to gluons and photons.

From the above Lagrangian one can see, that ALPs interact with SM particles similar to axions. Depending on the model, expected values for f_a can vary from 10^4 to $10^{17}\,\mathrm{GeV}$ [45]. Their mass and decay constant are not related as it is the case for axions (cf. Eq. (2.3b)). Hence, an ALP is a perfect candidate for a WISP.

Hidden Photons

Besides these additional chiral U(1) symmetries, compactifications can also yield gauge $\mathrm{U}(1)_\mathrm{h}$ symmetries [46]. Because the SM particles are not charged under $\mathrm{U}(1)_\mathrm{h}$, the corresponding bosons are hidden. Hence, they are referred to as *hidden photons*[6]. If some of these U(1) remain unbroken to low energy scales they couple to SM photons via a kinetic mixing [44, 47] with a Lagrangian

$$\mathcal{L} = -\frac{1}{4}F_{\mu\nu}F^{\mu\nu} - \frac{1}{4}X_{\mu\nu}X^{\mu\nu} + \frac{\chi}{2}F_{\mu\nu}X^{\mu\nu} + \frac{m_{\gamma'}^2}{2}X_\mu X^\mu \,, \tag{2.7}$$

where X_μ is the hidden photon field, $m_{\gamma'}$ its mass and $X_{\mu\nu} = \partial_\mu X_\nu - \partial_\nu X_\mu$ its field strength. This gives rise to photon-hidden photon oscillations, which are presented in the next section.

2.4 Axion, Axion-like Particle and Hidden Photon Propagation and Production

The interactions of axions, ALPs and HPs as presented in Secs. 2.2 and 2.3 allow for a number of experimental searches for these particles. In the context of this work, the coupling to photons is of importance. For axions and ALPs, their coupling to photons leads to an oscillation between photons and axions (or ALPs) when they propagate through regions with external electromagnetic fields. Secs. 2.4.1 and 2.4.3 describe the propagation of a photon-axion (or photon-ALP) state in the presence of an external magnetic field and the conversion of thermal photons to axions (or ALPs) in the plasma in stellar cores, respectively. The oscillation between photons and HPs is described in Sec. 2.4.2.

2.4.1 Axion and ALP Oscillations in External Magnetic Fields

In a region with external magnetic fields Eq. (2.4) leads to $\gamma \leftrightarrow \mathrm{a}$ oscillations. The low-energy effective Lagrangian is given by [48]

$$\mathcal{L} = -\frac{1}{4}F_{\mu\nu}F^{\mu\nu} + \frac{1}{2}\left(\partial_\mu a \partial^\nu a - m_\mathrm{a}^2 a^2\right) - \frac{1}{4}g_{\mathrm{a}\gamma}aF_{\mu\nu}\widetilde{F}^{\mu\nu} \,.$$

Ignoring effects causing rotation of the polarization (e.g. Faraday effect) the equations of motion for axions and photons propagating in the z-direction are given by [49]

$$\left[(\omega^2 + \partial_z^2) - \begin{pmatrix} -2\omega^2(n-1) & -g_{\mathrm{a}\gamma}B_\perp\omega \\ -g_{\mathrm{a}\gamma}B_\perp\omega & m_\mathrm{a}^2 \end{pmatrix}\right]\begin{pmatrix} A \\ a \end{pmatrix} = 0 \,,$$

[6] Sometimes also referred to as para-, dark, or sterile photons.

where ω is the photon energy, $B_\perp$ the magnetic field perpendicular to the z-axis, A the electromagnetic vector potential parallel to $B_\perp$, and n the corresponding refractive index of the medium. Focussing on situations where the lateral extent of the magnetic field is much larger than the photon field (as is the case in LSW experiments), the axion field is given by [48]

$$a(z,t) = \frac{ig_{\mathrm{a}\gamma}}{2k_{\mathrm{a}}} BE_0 e^{-i(\omega t - k_{\mathrm{a}} z)} \int \mathrm{d}z' f(z') e^{iqz'} \ ,$$

where

$$B_\perp(z) = Bf(z) \ , \qquad E(z,t) = E_0 \exp[i\omega(nz-t)] \ ,$$
$$k_{\mathrm{a}}^2 = \omega^2 - m_{\mathrm{a}}^2 \ ,$$

and

$$q = n\,\omega - \sqrt{\omega^2 - m_{\mathrm{a}}^2} \approx \omega(n-1) + \frac{m_{\mathrm{a}}^2}{2\omega} \tag{2.8}$$

being the momentum transfer to the magnetic field, where the last approximation is valid for low-mass ALPs, $m_{\mathrm{a}} \ll \omega$.

The probability to find an axion in a photon beam (or vice versa) that travelled a distance L through a magnetic field is then given by [48]

$$P(\mathrm{a} \leftrightarrow \gamma) = \frac{1}{4} \frac{\omega}{k_{\mathrm{a}}} \left(g_{\mathrm{a}\gamma} BL\right)^2 |F|^2 \ . \tag{2.9}$$

The form factor is defined as

$$F = \frac{1}{L} \int_0^L \mathrm{d}z f(z) e^{iqz} \tag{2.10a}$$

and can be simplified in the case of a homogeneous magnetic field ($f = 1$) of length L:

$$|F| = \frac{2}{qL} \sin\left(\frac{qL}{2}\right) \ . \tag{2.10b}$$

This form factor is bounded by unity, $|F| \leq 1$. Hence, the conversion probability is bounded by

$$P(\mathrm{a} \leftrightarrow \gamma) \leq \frac{1}{4} \left(g_{\mathrm{a}\gamma} BL\right)^2 \ . \tag{2.11}$$

This bound is saturated if $qL/2 \ll 1$ and $m_{\mathrm{a}} \ll \omega$. This case is called *strong mixing*.

If the magnetic field consists of many distinct domains of size ℓ with a randomly orientated magnetic field of total strength B the conversion probability for an ALP after travelling a distance $L = N\ell$, i.e. through N domains, is given by [50]

$$P_{\mathrm{dom}}(\mathrm{a} \leftrightarrow \gamma) = \frac{1}{3} \left[1 - \exp\left(-\frac{3}{8} N (gB\ell)^2\right)\right] \tag{2.12a}$$

$$\leq \frac{(g_{\mathrm{a}\gamma} BL)^2}{8N} \ . \tag{2.12b}$$

Comparing this upper bound (Eq. (2.12b)) with the upper bound in the case of a homogeneous magnetic field (Eq. (2.11)) shows that the conversion probability after the passage through a volume with randomly oriented magnetic fields is by a factor $2N$ smaller compared to the case with a homogeneous magnetic field.

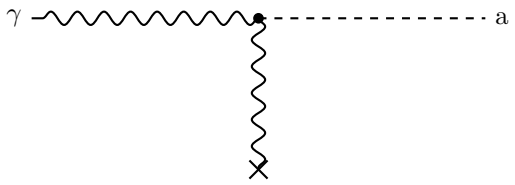

Figure 2.2: Sketch of the Primakoff process converting photons (γ) to axions or ALPs (a) in the presence of an external field.

2.4.2 Photon-HP Oscillations

The kinetic mixing of photons with HPs given by Eq. (2.7) gives the following equations of motion [48],

$$\left[\omega^2 + \partial_z^2 - \begin{pmatrix} -2\omega^2(n-1) + m_{\gamma'}^2\chi^2 & -m_{\gamma'}^2\chi \\ -m_{\gamma'}^2\chi & m_{\gamma'}^2 \end{pmatrix}\right] \begin{pmatrix} A \\ X \end{pmatrix} = 0$$

for particles propagating along the z-axis. In analogy to the axion case, the resulting oscillation probability is given by

$$P(\gamma \leftrightarrow \gamma') = \chi^2 \frac{m_{\gamma'}^4}{(\omega q)^2} \sin^2\left(\frac{ql}{2}\right) , \tag{2.13}$$

where l is the total distance travelled and

$$q = n\,\omega - \sqrt{\omega^2 - m_{\gamma'}^2} \approx \omega(n-1) + \frac{m_{\gamma'}^2}{2\omega} . \tag{2.14}$$

Conservation of momentum requires

$$m_{\gamma'} \leq \omega . \tag{2.15}$$

2.4.3 Axion and ALP Production in Stellar Media

In stellar plasma the largest contribution to axion- and ALP-production is due to the Primakoff process of photons interacting in the electric fields of nuclei as shown in Fig. 2.2. Typically, the photon energy, ω, in these plasmas is large compared to the plasma frequency,

$$\omega_{\rm pl}^2 = 4\pi\,\alpha_{\rm em}\,\frac{n_{\rm e}}{m_{\rm e}} , \tag{2.16}$$

or the axion mass, $m_{\rm a}$. Where in the above $n_{\rm e}$ and $m_{\rm e}$ are the free electron density and electron mass, respectively. The transition rate for these photons is given by [26, Sec. 5.2]

$$\Gamma_{\gamma\to{\rm a}} = \frac{g_{{\rm a}\gamma}^2 T\kappa^2}{32\pi}\left[\left(1+\frac{\kappa^2}{4\omega^2}\right)\ln\left(1+\frac{4\omega^2}{\kappa^2}\right) - 1\right] ,$$

where the screening scale is given for a non-degenerate medium by

$$\kappa^2 = \frac{4\pi\alpha_{\rm em}}{T}\left(n_{\rm e} + \sum_i Z_i^2 n_i\right) \tag{2.17}$$

with $\alpha_{\rm em}$ the fine-structure constant, T the temperature, $n_{\rm e}$ and n_j the number densities of electrons and nuclear species j, and Z_j the respective proton numbers. Multiplying with the differential photon density, which is given by the Bose-Einstein distribution, $n_{\rm BE}$, yields the differential axion production rate,

$$\begin{aligned}\frac{\mathrm{d}N_{\rm a}}{\mathrm{d}V\,\mathrm{d}\omega\,\mathrm{d}t} &= n_{\rm BE}\,\Gamma_{\gamma\to{\rm a}} \\ &= \frac{g_{{\rm a}\gamma}^2 T\kappa^2}{32\pi^3}\frac{\omega^2}{e^{\omega/T}-1}\left[\left(1+\frac{\kappa^2}{4\omega^2}\right)\ln\left(1+\frac{4\omega^2}{\kappa^2}\right)-1\right]\,.\end{aligned} \tag{2.18}$$

Assuming that the coupling of axions is weak such that produced axions leave the stellar medium undisturbed, the spectrum of produced axions (or ALPs) is given by integration over the stellar interior

$$\frac{\mathrm{d}N_{\rm a}}{\mathrm{d}\omega\,\mathrm{d}t} = 4\pi\int_0^R r^2\mathrm{d}r\,\frac{\mathrm{d}N_{\rm a}}{\mathrm{d}V\,\mathrm{d}\omega\,\mathrm{d}t}\,, \tag{2.19}$$

where a spherical-symmetric stellar profile was assumed.

2.5 WISP Observations

The existence of a WISP could have measurable impact on cosmological and astrophysical observables or the outcome of laboratory-based experiments. Existing observations exclude regions of the axion, ALP and HP parameter space spanned by the WISP mass and coupling to SM particles. Because axions and ALPs behave similarly, most observables are sensitive to both axion and ALP parameters. Hence, in the following discussion axion will be used synonymously for axions and ALPs and "QCD-axion" to note when a constraint does not include ALPs. Accordingly, "a" will denote an axion or an ALP. For axions, it is common praxis to use the $m_{\rm a}$-$g_{{\rm a}\gamma}$ plane to illustrate the constraints. For observations that depend on other couplings, e.g. $g_{{\rm a}N}$, the limits are converted to $g_{{\rm a}\gamma}$, which is a model-dependent procedure. This section will review the recent observations constraining the parameters space and observations that can be explained by the existence of a WISP. A selection of the resulting bounds is shown in Figs. 2.3 and 2.4.

Fig. 2.3 also shows the parameter space spanned by hadronic QCD-axion models for $E/N = 2$ and $E/N = 6$ as yellow band. The original KSVZ model ($E/N = 0$) and the DFSZ model ($E/N = 8/3$) are indicated by dashed and solid black lines, respectively.

2.5.1 Cosmological Observations

During the last decades, cosmological observations led to a much improved understanding of the evolution of the Universe. In a nutshell, the Universe started in the Big Bang, a state of an extremely hot and dense plasma. Expanding space lead to a cooling of this plasma. At some point during the evolution, the temperature was low enough to have stable baryonic matter and later electrons and photons decoupled and hydrogen atoms became stable. Initial quantum fluctuations caused non-uniformities, which seeded the cosmological structures we observe today. To reconcile the observations with the strength of the initial non-uniformities, i.e. to explain why the Universe appears uniform on large

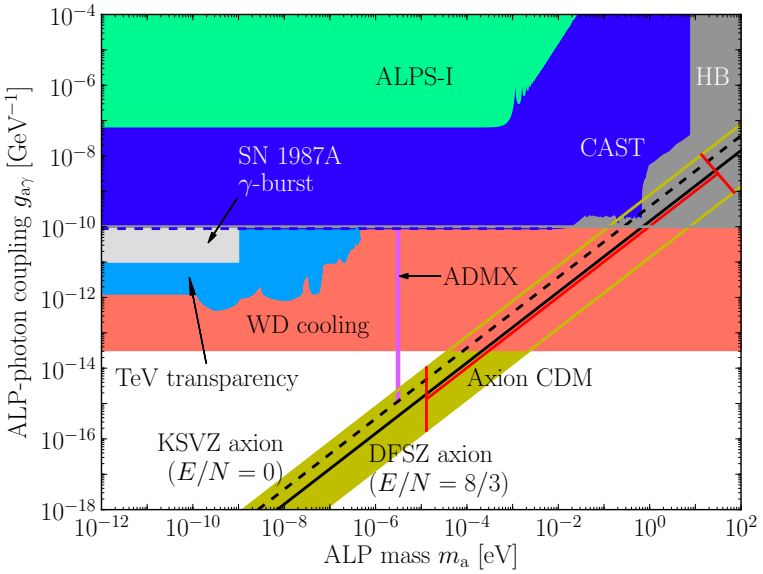

Figure 2.3: ALP parameter space. Shown are the constraints from ALPS-I (light green, [51]), the SN 1987A gamma-ray burst (light gray, [52, 53]), X-ray observation of α-Ori (dark red, Chap. 3), CAST (blue, [54–56]), the ADMX haloscope (purple, [57]), and the lifetime of HB stars (dark gray, [26, 29]). The ALP parameters indicated by anomalous white dwarf cooling [44, 58] is highlighted by the light-red area and the parameters favored by the TeV-transparency [59] is shown as light blue region. The parameter space of the QCD-axion models is shown as yellow band together with the DFSZ (solid black) and the original KSVZ model (dashed black). The parameter space for axion CDM is indicated by a red line. For details of the different observations refer to Sec. 2.5.

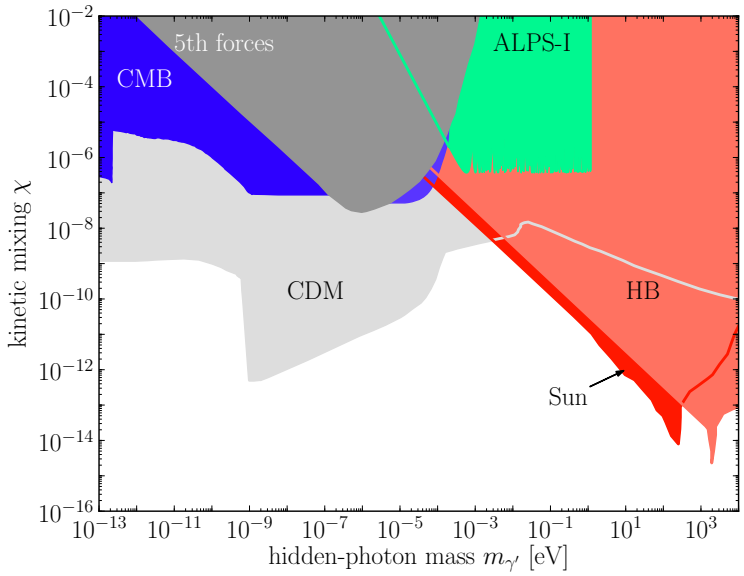

Figure 2.4: HP parameter space. Shown are the constraints from ALPS-I (light green, [51]), 5th forces experiments (dark gray, [60]), CMB-distortion (blue, [61, 62]), HP-CDM (light gray, [63], and solar and HB-star lifetime arguments (red and light red, [64–66]). For details of the different observations refer to Sec. 2.5.

scales, it is assumed that the Big Bang was followed by a phase of inflation. During inflation the expansion of space was exponentially fast, levelling the initial non-uniformities. At the end of inflation the Universe is reheated by the decay of the field that drives inflation. A great success of this research is the development of the ΛCDM model that describes the evolution after the inflationary phase. Together with models describing the formation of baryonic matter (Big Bang nucleosynthesis, BBN) and large-scale structures (LSS) this can explain many cosmological observables. A key conclusion of this model building is that additional dark matter (DM) is necessary to keep both the ΛCDM and BBN models in agreement with the observations. As mentioned above DM is also favoured by many other observations (for a review see e.g. Bertone et al. [5]). The existence of DE to explain the expansion of the Universe is another important consequence of the ΛCDM model [7]. Recent results of the Planck satellite confirmed the ΛCDM model [67].

Axions and HPs can act as (cold) dark matter [63]. However, the probably most widely studied class of candidates for DM are weakly interacting massive particles (WIMPs). In supersymmetric extensions of the SM, a WIMP candidate exists in the form of the lightest supersymmetric particle [4, 5]. It is expected that the next generation of direct WIMP searches, e.g. XENON1T [68], combined with results from the LHC will either find conclusive evidence for the existence of WIMPs or challenge the WIMP paradigm [69].

Axions as DM

To be a valid DM candidate the lifetime of the axion has to exceed the age of the Universe ($\sim 13.8\,\mathrm{Gyr}$ [67]). The axion can decay via the process $\mathrm{a} \to 2\gamma$ with a lifetime of [63]

$$\tau_\mathrm{a} = \frac{64\pi}{g_{\mathrm{a}\gamma}^2 m_\mathrm{a}^3} \approx 1.3 \times 10^{25}\,\mathrm{s} \left(\frac{g_{\mathrm{a}\gamma}}{10^{-10}\,\mathrm{GeV}^{-1}}\right)^{-2} \left(\frac{m_\mathrm{a}}{\mathrm{eV}}\right)^{-3} .$$

This excludes axions with large masses or couplings from being DM,

$$g_{\mathrm{a}\gamma} \lesssim 5467 \times 10^{-10}\,\mathrm{GeV}^{-1} \cdot \left(\frac{m_\mathrm{a}}{\mathrm{eV}}\right)^{-3/2} .$$

Depending on the temperature of reheating after inflation and the energy scale at which $\mathrm{U}(1)_\mathrm{PQ}$ is broken, axions can be produced in the early Universe by three different processes as reviewed by Sikivie [70]. First, thermally during phases of the evolution of the Universe were the interaction rate of axions with SM particles is not negligible. Second, by the so-called "misalignment mechanism". The axion field has random initial conditions. Figuratively speaking, during the early evolution, the size of the causal horizon is smaller than the Compton wavelength of the axion. At the point where the horizon encloses the Compton wavelength, the axion field starts to oscillate around the minimum of the potential. This results in a non-relativistic population. If the breaking of $\mathrm{U}(1)_\mathrm{PQ}$ happens at an energy scale above the reheating temperature, the causal horizon contains one initial field configuration given by the misalignment angle θ. For an ALP the cosmic CDM mass fraction is given by [44, 70]

$$\Omega_\mathrm{a} h^2 \approx 0.16 \times \left(\frac{m_\mathrm{a}}{\mathrm{eV}}\right)^{1/2} \left(\frac{f_\mathrm{a}}{10^{11}\,\mathrm{GeV}}\right)^2 \left(\frac{\theta}{\pi}\right)^2$$

and for a QCD axion by

$$\Omega_\mathrm{a} h^2 \approx 0.71 \times \left(\frac{f_\mathrm{a}}{10^{12}\,\mathrm{GeV}}\right)^{7/6} \left(\frac{\theta}{\pi}\right)^2 .$$

Third, the decay of topological defects (axion strings and domain walls) can contribute to $\Omega_\mathrm{a} h^2$ if the reheating temperature is above the symmetry-breaking energy scale, i.e. $\mathrm{U}(1)_\mathrm{PQ}$ is broken after inflation and different random initial values contribute. The corresponding CDM mass fraction is given by

$$\Omega_\mathrm{a} h^2 \approx 0.3 \times \left(\frac{f_\mathrm{a}}{10^{12}\,\mathrm{GeV}}\right)^{7/6}$$

for QCD axions [44, 70]. Hence, using the observed CDM mass fraction found by the Planck satellite ($\Omega_\mathrm{c} h^2 \approx 0.12$) [67], a QCD-axion mass $m_\mathrm{a} \gtrsim 1.3 \times 10^{-5}\,\mathrm{eV}$ is necessary in order not to overclose the Universe by axion CDM.

HPs as DM

Similar to axions, the HP field can have a non-vanishing zero-momentum component due to the misalignment mechanism. This component can constitute

the CDM. The interaction between photons and HPs is largest when the HP mass equals the plasma mass of the photon, $m_{\gamma'} = m_\gamma$, at some time during the evolution of the Universe with temperature $T_{\rm res}$. Depending on $T_{\rm res}$ different cosmological observations can be used to constrain the HP parameter space [63]. Estimates of the DM density during recombination and today show rough agreement. Thus, the resonance should have happened before recombination yielding $\chi \gtrsim 10^{-9}$. For masses $m_{\gamma'} \gtrsim$ neV a more stringent bound can be made. In this regime, the photons coming from $\gamma' \to \gamma$ distort the spectrum of the CMB from its original blackbody shape. Furthermore, the additional photons from $\gamma' \to \gamma$ dilute the neutrino density with respect to the photons, which can be constrained by estimates of the effective number of relativistic neutrino species.

Haloscopes

Axion haloscopes search for CDM axions. The density of the DM halo of the Milky Way is estimated to be [71]

$$\rho_{\rm DM}^{\rm local} \approx 0.39\,{\rm GeV\,cm^{-3}}\ .$$

If the DM halo density at the location of the Sun consists of axions, they resonantly convert into photons in a microwave cavity if the resonance frequency of the cavity equals the axion energy and the cavity is located inside a strong static magnetic field [72]. The corresponding increase in power inside the cavity can be detected by a microwave receiver. A number of such haloscope experiments are performed [57, 73–76].

In a recent proposal a spherical mirror is combined with a sensitive photo detector [77]. As HPs and in a magnetic field axions mix with photons, their wave function is an admixture of an electromagnetic and a sterile component. When this wave function interacts with the surface of the mirror, the electromagnetic component is reflected and focussed in the center of the mirror sphere, where it can be detected by a broadband detector. Hence, in contrast to the microwave cavity haloscopes, these experiments are sensitive to a broad broad mass region that depends on the spectral acceptance of the detector.

Bounds from CMB observables

The conversion of photons to WISPs is energy dependent. Hence, the initially almost perfect black body spectrum of the CMB would be distorted by processes like

$$\gamma + X \to {\rm a} + Y\ , \qquad\qquad \gamma + X \to \gamma' + Y\ ,$$

where X and Y may represent arbitrary particles. Based on the spectral measurements of the FIRAS instrument aboard the COBE space craft, the HP parameters can be constrained in a wide mass range [61, 62]. For axions the limits depend on the primordial magnetic field, $B_{\rm prim}$, and limits are given only for $g_{{\rm a}\gamma} B_{\rm prim}$ [78].

Because of their low masses, thermally produced WISPs can contribute to the radiation energy density in a way similar to neutrinos and, thus, impact the CMB [79]. This can be used to constrain the mass in hadronic axion models [80–82].

2.5.2 Astrophysical Observations

Stellar Evolution

If WISPs exist, they can be produced in stellar cores and can instantly escape because of their weak interaction. This increases the total energy loss and the evolution of stars can change dramatically. For a non-degenerate star like the Sun, the additional energy loss results in a contraction and heating. Consequently, the rate at which the nuclear reactions take place increases. Hence, the overall lifetime is decreased [26]. Based on the observed neutrino flux, this allows to constrain the WISP parameter space [83].

Horizontal branch (HB) stars are burning helium in their core and hydrogen in a shell around the core. Stars reach this phase after burning hydrogen to helium in a shell around a degenerate helium core during their red-giant phase (RGB). Stellar evolution models predict the length of the red-giant and horizontal-branch phases and hence the ratio of HB over RGB stars. The prediction fits the observation on the 10 % level, yielding

$$g_{a\gamma} \lesssim 1 \times 10^{-10}\,\mathrm{GeV}^{-1}\ ,$$

for $m_a \lesssim 30\,\mathrm{keV}$ [26, 29]. In a more recent analysis, the duration of the blue-loop phase of the evolution of massive stars, which is necessary to e.g. account for the existence of Cepheid stars, is calculated assuming different values of $g_{a\gamma}$ and a conservative bound of

$$g_{a\gamma} \lesssim 0.8 \times 10^{-10}\,\mathrm{GeV}^{-1}$$

is put from the observation that above this value the blue-loop phase vanishes from the evolution [84].

Sun

In addition to constraining WISP parameters with the above energy-loss argument, WISPs produced in the Sun can be detected by experiments on Earth similar to solar neutrino observatories. In these helioscopes, a telescope observes the Sun through a strong magnetic field that is perpendicular to the line of sight. Axions produced in the Sun's core can reconvert to photons in the magnetic field and be detected. X-ray detectors are used because this is the average photon energy in the solar core. This concept was first implemented by Lazarus et al. [85] followed by the Tokyo Axion Helioscope (SUMICO) [86–88] and the CERN Axion Solar Telescope (CAST) [89]. This technology can be used to constrain both the axion [54–56] and HP [90] parameter space. Dedicated HP helioscopes are operated at the Hamburger Sternwarte [91] and SUMICO [92].

Additionally, solar models can be used limit the solar luminosity in HPs, which allows to constrain the HP parameter space [64, 65].

Recently, the interaction of DM and solar axions in liquid-xenon dark matter detectors was discussed and the expected sensitivity on the axion-electron coupling calculated [93].

SN 1987A

An analogy to the stellar energy-loss argument can be made for the duration of the neutrino emission of a supernovae. During the stellar collapse of a super-

nova, the density of the inner core is so high that neutrinos are trapped, most effectively by heavy nuclei. As more material falls in, the inner core stiffens and a shock wave starts to propagate outward. The inner core forms a proto-neutron star. In the shock wave, heavy nuclei are dissociated and neutrinos can escape from the outer shell of the proto-neutron star (prompt ν_e burst). It then cools by the emission of (anti)neutrinos resulting in a deleptonization. Meanwhile, after a period of standstill, the shock wave continues to propagate outwards and eventually ejects the remaining material into outer space [26, Sec. 11.1].

Axions would provide an additional cooling channel to the proto-neutron star and, thus, shorten the duration of the cooling period. In the inner core axions are produced by nucleon bremsstrahlung [26, Sec.13.3],

$$N + N \to N + N + a \,.$$

Neutrinos from SN 1987A were detected by several detectors with a pulse duration of $\tau \approx 12\,\mathrm{s}$. Requiring that the duration of the cooling period is not shortened by more than a factor of two sets an upper limit on the energy released by axions from the inner core to [26, Sec. 13.4]

$$\varepsilon_a \lesssim 1 \times 10^{19}\,\mathrm{erg\,g^{-1}\,s^{-1}} \,.$$

Depending on the model for the evolution of the supernova and the axion-nucleon interaction, this can be used to constrain the QCD-axion mass and decay constant [94]

$$m_a \lesssim 16\,\mathrm{meV} \,, \qquad\qquad f_a \gtrsim 4 \times 10^8\,\mathrm{GeV} \,,$$

which are considered rough estimates due to the insufficient knowledge of the axion emission rate.

In addition to providing an additional cooling channel, the axions emitted by the proto-neutron star reconvert to photons in the galactic magnetic field and a gamma-ray burst coincident with the neutrino signal is registered at Earth. The non-observation of such a signal with the Gamma-Ray Spectrometer aboard the Solar Maximum Mission satellite allows to set a limit on the ALP-photon coupling of [52, 53]

$$g_{a\gamma} \lesssim 10^{-11}\,\mathrm{GeV}^{-1} \qquad \text{for} \qquad m_a \lesssim 10^{-9}\,\mathrm{eV} \,.$$

White Dwarf Cooling

Comparing the observed luminosity function of white dwarfs, i.e. the number of white dwarfs per luminosity interval, with models of the cooling process shows a discrepancy at $-3 \lesssim \log_{10}(L/L_\odot) \lesssim -1$, which can be lifted by assuming an additional QCD-axion-mediated cooling channel, indicating [58]

$$m_a \cos\beta \gtrsim 5\,\mathrm{meV}$$

in the DFSZ model where $\cos\beta$ is given by Eq. (2.6). This can be converted to set a lower limit of $g_{a\gamma} \gtrsim 3 \times 10^{-13}\,\mathrm{GeV}^{-1}$ on the axion-photon coupling for $m_a \lesssim 1\,\mathrm{keV}$ [44].

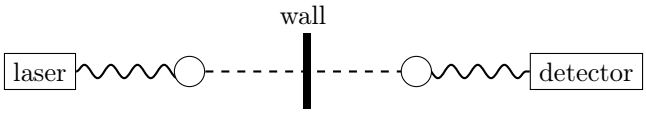

Figure 2.5: Illustration of the light shining through a wall (LSW) principle. Photons emitted by a strong light source (e.g. a laser) oscillate into WISPs before a wall that is opaque for SM particles. The WISPs traverse the wall and reconvert to photons behind the wall, which will be measured by a detector. The white blobs illustrate that the WISP-photon oscillation may require additional particles, e.g. photons for ALPs, not shown here.

TeV Transparency

Another puzzling observation is the transparency of the universe for γ rays at very high energies ($\gtrsim 100\,\mathrm{GeV}$, VHE) [59]. At these energies it is expected that the VHE photons interact with the extra-galactic background light via pair production such that the intrinsic spectrum of a VHE γ ray source gets distorted. However, observations show that even using lower-limit models of the extra-galactic background light over-corrects the observed spectra. This tension can be relaxed if a conversion of VHE photons to axions in, e.g. , the intergalactic magnetic field and a reconversion of the axions in the galactic magnetic field is included. Using optimistic values for parameters of the galactic fields a lower limit of

$$g_{\mathrm{a}\gamma} \gtrsim 10^{-12}\,\mathrm{GeV}^{-1} \qquad \text{for} \qquad m_{\mathrm{a}} \lesssim 10^{-9}\,\mathrm{eV}$$

is stated, which overlaps with the white dwarf hint.

2.5.3 Laboratory-based Experiments

Some of the above observations put strong bounds on the WISP parameter space. However, all of them rely on models of the DM distribution or the stellar evolution in the wider sense. While these models are generally reliable, a non-negligible uncertainty remains. For example, an additional WISPy component of $\sim 10\,\%$ of the total luminosity can be incorporated in the solar model without contradicting observations [95]. Hence, it is desirable to have full control over the production of the WISP and its propagation and detection in a laboratory experiment.

LSW

Experiments of the light-shining-through-a-wall type (LSW) exploit that WISPs interact very weakly with ordinary matter and can thus traverse barriers that are otherwise opaque for SM particles[7]. Simplistically, such an experiment consists of a strong light source, a "wall" as barrier, a sensitive photo-detector, and in an axion search a magnet, which encloses the setup (cf. Fig. 2.5). Photons oscillate to WISPs before the wall, which the WISPs can pass. Behind the wall, these WISPs oscillate back to photons, which the detector can sense. The rate of

[7] Neutrinos excluded. But the SM-probability for e.g. a photon traversing such a barrier via an intermediate (anti-)neutrino pair, $\gamma \to \nu\overline{\nu} \to \gamma$, is negligible [96].

detected photons, $\dot{N}_{\mathrm{det}}$, is given by

$$\dot{N}_{\mathrm{det}} = \eta\, \mathcal{P}(X \to \gamma)\, \mathcal{P}(\gamma \to X)\, \dot{N}_{\mathrm{prod}} \,, \tag{2.20}$$

where X denotes a WISP, η is the efficiency of the detector, $\mathcal{P}$ the probabilities for WISP-photon and photon-WISP oscillation as calculated in Sec. 2.4, and $\dot{N}_{\mathrm{prod}}$ the photon rate of the source.

Combining Eqs. (2.9) and 2.20 allows to derive a rough estimate of the sensitivity for the axion-photon coupling, $S(g_{\mathrm{a}\gamma})$, of such an experiment. One finds

$$S(g_{\mathrm{a}\gamma}) \propto \frac{1}{B\,L} \left(\frac{\sigma(N_{\mathrm{cnt}})}{\eta\, T\, \dot{N}_{\mathrm{prod}}} \right)^{1/4} \,, \tag{2.21}$$

where the uncertainty on the number of counts, $\sigma(N_{\mathrm{cnt}})$, is set by the noise level of the detector and the duration of the experiment, T. This can be improved, i.e. $S(g_{\mathrm{a}\gamma})$ can be lowered by using a low-noise detector or increasing the magnetic field length, $B\,L$, the efficiency or the initial rate of photons. Different ways have been pursued to achieve this.

Some experiments used very strong pulsed magnets and lasers. Another option is to use a continuous wave laser. Then, the initial rate of photons can be increased by installing an optical cavity in front of the wall. The photons are reflected by the mirrors of the cavity. Therefore, they propagate through the magnetic field multiple times and, effectively, the number of times a photon hits the wall is increased by the power build-up of the cavity, β_{prod}. Installing a second cavity that is in resonance with the first one can further increase the regeneration probability, $\mathcal{P}(X \to \gamma)$ [97, 98]. A technically demanding problem here, is to keep the two cavities in resonance. This will be addressed later in Sec. 4.3.

A number of experiments have been conducted using pulsed lasers [99, 100] and pulsed magnets [101], using continuous wave lasers [102, 103] and optical cavities in front of the wall [51, 104]. There exist also experiments that exploit this LSW scheme in the microwave regime [105]. Up to now, none of these searches has found any light shining through a wall.

Birefringence

In the presence of a strong magnetic field, the quantum electro dynamics (QED) vacuum shows birefringence [106]. The presence of axions changes this in two ways [107]. First, assuming linearly polarized light with some angle between the direction of the magnetic field and the polarization, the oscillation of photons polarized perpendicular to the magnetic field into axions diminishes this component and changes the plane of polarization. Second, the axion-photon mixing of the component polarized perpendicular to the magnetic field changes the birefringent properties of the vacuum. Thus, the observed ellipticity is expected to deviate from the QED predictions. A number of experiments searching for this effect were conducted [108, 109]. An important impact had the PVLAS experiment, which observed such an anomalous rotation [110]. This motivated construction of a number of experiments. Together with PVLAS [111], these experiments excluded the corresponding WISP parameter region and, hence, ruled out the initial PVLAS result. As the next-generation experiments will

have sensitivities in the reach of the QED expectations improving the bounds from these kind of experiments beyond $g_{a\gamma} \sim 10^{-7}\,\mathrm{GeV}^{-1}$ will be difficult [45].

Fifth Forces

The photon-HP mixing leads to a modification of the Coulomb potential, V, between two unit charges [45]

$$V = \frac{\alpha_{\mathrm{em}}}{r}\left(1 + \chi^2\, e^{-m_{\gamma'} r}\right) ,$$

where $\alpha_{\mathrm{em}} = e^2/4\pi$ is the fine structure constant and r is the distance of the two charges. Hence, constraints on an electromagnetic fifth force [60] derived from a more than 40 year old experiment [112] directly translate into an upper limit on the HP kinetic mixing.

Combining all these observations allows to draw "WISP maps" showing the excluded and hinted parameter regions as shown in Figs. 2.3 and 2.4.

Chapter 3

Direct Axion-like Particle Constraints from Red Giant Stars

The potential production of WISPs in stellar cores and the associated energy loss is used to derive constraints on the WISP parameters as discussed in Sec. 2.5.2. Helioscopes directly search for ALPs from the Sun. They exploit that the produced ALPs propagate unhindered from the solar core to an observatory on Earth. The observatories consist of a strong magnetic field, where the reconversion a $\rightarrow \gamma$ takes place, and an X-ray detector as the photons in the solar core are in the X-ray regime.

The solar atmosphere is highly active and, thus, highly luminous in X-rays. Therefore, it is difficult to search for a signal from ALPs that reconvert to X-ray photons in the magnetic field of the heliosphere. However, every stellar core is a potentially luminous ALP source. Stellar objects with a sufficiently inactive atmosphere do not emit X-rays. If the core temperature of such an object is sufficiently high, the thermal photons and, hence, also the produced ALPs have energies in the X-ray regime. The ALPs can escape the core. While they traverse the galactic magnetic field (GMF) of the Milky Way, they oscillate with X-ray photons. Hence, in the presence of ALPs, an inactive-surface stellar object can be luminous in X-rays if its core temperature is sufficiently high. The absence of such an X-ray signal allows to constrain the ALP parameter space. α-Ori (Betelgeuse) has these properties and the non-observation of α-Ori in X-rays was used to constrain the ALP-photon coupling $g_{a\gamma} < 2.5 \times 10^{-11}\,\mathrm{GeV}^{-1}$ for mass-less ALPs [113].

In this chapter, this method will be extended to constrain $g_{a\gamma}$ for massive ALPs. After a description of the current model of stellar evolution in the first section, the properties of α-Ori, modelling of its stellar interior and X-ray observations with the instruments aboard the Chandra X-ray Observatory will be presented in the second section. Followed by a calculation of the ALP production rate and the conversion probability in the GMF which leads to estimates of the expected X-ray count rate with Chandra and other X-ray observatories. In the last section, the result ($g_{a\gamma} \lesssim 1.8 \times 10^{-11}\,\mathrm{GeV}^{-1}$) of this analysis is presented.

3.1 Stellar Evolution

The luminosity, L of a star is related to its radius, R, and the effective temperature of its surface, T_e, by the Stefan-Boltzmann law [114, Sec. 3.4]

$$L = 4\pi\, R^2\, \sigma\, T_\mathrm{e}^4 \,, \tag{3.1}$$

where

$$\sigma = \frac{2\pi^5\, k^4}{15 c^2\, h^3} = 5.6704 \times 10^{-8}\, \mathrm{W\,m^{-2}\,K^{-4}}$$

is the Stefan-Boltzmann constant. According to this equation, a contracting object must be heated to maintain its initial luminosity. Another important relation for the understanding of stellar evolution is the virial theorem [114, Sec. 2.4] stating that for a gravitationally bound system in equilibrium the time-averaged gravitational potential energy, U, is twice the total energy, E,

$$E = \frac{1}{2}\, U \,.$$

Hence, for a collapsing object, the gravitational potential energy released during the collapse has to be radiated away in order to maintain equilibrium.

3.1.1 Star Formation

The current model of stellar evolution[1] assumes that proto-stars are formed by the gravitational collapse of clouds in the interstellar medium (ISM). Under the condition that the cloud is initially free of rotation, turbulence or magnetic fields, the critical mass for the gravitational collapse is given by the Bonnor-Ebert mass, $M_\mathrm{BE} \propto T^2$, where T is the temperature of the cloud [114, Sec. 12.2]. At the beginning of the collapse, the cloud is optically thin. Therefore, the released gravitational potential energy can be radiated away and the cloud is not heated. At some point, the density of the medium at the center of the cloud becomes optically thick. At this point, the collapse of the central region, the proto-stellar core, becomes adiabatic and the central temperature starts to increase. Hence, the Bonnor-Ebert mass increases and the proto-stellar core stops to collapse any further. Instead, it becomes nearly hydrostatic. When the central temperature is high enough ($\sim 2000\,\mathrm{K}$), molecular hydrogen dissociates. Because this process absorbs energy, the core becomes unstable and a second collapse occurs until hydrostatic equilibrium is re-established. This process is followed by a phase of quasi-steady accretion, which ends when the mass of the initial cloud has been consumed.

The end of this accretion phase marks the begin of the pre-main-sequence evolution. The proto-star has become a pre-main-sequence star (PMS). The PMS continues to contract quasi-statically. The released gravitational potential energy is the main source of energy during this phase of stellar evolution. The temperatures of the core and of the envelopes surrounding it increase. Formation of H^- in the surrounding envelopes result in an increased opacity. This causes the formation of a convective zone, which can reach to the center of the core. The energy which is released by the gravitational contraction is efficiently transported by convection and radiated away from the surface of the PMS. This

[1] The following overview is taken from Chaps. 12, 13, and 15 of Carroll and Ostlie [114].

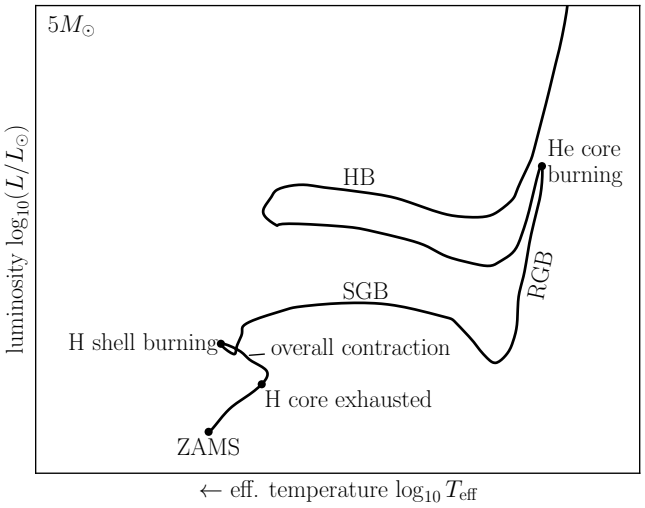

Figure 3.1: Schematic Hertzsprung-Russel diagram for the evolution of a $5\,M_\odot$ mass star. Note that by convention the effective temperature points to the left. The evolution is shown starting at the zero-age main sequence (ZAMS). Notable events and phases during the evolution are annotated. Refer to the text for more information. (Adapted from Carroll and Ostlie [114])

causes the temperature to increase very slowly. Hence, according to Eq. (3.1), the luminosity decreases much more rapidly due to the contraction.[2] The increasing temperature of the core cause a decrease of the opacity and a radiative core develops which increases in size, i.e. the convective envelope shrinks. This causes a rise of the temperature and, accordingly, also of luminosity. Eventually, the temperature in the core is high enough to support nuclear fusion. This additional source of energy causes a temperature rise further. Eventually, the energy produced by nuclear fusion is so high that the core expands slightly. The necessary gravitational potential energy causes a cooling and an according decrease of the luminosity. Then, the core reaches an equilibrium for the rates of the fusion reactions which consume hydrogen and the energy from nuclear fusion becomes the dominant source. The star has reached the main sequence. This stage is known as zero-age main sequence (ZAMS). Stars with masses $0.08 < M/M_\odot < 0.3$ do not develop a radiative core and reach the their ZAMS stage while being fully convective [115, Sec.5.1].

3.1.2 Evolution of ZAMS Stars

During the main sequence phase, a star consumes its hydrogen content in nuclear burning. The nuclear burning in low-mass stars ($0.3 < M/M_\odot < 1.2$) is dominated by the proton-proton chain. These stars have a radiative core. In stars with higher masses, the highly temperature dependent CNO cycle is

[2] The trajectory in the Hertzsprung-Russel diagram during this phase is known as the Hayashi track.

present and, consequently, these stars have a convective core. The evolution in the Hertzsprung-Russel diagram, i.e. in the plane of luminosity, L, and effective surface temperature, T_{eff}, is schematically shown for a $5\,M_\odot$ mass star in Fig. 3.1.

As the fusion of hydrogen to helium proceeds in a star, its core temperature and, thus, the region where fusion takes place increase. When the hydrogen in the central core has depleted, a helium-enriched core remains, which contracts. Hydrogen burning continues in a shell around the core. The contraction of the core causes the shell to expand, which results in a decrease of the effective temperature. This phase is called subgiant branch (SGB). The decreased temperature allows H^- ions to form in the outer envelopes of the star. This increases the opacity. Hence, similar to the process during star formation, a convective envelope forms, which efficiently transports the energy produced in the hydrogen-burning shell to the surface. As the outer diameter of the envelope increases, the luminosity of the star rises. The trajectory in the Hertzsprung-Russel diagram during this phase is called red giant branch (RGB). At the same time, the helium core continues to contract. For stars with masses, $M \lesssim 1.8\,M_\odot$, this process ends with an abrupt onset of the triple alpha process,

$$ {}^4_2\mathrm{He} + {}^4_2\mathrm{He} \rightleftharpoons {}^8_4\mathrm{Be} \quad \text{and} \quad {}^8_4\mathrm{Be} + {}^4_2\mathrm{He} \rightleftharpoons {}^{12}_6\mathrm{C} + \gamma \; . $$

This is known as the "helium core flash". In heavier stars, helium burning sets in more quietly.

In stars with masses $M \lesssim 8\,M_\odot$ the core expands with the onset of helium burning. The hydrogen-burning shell is pushed outwards and cools. Because the luminosity is dominated by the energy produced in the hydrogen-burning shell, the luminosity decreases. Consequently, the convective envelope contracts and the effective temperature increases. As this process continues, a contracting carbon-oxygen core forms with an surrounding helium-burning shell and a resulting decrease of the effective temperature (similar to the helium core and the resulting cooling in the earlier post-ZAMS evolution).

Similar to the evolution during the RGB, a convective envelope forms, which results in an increasing luminosity at an almost constant effective temperature. At the same time, these stars lose mass to the ISM due to mechanisms not yet understood. Hence, one is confined to describe the observations. For stars with masses $M < 8\,M_\odot$ the size of the envelope above the hydrogen- and helium-burning shells decreases as the mass loss continues and, finally, the nuclear reactions stop. The cloud that has formed from the ejected matter becomes optically thin and reveals the remaining core, which consists of the products of the nuclear reactions. This core continues to cool and becomes a white dwarf.

Stars with masses $M \gtrsim 8\,M_\odot$ evolve differently compared to the low-mass evolution described above. When they reach the phase that corresponds to the RGB during the low-mass evolution, they are much larger than low-mass stars and, thus, their luminosity is much higher. Therefore, these stars are referred to as red supergiants (RSGs). The temperature in the contracting carbon and oxygen rich core becomes high enough to support the nuclear burning of carbon and heavier elements up to iron (the element with the highest binding energy per nucleon). The interior of such a star is expected to have an onion-like structure: A core burning heavy elements is surrounded by a sequence of shells burning lighter elements. Eventually, the core of such a star collapses resulting in a supernova explosion.

3.1.3 Simulating Stellar Evolution

In this study, the EZ-Web interface [116] to the "Evolve ZAMS" code [117] has been used. It is an improved version of the code written by Eggleton [118–121]. The code allows the evolution of stars with initial masses ranging from $M_{\mathrm{ini}} = 0.1$ to $100\,M_\odot$ and initial metallicities[3] ranging from $Z = 0.0001$ to 0.03. It contains a set of pre-computed, spherical symmetric models of ZAMS stars, which are used as starting points of the simulation. An initial model that fits the chosen initial mass and metallicity is then evolved by solving the governing system of differential equations numerically (see App. A.3). These computations are valid until hydrodynamical effects become important. At this point, the simulation is stopped.

3.2 α-Ori

α-Ori is a red supergiant (RSG) at galactic longitude $l \approx 199.8°$ and latitude $b \approx -9.0°$ with spectral type M2Iab [122]. Since its properties are well studied, it makes a perfect candidate to study X-ray emission due to ALPs.

A recent estimate of the parallax using radio observation of α-Ori yielded $\pi = (5.07 \pm 1.01)\,\mathrm{mas}$[4] corresponding to a distance of $d = (197 \pm 45)\,\mathrm{pc} \approx 643\,\mathrm{ly}$ [123], which differs from previous estimates of the parallax $(6.55 \pm 0.83)\,\mathrm{mas}$ ($d \approx 153\,\mathrm{pc}$) [124]. Its surface temperature is estimated to be $T_{\mathrm{eff}} = (3641 \pm 53)\,\mathrm{K}$ [125]. Its atmosphere is expected to be inactive in the X-ray regime [126]. Based on the distance, estimates were derived for the luminosity, $\log_{10}(L/L_\odot) \simeq (5.10 \pm 0.22)$, the initial mass, $M_{\mathrm{ini}} \approx 20\,M_\odot$, and the age, $t \approx 10\,\mathrm{Myr}$ [123]. In the literature, mass values ranging from 8 to $20\,M_\odot$ can be found [127] but the mass range 15 to $20\,M_\odot$ is preferred [128]. An iron abundance[5] of [Fe/H] $= 0.05 \pm 0.14$ indicates a metallicity Z, similar to the Sun ($Z_\odot = 0.0122$) [129–131]. Compared to the solar atmosphere, α-Ori's atmosphere has an enhanced nitrogen content compared to carbon and oxygen indicating that material processed by the CNO-cycle is present at the surface [130, 132].

3.2.1 Modelling of α-Ori

In contrast to other studies (see e.g. [26, 29, 84]), the impact of ALP production on the stellar evolution is not considered here. Instead, it is conservatively assumed that the ALP production does does not change the stellar evolution and, hence, "standard" stellar evolution codes can be used. This assumption is justified by the fact that these codes successfully describe observed stellar evolution.

To calculate the ALP flux produced in the core of α-Ori according to Sec. 2.4.3, it is necessary to model the stellar interior of α-Ori. This was done using the EZ code [116, 117] described above. Fig. 3.2 shows the evolution of model stars

[3] The metallicity, Z, is defined as the mass fraction of all elements heavier than helium: $Z = \sum_{i>\mathrm{He}} m_i/M$, where m_i is the mass of the element-i content of a star with total mass M.

[4] $1\,\mathrm{mas} = 0.001'' =$ one milli arc second

[5] [Fe/H] is defined as $[\mathrm{Fe/H}] = \log_{10}(N_{\mathrm{Fe}}/N_{\mathrm{H}})_{\mathrm{star}} - \log_{10}(N_{\mathrm{Fe}}/N_{\mathrm{H}})_{\mathrm{Sun}}$ with N_X the number density of element X.

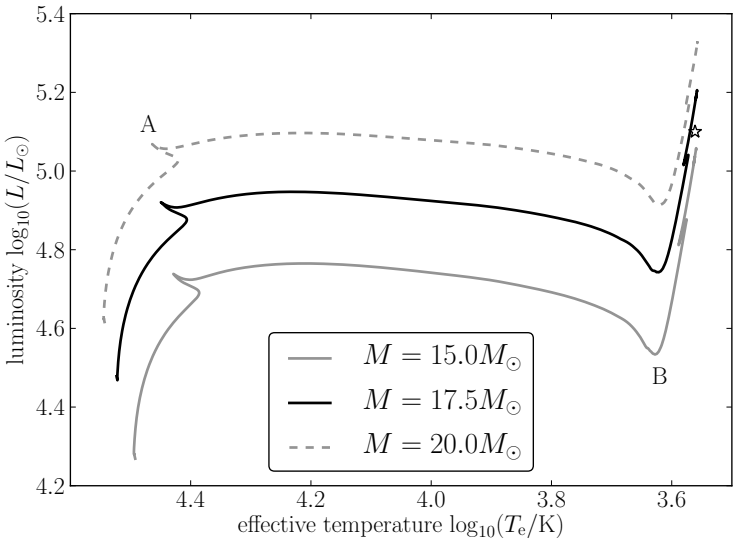

Figure 3.2: Evolution of $Z = 0.01$ stars with the EZ stellar evolution model [116, 117]. Shown are the trajectories in the Hertzsprung-Russel diagram for three model stars with initial masses of 15, 17.5 and 20 $M_\odot$. The evolution is from left to right, i.e. from high to low surface temperatures. The state of α-Ori [123] is marked by a star. The features marked by A and B are discussed in the text.

with initial masses of 15, 17.5 and 20 $M_\odot$ as trajectories in the Hertzsprung-Russel diagram. The initial metallicity is chosen to resemble the solar value $Z_{\mathrm{ini}} = 0.01 \approx Z_\odot$. The start points of the trajectories are the ZAMS state for the corresponding masses. As the star consumes hydrogen, its luminosity increases and its effective temperature decreases slightly. When hydrogen burning stops, the star contracts. The released gravitational potential energy is radiated away. This causes an increase of the luminosity and effective temperature. In Fig. 3.2, this phase is marked by A. At the spike of this feature pointing to the left, hydrogen burning in a shell around the core sets in. The evolution continues along the SGB with decreasing effective temperature. This phase of the evolution ends when a convective zone develops in the outer envelope and the star enters the RGB, which is marked by B in Fig. 3.2.

A comparison with the observed effective temperature and luminosity of α-Ori shows good agreement with the RGB phase of the $M = 17.5\,M_\odot$ model. The state in the evolution of this model nearest to the values of α-Ori is therefore used in the following to calculate the stellar ALP production. This state corresponds to an age of 11.5 Myr in agreement with the above mentioned value of 10 Myr. Fig. 3.3 shows the normed radial profiles of all parameters necessary to calculate the ALP production rate and, additionally, the pressure, P. The profiles of the temperature and the screening scale, Eq. (2.17), are shown in Fig. 3.4. Compared to the model used by Carlson [113] to calculate a $g_{\mathrm{a}\gamma}$-limit, the temperature and screening scale are slighly larger in the core ($R \lesssim 0.4\,R_\odot$). In the outer regions ($R \gtrsim 0.4\,R_\odot$) the temperature and screening scale of our model are below the values of the model of Carlson [113]. Because the differential axion production rate is $\mathrm{d}N_{\mathrm{a}}/(\mathrm{d}V\,\mathrm{d}\omega\,\mathrm{d}t) \propto T \cdot \kappa^2$ (cf. Eq. (2.18)), this model will yield a higher axion production rate and, hence, also a higher value for the expected X-ray count rate than the model of Carlson [113].

3.2.2 X-ray Observations with Chandra

The Chandra X-ray Observatory is a space telescope [133, 134]. It was brought into orbit on July, 23 1999 by a Space Shuttle mission. It began X-ray observations on August, 12 of the same year and is still in operation. X-rays are focussed by a Wolter telescope consisting of 4 shells of Iridium coated glass with a focal length of 10 m. For spectroscopy, two gratings are installed. Two different focal plane detectors are available, which both have an imaging (I) and a spectroscopy (S) component:

1. The High Resolution Camera (HRC) is a microchannel plate. The imaging component has a size of $10 \times 10\,\mathrm{cm}^2$ with a field of view of 31×31 arcmin, an angular resolution of $0.4''$ and an energy range of 0.08 to 10 keV.

2. The Advanced CCD Imaging Spectrometer (ACIS) consists of CCD chips. A 2×2 layout of chips is used for the imaging component, which has a field of view of 17×17 arcmin and a pixel size of $0.5''$. The chips are front-illuminated and their energy range[6] is 0.7 to 11 keV. ACIS-S consists of an 1×6 array of chips with a field of view of 8×8 arcmin and the same pixel size as ACIS-I. The first and last of these chips are back-illuminated.

[6] The energy range is taken to be the range where the quantum efficiency is above 30 %.

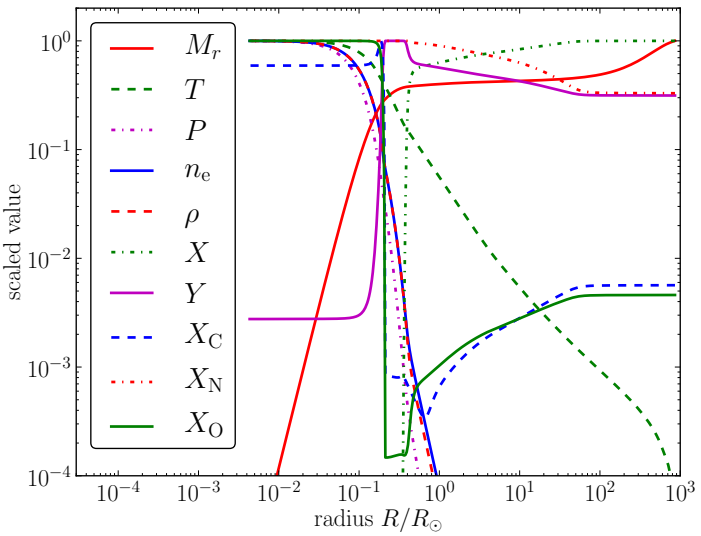

Figure 3.3: Normed radial profiles of the 17.5 $M_\odot$ model. The profiles are normed to their respective maximal values, which are given in parentheses. Shown are the Lagrangian mass, M_r (1.701×10^1 $M_\odot$), temperature, T (2.947×10^8 K), pressure, P (5.820×10^{18} Pa), electron number density, n_e ($8.512 \times 10^{32}\,\mathrm{m}^{-3}$), density, ρ ($2.827 \times 10^6\,\mathrm{kg\,m}^{-3}$), Hydrogen mass fraction, X (6.788×10^{-1}), Helium mass fraction, Y (9.903×10^{-1}), Carbon mass fraction, X_C (1.937×10^{-1}), Nitrogen mass fraction, X_N (6.726×10^{-3}), and Oxygen mass fraction, X_O (8.657×10^{-1}).

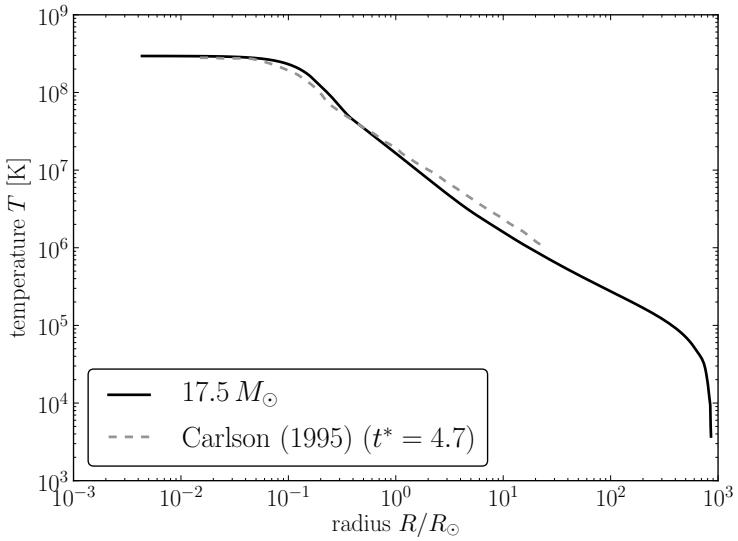

(a) Temperature profile

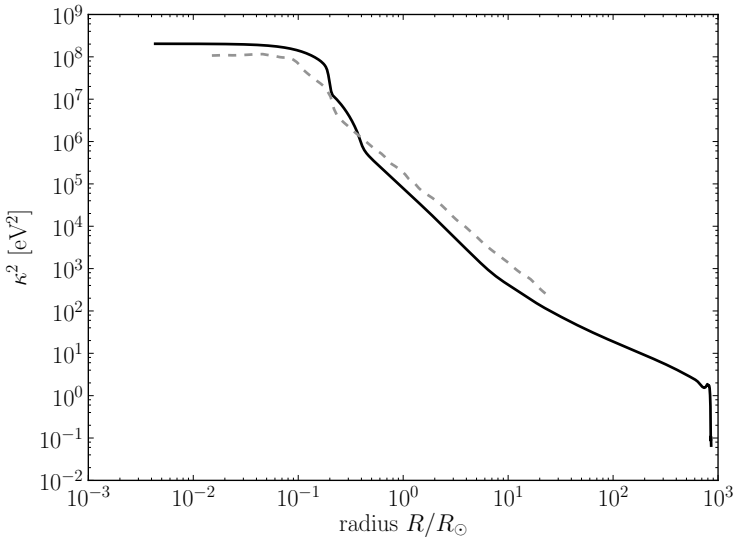

(b) κ^2 profile

Figure 3.4: Stellar profiles of the $M = 17.5\,M_\odot$ model at an age of 11.5 Myr. Shown are (a) the temperature and (b) the square of the screening scale, κ^2, (Eq. (2.17)) as function of the radius, R. The results are compared to the model used by Carlson [113] (dashed grey line).

The energy range of the back-illuminated chips is slightly lower compared to the front-illuminated ones: 0.4 to 10 keV.

From 2001 to 2007, Chandra periodically observed α-Ori as part of the calibration program to monitor the low-energy response of the detectors. The on-axis observations with the ACIS-I, HRC-I and -S detectors were used by Posson-Brown et al. [135] to estimate the X-ray count rate from α-Ori. From the ACIS-I data, events with an energy between 0.3 and 2.5 keV were used. A circle of $3''$ radius around the source location was used as source region, corresponding to 99 % of the instrument's X-ray point-spread function (PSF). The background was estimated from an annulus centered at the source location with an inner radius of $10''$ and an outer radius of $100''$. For both HRC detectors the source region had a radius of $1''$, corresponding to 95 % of the X-ray PSF. An annulus with inner radius $60''$ and a width of $30''$ was used to estimate the background with the HRC-I. The background region of the HRC-S was an annulus with inner radius $35''$ and outer radius $80''$. The leakage of UV emissions of α-Ori expected for these measurements was found to be negligible [135].

Because the method used by Posson-Brown et al. [135] does not include the observed counts in the source region, the unified method [136], which is described below in Sec. 5.3.2, is used here to derive an upper limit on the X-ray counts from α-Ori. The expected background counts in the source region, b, are estimated from the counts in the background region, N_{bgd}, as

$$b = \frac{a_{\mathrm{src}}}{a_{\mathrm{bgd}}} N_{\mathrm{bgd}} \ , \tag{3.2}$$

where a_{src} and a_{bgd} are the angular sizes of the source and background regions, respectively. The source and background counts are assumed to be Poisson-distributed,

$$P(N_{\mathrm{src}}; \theta, b) = \frac{(\theta + b)^n}{n!} e^{-(\theta+b)} \ ,$$

where N_{src} is the total number of counts in the source region and θ the expectation value for the number of counts coming from the source. The resulting 95 % confidence level (CL) upper limits on the count rate are listed in Tab. 3.1. With θ_α being the α-CL upper limit on the counts from the source, the corresponding upper limit on the count rate is given by

$$\dot{N}_\alpha = \frac{\theta_\alpha}{t_{\mathrm{exp}}} \ ,$$

where t_{exp} is the exposure time of the respective measurement.

3.3 X-ray Spectrum due to ALPs

To constrain the ALP-photon coupling with the upper limits on the X-ray count rate from α-Ori obtained in the previous section, it is necessary to calculate the expected X-ray flux due to ALPs which reconvert in the GMF. To this end, it is necessary to calculate the ALP production rate in the core of α-Ori and the conversion probability in the GMF. Combining results of these calculations allows to estimate the expected X-ray count rate. This is done in the following.

Instrument	$t_{\rm exp}$ [s]	Background region $a_{\rm bgd}$ [arcsec^2]	$N_{\rm bgd}$	Source region $a_{\rm src}$ [arcsec^2]	$N_{\rm src}$	b	Upper limit $\theta_{0.95}$	$\dot{N}_{0.95}$ [$10^{-4}\,{\rm s}^{-1}$]
HRC-I	7791	14126	1052	2.66	0	0.20	2.88	3.70
HRC-S	7832	16245	9340	2.66	4	1.53	8.23	10.51
ACIS-I (0.3–2.5 keV)	4897	31102	50	28.27	0	0.05	3.05	6.24

Table 3.1: 95 % CL upper limits on the X-ray count rate from α-Ori measured with Chandra. The table lists the exposure time, the angular size and observed counts in the background and source regions estimated by Posson-Brown et al. [135], the expected number of background counts in the source region (Eq. (3.2)) and the resulting upper limit on the number of source counts and the corresponding source count rate.

3.3.1 ALP Production

Assuming a spherical symmetric stellar interior (as given by the "Evolve ZAMS" code), integrating Eq. (2.18) over the solid angle yields the differential axion production per stellar shell

$$\frac{{\rm d}N_{\rm a}}{{\rm d}r\,{\rm d}\omega\,{\rm d}t} = 4\pi\,r^2\,\frac{{\rm d}N_{\rm a}}{{\rm d}V\,{\rm d}\omega\,{\rm d}t}\ . \tag{3.3}$$

For the $M = 17.5\,M_\odot$ model of α-Ori, this is shown for different photon energies in Fig. 3.5a assuming an ALP-photon coupling of $g_{{\rm a}\gamma} = 10^{-10}\,{\rm GeV}^{-1}$. For X-ray energies ($\omega \gtrsim 1\,{\rm keV}$), the largest contribution comes from the core with $R \lesssim R_\odot$. At extreme ultra-violett energies, e.g. 0.1 keV, the production rate is suppressed in the core compared to X-ray energies but higher in the outer layers. However, this does not compensate the high ALP production rate at X-ray energies in the core as is visible from the ALP spectrum in Fig. 3.5b, which results from integrating Eq. (3.3) over the stellar interior from the center to the outer radius of the model, $R_{\alpha\text{-Ori}}$,

$$\frac{{\rm d}N_{\rm a}}{{\rm d}\omega\,{\rm d}t} = \int_0^{R_{\alpha\text{-Ori}}} {\rm d}r \frac{{\rm d}N}{{\rm d}r\,{\rm d}\omega\,{\rm d}t}\ . \tag{3.4}$$

The spectrum peaks at hard X-ray energies around 50 keV.

3.3.2 a→γ Conversion in the Galactic Magnetic Field

Current observations of the GMF have been reviewed by Beck and Wielebinski [137]. The GMF in the Milky Way is typically considered to consist of a turbulent and a regular component. The regular component has a radial coherence length of $\ell_{\rm reg} \simeq 12\,{\rm kpc}$ [138]. An analytic model of the shape of the regular component of the GMF in the Milky Way does not exist. Two popular descriptive models are the axisymmetric and the bisymmetric configurations shown in Fig. 3.6 [137]. In both cases the field lines are aligned along the spiral arms of the galaxy. In the axisymmetric configuration the rotational orientation of the field lines is the same in all arms while in the bisymmetric configuration the rotational orientation flips from arm to arm. Observations show that a large-scale reversal is present between the local Orion Spur and the Scutum-Crux-Sagittarius Arm

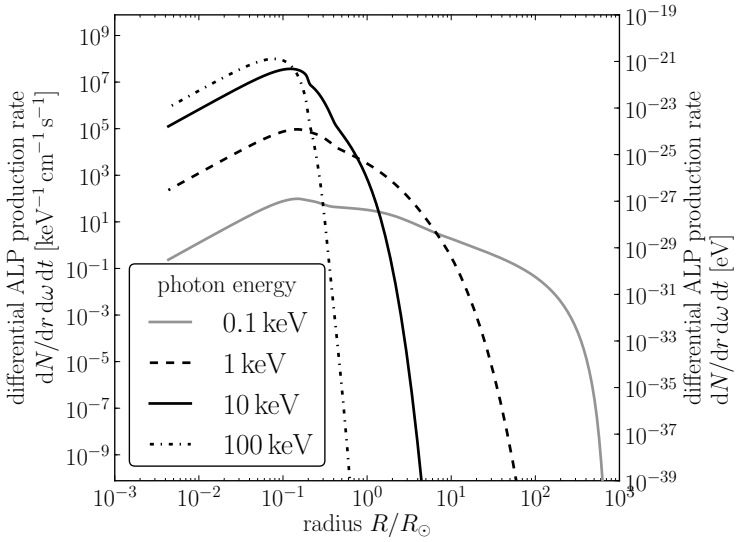

(a) Differential ALP prodution

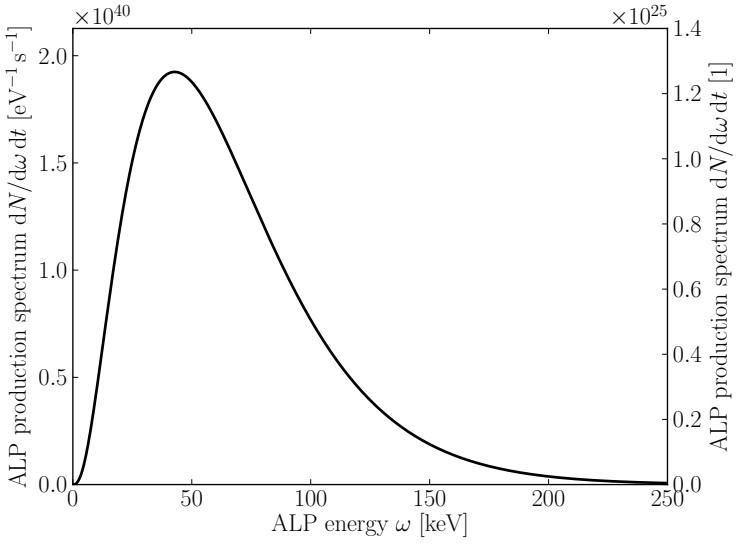

(b) ALP spectrum

Figure 3.5: ALP production in the $M = 17.5\,M_\odot$ model of α-Ori for an ALP coupling to photons $g_{\mathrm{a}\gamma} = 10^{-10}\,\mathrm{GeV}^{-1}$. (a) Radial profile of the differential axion production rate per stellar shell (Eq. (3.3)) for photon energies of 0.1, 1, 10 and 100 keV. (b) Spectrum of the produced ALPs (Eq. (3.4)).

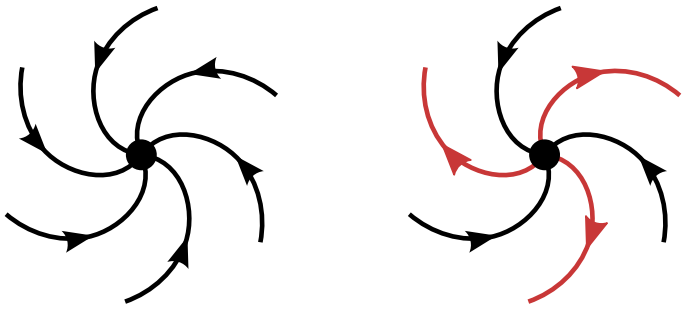

(a) Axisymmetric **(b)** Bisymmetric

Figure 3.6: Axisymmetric (a) and bisymmetric (b) configuration for the regular magnetic field in a spiral galaxy. The lines indicate the spiral arms and the arrows the direction of the magnetic field in the arms.

(cf. Fig. 3.7), supporting a bisymmetric configuration [137]. Apart from this, the axisymmetric configuration fits the observations better [139]. Therefore, currently, no consensus exists about the large-scale field configuration in the Milky Way [140].

For length scales $\ell \lesssim 4\,\mathrm{pc}$, the energy density spectrum of the turbulent magnetic field follows a power law with index $\gamma = -5/3$. For larger length scales, $4\,\mathrm{pc} \lesssim \ell \lesssim 100\,\mathrm{pc}$, the index of the power law is uncertain. Estimations range from $\gamma = -2/3$ to $-5/3$ [141, 142]. To be conservative, an upper limit of the energy density is estimated by assuming $\gamma = -5/3$. Hence, for a wavenumber $k = 2\pi/\ell$, the energy density spectrum, $E(k)$, is given by

$$E(k) = C \left(\frac{k}{k_0}\right)^{-5/3} ,$$

with $C = 9.5 \times 10^{-13}\,\mathrm{erg\,cm^{-3}\,kpc}$ the normalization at $k_0 = 1\,\mathrm{pc}$ [141]. Hence, the energy density in turbulent fluctuations with scales $\ell \lesssim 100\,\mathrm{pc}$ is

$$E(\ell \lesssim 100\,\mathrm{pc}) \approx 3 \times 10^{-13}\,\mathrm{erg\,cm^{-3}} .$$

The corresponding field strength is

$$B_{\mathrm{turb}} \approx 2.7\,\mu\mathrm{G} ,$$

which is of the same order of magnitude as the regular component of the magnetic field discussed below. The ratio of the upper bounds of the probabilities for conversion in a homogeneous (Eq. (2.11)) and turbulent (Eq. (2.12b)) magnetic field with length scale ℓ can be written as

$$\frac{P}{P_{\mathrm{dom}}} = 2\frac{L}{\ell} ,$$

where the same field strength, B, was assumed and L is the total distance travelled. It is obvious from this that the conversion in the turbulent component of the magnetic field can be neglected when observations of α-Ori ($L = 197\,\mathrm{pc}$) are considered.

Several observables can be used to estimate different components of the galactic magnetic field as reviewed by Beck and Wielebinski [137] and Zweibel and Heiles [143]:

- Zeeman splitting of absorption lines of clouds in the ISM can be used to estimate the component of the magnetic field parallel to the line of sight, $B_{\parallel}$.
- Optical light that passed clouds of dust is expected to be linearly polarized parallel to the component that is perpendicular to the line of sight, $B_{\perp}$. The infra-red light emitted by such dust clouds is polarized perpendicular to $B_{\perp}$.
- In the presence of a magnetic field parallel to the line of sight, the free thermal electrons in the ISM cause Faraday rotation. In the ISM, the angle of rotation, ϕ, for a beam of light with wavelength λ is given by [115, Sec. 8.1]
$$\phi = RM\,\lambda^2 \ ,$$
where the rotation measure, RM, is given by
$$RM = \frac{e^3}{8\pi^2\,\varepsilon_0\,m_\mathrm{e}^2\,c^3}\int_\mathrm{los} \mathrm{d}s\,n_\mathrm{e}\,B_{\parallel} \ ,$$
with e the electronic unit charge, ε_0 the permittivity of vacuum, m_e the electron mass, c the speed of light and n_e the density of free thermal electrons. Hence, a regular $B_{\parallel}$ causes a wavelength dependent rotation of the polarization an RM can be measured with multi-wavelength observations. An irregular, e.g. turbulent $B_{\parallel}$ causes depolarization.
- Equipartition of the energy densities of cosmic rays and of the magnetic field is considered a valid assumption [143, 144]. This allows to deduce the strength of $B_{\perp}$ from measurements of the intensity of synchrotron radiation that is emitted by cosmic ray particles gyrating in a magnetic field. The degree of polarization of this synchrotron radiation is sensitive to the randomness of $B_{\perp}$.

To calculate the conversion probability $P_{a\to\gamma}$ for ALPs coming from α-Ori, it is sufficient to know the local configuration within the Orion Spur, where the Sun and α-Ori are located and which is not disputed [137, 145, 146]. Viewing from the galactic north pole, the direction of the field lines is clock wise. From the large-scale diffuse Galactic synchrotron background, the local regular field strength is estimated to be $B_\mathrm{reg} = (4 \pm 1)\,\mu\mathrm{G}$ [147]. As a conservative estimate,
$$B_\mathrm{reg} = 3\,\mu\mathrm{G} = 3\times10^{-10}\,\mathrm{T}$$
will be used, which is in agreement with predictions of models of the GMF [148, 149].

The pitch angle of the Orion Spur at the location of the solar system is $\theta \approx 10^\circ$ [151, 152]. Hence, the spur is pointing at $l_\mathrm{spur} \approx 260^\circ$ and the component perpendicular to the line of sight to α-Ori, $B_{\perp}$, is given by
$$B_{\perp} = B_\mathrm{reg}\cdot G \ ,$$

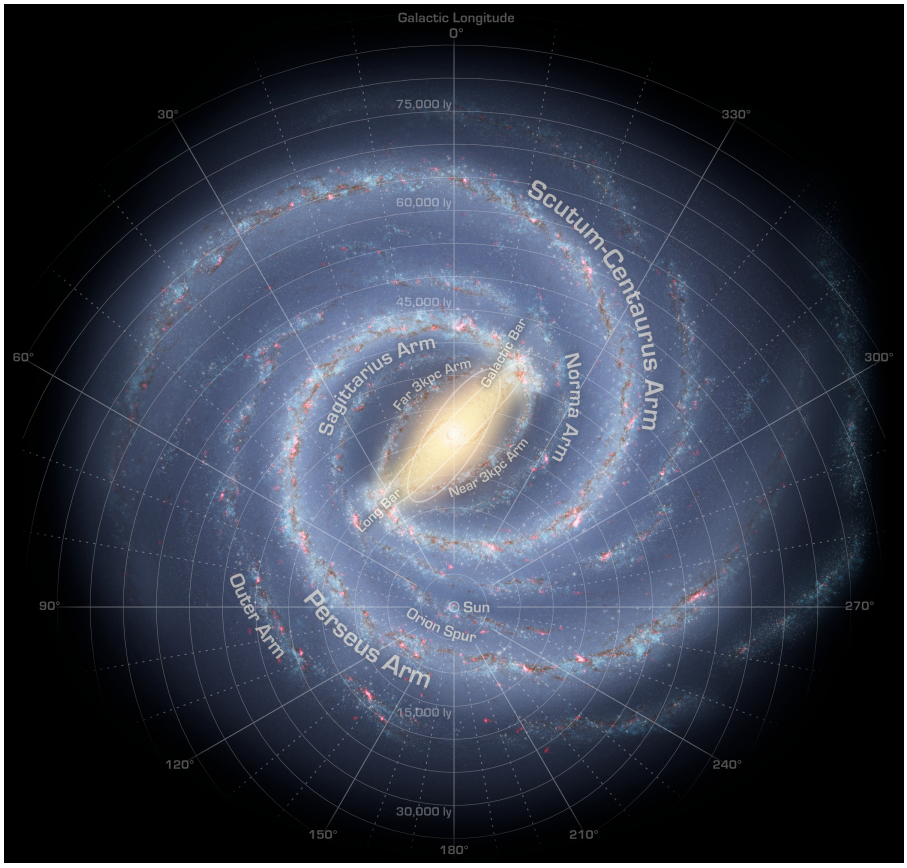

Figure 3.7: View on the Milky Way from the galactic north pole. The location of the solar system is at the center of the polar grid of galactic longitudes. α-Ori is located within the circle around the location of the Sun in the Orion Spur. (Taken from [150])

with

$$G^2 = |\hat{\mathbf{n}}_{\rm los} \times \hat{\mathbf{n}}_{\rm spur}|^2 = 1 - \cos^2 b \, \cos^2(l - l_{\rm spur}) \approx 0.76 \,, \tag{3.5}$$

where $\hat{\mathbf{n}}_{\rm los}$ and $\hat{\mathbf{n}}_{\rm spur}$ are unit vectors in the direction of the line of sight of the observation and the direction of the Orion Spur, respectively. The numerical value is valid for observations of α-Ori.

Although being very thin, the ISM affects the propagation of photons. The index of refraction in the ISM is given by [115, Sec. 8.1]

$$n = \sqrt{1 - \frac{\omega_{\rm pl}^2}{\omega^2}} \approx 1 - \frac{\omega_{\rm pl}^2}{2\omega^2} \,, \tag{3.6}$$

where $\omega_{\rm pl}$ is given by Eq. (2.16) and ω is the photon energy. The approximation holds for $\omega_{\rm pl} \ll \omega$. According to the NE2001 model of the free electron density in the Milky Way [153], the dispersion measure, DM, along the line of sight to α-Ori is

$$DM = \int_{\rm los} {\rm d}s \, n_{\rm e} = 2.6020 \, {\rm pc \, cm^{-3}} \,,$$

i.e. the average free electron density is $n_{\rm e} = DM/d = 0.013 \, {\rm cm^{-3}}$, approximately one half of the value of $\sim 0.03 \, {\rm cm^{-3}}$ typically assumed for the ISM (e.g. [113]). Hence, using Eq. (2.16), one finds for the plasma frequency along the line of sight to α-Ori

$$\omega_{{\rm pl},\alpha\text{-Ori}} \approx 4.23 \times 10^{-12} \, {\rm eV} \,, \tag{3.7}$$

which is much smaller than the expected X-ray energies. Thus, the approximation of Eq. (3.6) can be used. Hence, considering only ALPs with $m_{\rm a} \ll \omega$, Eq. (2.8) can be written as

$$q = \frac{m_{\rm a}^2 - \omega_{\rm pl}^2}{2\omega} \qquad (m_{\rm a}, \omega_{\rm pl} \ll \omega) \,.$$

Because the typical photon energies in a stellar core and, therefore, also the energies of the ALPs and reconverted photons are $\omega \gtrsim 1 \, {\rm keV}$, one finds for the argument of the form factor Eq. (2.10b) with $L = d = 197 \, {\rm pc}$ for α-Ori

$$|q \, L| < 0.01 \qquad \text{if} \quad m_{\rm a}, \omega_{\rm pl} \lesssim 2.6 \times 10^{-11} \, {\rm eV} \,.$$

The estimated plasma frequency in Eq. (3.7) fulfills this bound. Hence, the strong mixing expression of the conversion probability, Eq. (2.11), can be used in this mass region, which yields

$$P({\rm a} \leftrightarrow \gamma) \approx \frac{1}{4} \left(g_{{\rm a}\gamma} B_{\rm reg} L\right)^2 \, G^2 \qquad (m_{\rm a} \lesssim 2.6 \times 10^{-11} \, {\rm eV}) \tag{3.8}$$

for the dependence of the conversion probability on the photon-ALP coupling, $g_{{\rm a}\gamma}$, the strength of regular magnetic field component, $B_{\rm reg}$, the distance to α-Ori, L, and the projection of the line of sight on the direction perpendicular to $B_{\rm reg}$, G (cf. Eq. (3.5)).

Parameter		Value
Distance	d	197 pc
Galactic longitude	l	199.79 °
Galactic latitude	b	-8.96 °
Initial mass	M	17.5 $M_\odot$
Initial metallicity	Z	0.01
Evolution age	t	11.5 Myr
Regular magnetic field	B_{reg}	3 µG
Orion Spur pitch angle	θ	10 °
Free electron density	n_{e}	$0.013\,\mathrm{cm}^{-3}$
Neutral-hydrogen density	$n(\mathrm{H})$	$3.3 \times 10^{20}\,\mathrm{cm}^{-2}$
a-γ coupling	$g_{\mathrm{a}\gamma}$	$10^{-10}\,\mathrm{GeV}^{-1}$

Table 3.2: Parameters used for simulating α-Ori and calculating the photon spectrum at Earth.

3.3.3 Expected X-ray Count Rate

Combining Eqs. (3.4) and (3.8) allows to calculate the differential flux of X-ray photons from a $\leftrightarrow \gamma$ oscillations at Earth,

$$\frac{\mathrm{d}N_\gamma}{\mathrm{d}A\,\mathrm{d}\omega\,\mathrm{d}t} = \frac{1}{4\pi\,d^2}\,P(\mathrm{a} \leftrightarrow \gamma)\,\frac{\mathrm{d}N_\mathrm{a}}{\mathrm{d}\omega\,\mathrm{d}t} \tag{3.9a}$$

$$\approx \frac{g_{\mathrm{a}\gamma}^4 B_{\mathrm{reg}}^2 G^2}{128\pi^3} \cdot \cdot \int_0^{R_{\alpha\text{-Ori}}} \mathrm{d}r\, r^2\, \frac{\omega^2\kappa^2 T}{e^{\omega/T}-1}\left[\left(1+\frac{\kappa^2}{4\omega^2}\right)\ln\left(1+\frac{4\omega^2}{\kappa^2}\right)-1\right], \tag{3.9b}$$

where in the approximation $\omega_{\mathrm{pl}}, m_{\mathrm{a}} \lesssim 2.6 \times 10^{-11}\,\mathrm{eV}$ and a coherence length of the regular magnetic field comparable to or larger than the distance to α-Ori were assumed. Taking $g_{\mathrm{a}\gamma} = 10^{-10}\,\mathrm{GeV}^{-1}$, the spectrum expected from α-Ori is shown in the upper panel of Fig. 3.8. The used parameters are summarized in Tab. 3.2. The five-fold increase in the spectrum compared to the result of Carlson [113][7] is due to (a) the fact that a regular component of $B_{\mathrm{reg}} = 2\,\mu\mathrm{G}$ was assumed by Carlson [113] while a value of 3 µG is used in this work and (b) the difference in the used stellar models as discussed above in Sec. 3.2.1. Compared to these differences, the consideration of the pitch angle of the Orion Spur has only minor effect.

To estimate the count rate, the spectrum has to be folded with the effective area (shown in the lower panel of Fig. 3.8) and the energy response of the instrument used for observation, in our case the different instruments of Chandra. Additionally, absorption of X-ray photons by particles in the ISM may change the spectrum and has to be accounted for. Both was done using PIMMS version 4.6b, which is available on the web [155]. In App. A.2 the column density of neutral hydrogen along the line of sight is estimated to be $n(\mathrm{H}) \approx 3.3 \times 10^{20}\,\mathrm{cm}^{-2}$.

[7] Carlson uses a stellar model evolved to $t^* = 4.7$, where $t^* = \log_{10}(t_{\mathrm{f}} - t)$ and t_{f} is chosen arbitrary near the end of the stars evolution at t_{f} [113, 154].

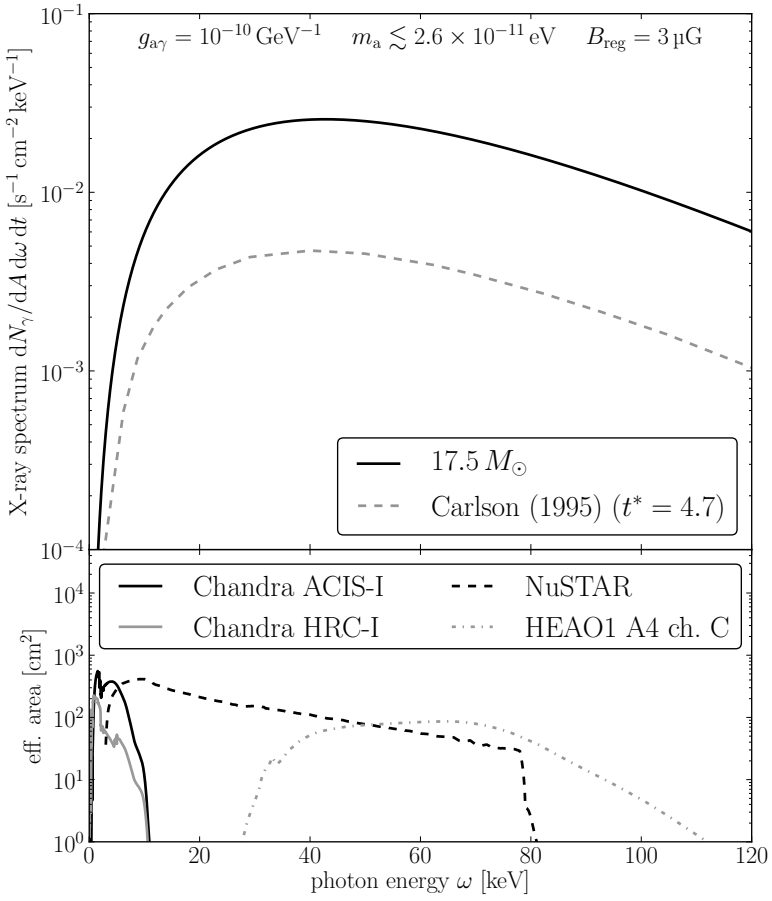

Figure 3.8: Upper panel: Spectrum of photons due to ALP-photon oscillations from α-Ori expected at Earth. The spectrum is calculated using the $M = 17.5\,M_\odot$ stellar model and assuming $B_{\mathrm{reg}} = 3\,\mu\mathrm{G}$ and $g_{a\gamma} = 10^{-10}\,\mathrm{GeV}^{-1}$. All relevant parameters are listed in Tab. 3.2. X-ray absorption in the ISM is not included. The result of this work (black solid line) is compared with the spectrum used by Carlson [113] (grey dashed line). Lower panel: Effective area of detectors. Shown are the effective areas of the Chandra imaging detectors (HRC-I, ACIS-I; the spectroscopic devices of Chandra (HRC-S, ACIS-S) have similar effective areas) and NuSTAR as distributed with PIMMS [155] and of channel C of the low energy detector LED-1 of the A-4 instrument of HEAO1 (the effective area of channel C of LED-2 is similar to that of LED-1; [156]).

This result is obtained from a list of measurements of interstellar column densities along lines of sight near α-Ori compiled by Gudennavar et al. [157]. The resulting expected count rates do not depend strongly on $n(\mathrm{H})$, e.g. increasing $n(\mathrm{H})$ by one order of magnitude causes a relative variation of the expected count rates of at most 3 %. Hence, this rough estimate of $n(\mathrm{H})$ can be used.

The expected count rates are listed in Tab. 3.3. In addition to the expected count rate with the Chandra instruments, the count rate expected for the NuSTAR mission, which was launched in June 2012 [158], over its complete energy range of 3 to 78.4 keV was calculated, which yields $\dot{N}_{\mathrm{exp}} = 2.219 \times 10^2\,\mathrm{s}^{-1}$.

For comparison with Carlson [113], the count rate expected for channel C of the UCSD/MIT Hard X-Ray and Low-Energy γ-Ray instrument (A-4) aboard the HEAO1 satellite [156] was calculated. The A-4 instrument consisted of two low energy detectors (LED-1 and LED-2) with a nominal energy range of 13 to 180 keV. An all-sky survey was performed with HEAO1 between August 1977 and January 1979. The position of α-Ori was scanned three times during this survey but no source was found at the 6σ level [113, 156].

Carlson [113] chose channel C (40 to 80 keV) to estimate an upper limit on the ALP-photon coupling for massless ALPs. He found an expected count rate of $28\,\mathrm{s}^{-1}$. For the X-ray spectrum expected for the $17.5\,M_{\odot}$ model (Fig. 3.8), the expected count rates are $77.0\,\mathrm{s}^{-1}$ (LED-1) and $77.8\,\mathrm{s}^{-1}$ (LED-2), where typical effective areas of the detectors were used [156]. Thus, the total expected count rate is $\dot{N}_{\mathrm{exp}} = 154.8\,\mathrm{s}^{-1}$. As expected from the five-fold increase of the spectrum (see above), this value is also five times larger than the result of Carlson [113]. Calculations with PIMMS show that X-ray absorption in the ISM changes the expected count rate for channel C on the per mille level. Therefore, X-ray absorption was neglected here.

The count rates from the observation of α-Ori with HEAO1 are not available. Carlson [113] estimated an upper limit of the observed count rate of $0.02\,\mathrm{s}^{-1}$ (at 1σ) from the count-rate uncertainty of a source near α-Ori (0614+091 at $l = 200.9°$, $b = -3.4°$ [156]). Thus, the 95 % CL upper limit on the count rate is given by

$$\dot{N}_{0.95} \approx 0.04\,\mathrm{s}^{-1} \qquad \text{(for HEAO1 A-4 channel C)}. \tag{3.10}$$

3.4 Results

Comparing the observed upper limit on the count rate ($\dot{N}_{\alpha}$, Tab. 3.1 and Eq. (3.10)) against the expectation ($\dot{N}_{\mathrm{exp}}$, Tab. 3.3) allows to constrain the ALP-photon coupling, $g_{\mathrm{a}\gamma}$. Since the X-ray flux in Eq. (3.9) scales as $g_{\mathrm{a}\gamma}^4$ the condition

$$\dot{N}_{\mathrm{exp}} \leq \dot{N}_{\alpha}$$

translates to an upper limit, g_{α}, on $g_{\mathrm{a}\gamma}$,

$$g_{\mathrm{a}\gamma} \leq g_{\alpha} = 10^{-10}\,\mathrm{GeV}^{-1} \left(\frac{\dot{N}_{\alpha}}{\dot{N}_{\mathrm{exp}}} \right)^{1/4}, \tag{3.11}$$

where the normalization to $10^{-10}\,\mathrm{GeV}^{-1}$ corresponds to the value of $g_{\mathrm{a}\gamma}$ used in the calculation of $\dot{N}_{\mathrm{exp}}$. The last column of Tab. 3.3 lists the 95 % CL upper limits, $g_{0.95}$, on the ALP-photon coupling.

Vessel	Instrument	$\dot{N}_{\mathrm{exp}}$ [s^{-1}]	$\dot{N}_{0.95}$ [$10^{-4}\,\mathrm{s}^{-1}$]	$g_{0.95}$ [$10^{-11}\,\mathrm{GeV}^{-1}$]
Chandra	HRC-I	4.148×10^{-1}	3.70	1.73
	HRC-S	4.314×10^{-1}	10.51	2.22
	ACIS-I (0.3–2.5 keV)	7.684×10^{-2}	6.24	3.00
	ACIS-S	2.227	–	–
NuSTAR[a]	(3–78.4) keV	2.219×10^{2}	10.31	0.46
HEAO1	A-4 channel C	1.548×10^{2}	40	1.27

[a]For NuSTAR the 95 % CL sensitivity for a 10 ks long observation of α-Ori is quoted.

Table 3.3: Expected count rate, $\dot{N}_{\mathrm{exp}}$, for the $17.5\,M_{\odot}$ spectrum in Fig. 3.8 for the different Chandra instruments and NuSTAR as estimated by PIMMS version 4.6b [155] and for channel C of the A-4 instrument of HEAO1 [156]. Where appropriate, the last two columns list the 95 % CL upper limit on the count rate, $\dot{N}_{0.95}$, and the resulting upper limit on the ALP-photon coupling from comparison of $\dot{N}_{\mathrm{exp}}$ and $\dot{N}_{0.95}$ (cf. Eq. (3.11)). (See text for details)

For NuSTAR, PIMMS provides an estimate of the background rate, $1.876 \times 10^{-3}\,\mathrm{s}^{-1}$, i.e. the expected number of background counts for an observation with NuSTAR with a duration of 10 ks (comparable to the Chandra observations) is 18.76 counts. Using the unified method (see Sec. 5.3.2 and [136]) the 95 % CL sensitivity is 10.31 counts or, correspondingly, a count rate of

$$\dot{N}_{0.95}^{\mathrm{NuSTAR}} = 1.031 \times 10^{-3}\,\mathrm{s}^{-1}\,,$$

which is slightly larger than the upper limits from Chandra (Tab. 3.1).

The upper limits on the coupling resulting from the observation of α-Ori with Chandra are slightly worse than the result obtained with channel C of the HEAO1 A-4 detector. This is because the energy range of this channel (40 to 80 keV nominal) contains the high-flux part of the spectrum while the energy range of the Chandra instruments (below 10 keV) contains only the low-flux edge of the spectrum. The effective area of the different detectors is shown in the lower panel of Fig. 3.8. Since NuSTAR has a broad energy range extending to 78.4 keV, it is able to detect the high-flux part of the spectrum as well. Consequently, the sensitivity, i.e. the expected limit, from a 10 ks observation of α-Ori with NuSTAR can improve the upper limit by almost a factor of 4 over the result with Chandra.

As an approximate upper limit of this study $g_{\mathrm{a}\gamma} \lesssim 1.8 \times 10^{-11}\,\mathrm{GeV}^{-1}$ is taken from the Chandra results. The Chandra results are chosen because the estimation of $\dot{N}_{0.95}$ is more robust for these results compared to the HEAO1 result. This limit is slightly better than the result of Carlson [113] ($g_{\mathrm{a}\gamma} < 2.5 \times 10^{-11}\,\mathrm{GeV}^{-1}$). From the comparison of the region of the ALP parameter space which is excluded by this result with other constraints in Fig. 3.9 one can see that this limit coincides roughly with the bound from the missing γ-ray burst from SN 1987A (Sec. 2.5.2).

To improve this limit, two possibilities exist. First, the limit can be improved by an increased observation length. This can be achieved additional observations with Chandra of either α-Ori or other RSG stars. However, this will only

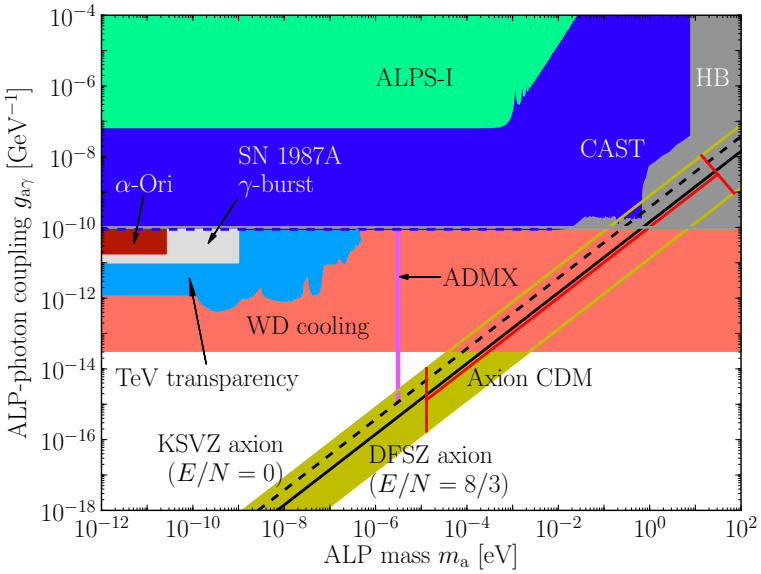

Figure 3.9: ALP parameter space. The parameter space region excluded by the non-observation of X-rays from α-Ori (dark red) is compared with the bound derived from the non-observation of a γ-ray burst associated with SN 1987A (gray) and other constraints and hints which were already shown in Fig. 2.3. See caption of Fig. 2.3 and Sec. 2.5 for details of the different observations.

mildly improve the limit because the upper limit on the count rate is approximately proportional to the root of the observation length, $\dot{N}_\alpha \propto \sqrt{t}$. Hence, according to Eq. (3.11), an improvement in the limit for the coupling by one order of magnitude would require a 10^8-fold increase of the observation length. Compared to this bleak prospect, the second option for improvement seems to be more promising. This option is to observe with a different instrument with an energy range that extends to higher energies compared to Chandra, as e.g. NuSTAR. By this, a larger portion of the X-ray spectrum due to reconverted ALPs (cf. Fig. 3.8), ideally including the peak of the spectrum, can be detected. Unfortunately, most X-ray satellite missions previous to NuSTAR have energy ranges extending to less than 20 keV [158]. Therefore, and considering that an observation with NuSTAR would yield a four-fold improved limit compared to the result determined from the Chandra observations, observations of α-Ori with other X-ray satellite missions are of no big help as well.

Direct searches for HPs coming from stars except the Sun are not possible. This is because the flux at Earth reduces with the distance of a star, d, as $1/d^2$. For HPs this reduction is not countered by an increased conversion probability, P, as it is the case for ALPs due to coherent conversion in the GMF ($P(\mathrm{a} \leftrightarrow \gamma) \propto (B\,L)^2$).

Chapter 4

ALPS-II

To obtain the limit on the ALP-photon coupling from X-ray observations of α-Ori in the previous chapter, it was necessary to make assumptions about e.g. the interior of α-Ori, the configuration of the regular GMF component and the free electron density along the line of sight. These quantities can only be indirectly determined from various observables. Estimates for these quantities from different observables may even give inconsistent results as it is the case for the parallax of α-Ori [123]. Hence, the values are associated with hard-to-quantify uncertainties. This does not mean that the above limit on $g_{a\gamma}$ is meaningless but rather that the interpretation of this limit in terms of confidence level is model-dependent. Thus, to get limits that are less model-dependent, it is desirable to have full control over all aspects of the photon-WISP-photon process. This is the case in experiments of the light-shining-through-a-wall (LSW) type.

The Any-Light-Particle Search (ALPS) experiment was an LSW experiment at DESY [51, 104]. It used a superconducting HERA dipole magnet, an optical cavity to enhance the probability for photon-WISP oscillations and a CCD camera (Princeton Instruments PIXIS 1024B [159]) for detection. Up to now, it is the most sensitive experiment of the LSW kind [103]. Following up on this success, the ALPS-II experiment is under preparation [160]. In the following, the original ALPS experiment will be referred to as ALPS-I to distinguish it from ALPS-II. ALPS-II will re-use the laser components of ALPS-I. In its final phase it will use 2×10 straightened HERA dipoles to increase the magnetic length BL and as first experiment resonant regeneration [97, 98]. For several reasons discussed below, ALPS-II will use infra-red light at 1064 nm. Because of its very low quantum efficiency at this wavelength, it is planned to use the CCD only during commissioning and as backup detector. A transition edge sensor (TES) detector is foreseen as primary detector. These measures will improve the sensitivity by three orders of magnitude compared to ALPS-I (cf. Tab. 4.1). This improvement of the sensitivity will allow not only to confirm astrophysical- and helioscope-based limits on the axion parameters, but in fact ALPS-II will improve over the horizontal branch [26, 29] and CAST [54–56] limits.

ALPS-II will be realized in three steps, denoted ALPS-IIa, ALPS-IIb and ALPS-IIc, shown in Fig. 4.1. The first two steps will not use any magnets and are thus limited to a search for HPs. ALPS-IIa will use two 10 m long optical cavities in the production and regeneration regions. Besides the search

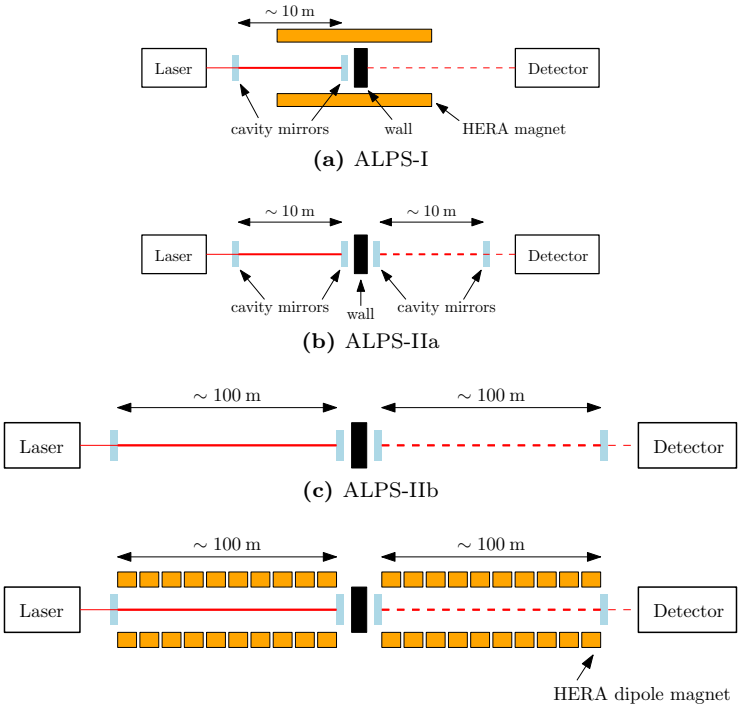

(a) ALPS-I

(b) ALPS-IIa

(c) ALPS-IIb

(d) ALPS-IIc

Figure 4.1: Schematic views of ALPS-I and the different stages of ALPS-II.

for HPs, its main purpose is to prove that the planned locking scheme for the regeneration cavity is working and that the TES can be integrated into the experiment. The second phase, ALPS-IIb, will extend this setup to production and regeneration cavities of 100 m length to show that the two cavities of this length can be successfully locked and that the stronger requirements concerning the alignment of the two longer cavities can be met. The final phase, ALPS-IIc, will then combine this laser setup with 2×10 HERA dipole magnets to search for axions and ALPs.

In this chapter, ALPS-I is reviewed focussing on the technical challenges that led to design decisions for ALPS-II. This is followed by a short presentation of the options that can be used to improve the sensitivity of an LSW experiment and descriptions of the several subsystems of ALPS-II, namely the optical and vacuum systems, the magnets and the detectors, as presented in the technical design report [160]. In the last section, the expected sensitivity for the ALP and HP parameters will be discussed. The characterization of the CCD detector and a description of the statistical analysis of its data follows in Chap. 5.

4.1 ALPS-I

The LSW experiment ALPS-I was performed at the Hamburg site of DESY. A sketch of the setup is shown in Fig. 4.2. The laser light source was a narrow-linewidth master-oscillator power amplifier (MOPA) system initially developed

			Sensitivity on $g_{a\gamma}$	
Parameter	ALPS-I	ALPS-IIc	Scaling exponent	Gain
Circulating laser power	1 kW	150 kW	$-1/4$	3.5
Rel. photon number flux	1	2	$-1/4$	1.2
Reg. cavity power build-up	1	40000	$-1/4$	14
Total magn. length BL	22 T m	468 T m	-1	21
Detector efficiency	0.9	0.75	$-1/4$	0.96
Detector dark current	$10^{-3}\,\mathrm{s}^{-1}$	$10^{-6}\,\mathrm{s}^{-1}$	$1/8$	[a]2.6
Combined				3082

[a]This value includes the effect of the non-zero read-out noise of the CCD used in ALPS-I.

Table 4.1: Comparison of experimental parameters of ALPS-I and the planned experimental parameters of ALPS-IIc. Listed are the numerical values of parameters that affect the sensitivity on the ALP-photon coupling together with the exponent of the approximate scaling of the sensitivity according to Eq. (2.21) and the respective gain in sensitivity between ALPS-I and ALPS-IIc. (Adapted from Bähre et al. [160])

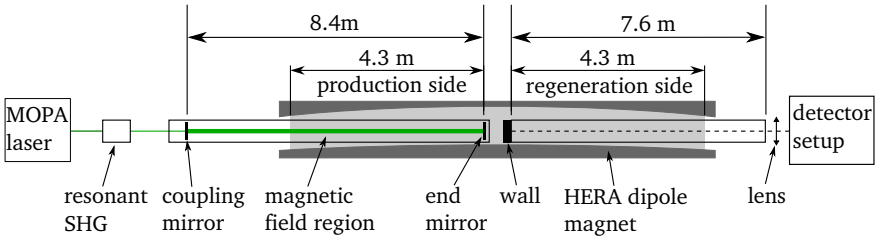

Figure 4.2: Sketch of the ALPS-I setup. (Adapted from Ehret et al. [51])

for gravitational wave detectors [161]. It has a central frequency of 1064 nm. The laser will be described in more detail below as it will also be used in ALPS-II. Second harmonic generation (SHG) was used to produce green light at 532 nm from the IR laser light, because of its easier handling and the better quantum efficiency of the used silicon CCD detector at this wavelength.

The magnetic field of 5 T was generated with a superconducting HERA dipole. The bore of the HERA magnets is at 4.2 K and has a diameter of 55 mm. But because the bore is bent, the free horizontal width is 35 mm. Additionally, an anti-cryostat was inserted into the beam pipe to have an ambient temperature of the end mirror of the cavity of 20 °C. The vacuum tube was inserted into the anti-cryostat. The resulting free aperture had a cat-eye shape with horizontal width of 14 mm [162].

In a first setup [104] the mirrors of the optical cavity were installed outside the vacuum tube. Hence, the photons had to pass the two windows of the vacuum tube twice during one cavity round trip. The associated losses limited the achievable power build-up[1] significantly. Therefore, the mirrors were placed inside the production vacuum tube in an improved setup [51]. The length of this cavity was 8.4 m of which 4.3 m were inside the magnetic field. A power build-up of ~ 300 was reached. The length of the vacuum tube on the regeneration side was 7.6 m with 4.3 m inside the magnetic field. Additionally, a resonant SHG was used. With this the resulting output power was ~ 5 W yielding a stable circulating power of 1.2 kW. The mirrors of the production cavity degraded severely during operation and had to be replaced after several 10 hours. This limited the overall performance of the experiment.

A lens was used to focus the beam of potentially regenerated photons on a Princeton Instruments PIXIS 1024B CCD camera [159], which is described in detail in Sec. 5.2. A stable focussing on 3×3 pixels could be achieved. This setup allowed to put a bound of

$$g_{a\gamma} < 6.4 \times 10^{-8}\,\mathrm{GeV}^{-1} \quad (95\,\%\mathrm{CL}) \qquad \text{for} \quad m_a \lesssim 0.3\,\mathrm{meV}$$

on the ALP-photon coupling, which is currently still the most stringent bound from LSW experiments [103].

4.2 Improving the Sensitivity of an LSW Experiment

The sensitivity of an LSW experiment on the ALP-photon coupling, $S(g_{a\gamma})$, as given by Eq. (2.21) can be written as

$$S(g_{a\gamma}) \propto \frac{1}{B\,L} \left(\frac{R_{\mathrm{DC}}}{T}\right)^{1/8} \left(\frac{1}{\eta\,\dot{N}_{\mathrm{prod}}\,\beta_{\mathrm{PC}}\,\beta_{\mathrm{RC}}}\right)^{1/4} ,$$

where it was assumed that the noise level of the detector, $\sigma(N_{\mathrm{det}})$, is completely determined by the dark count rate of the detector, R_{DC},

$$\sigma(N_{\mathrm{det}}) = \sqrt{T\,R_{\mathrm{DC}}}\,,$$

[1] Defined below in Eq. (4.3).

with B the strength of the magnetic field, L its length, T the duration of the experiment, η the quantum efficiency of the detector, $\dot{N}_{\mathrm{prod}}$ the rate of photons generated by the laser, and β_{PC} (β_{RC}) the power build-up of an optical cavity in front of (behind) the wall. Therefore, several options are available to improve, i.e. lower, the sensitivity of an LSW experiment.

The sensitivity on the ALP-photon coupling, $S(g_{\mathrm{a}\gamma})$, is inversely proportional to the magnetic field length, $B\,L$. Hence, increasing the size and strength of the used magnets is the easiest way to improve the sensitivity. Therefore, ALPS-IIc will use 2×10 straightened HERA dipole magnets, which will provide a magnetic length of 468 T m. This results in a tenfold improvement on the sensitivity. Increasing the magnetic length much further by, e.g. , using LHC magnets instead is not possible [160].

Increasing the quantum efficiency above the value of ALPS-I (95 %) is hardly possible. However, lowering the dark count rate is possible and will be achieved in ALPS-II by using a TES detector. Because the sensitivity scales as the eighth root of the duration of the experiment, it is not an option to prolong the experiment in order to improve the sensitivity significantly.

Modifications of the optical system are further options. The effective number of photons in front of the wall, $\beta_{\mathrm{PC}}\,\dot{N}_{\mathrm{prod}}$, can be increased by using a stronger laser or a cavity with a higher power build-up. Additionally, the probability for an a $\rightarrow \gamma$ reconversion behind the wall can be increased by an optical cavity behind the wall that is resonant to the beam of the cavity in front of the wall [97, 98]. Because high power build-ups in this regeneration cavity are possible, the unfavorable scaling of the sensitivity can be overcome. In ALPS-II, both of these modifications will be implemented.

4.3 Optical System of ALPS-II

The modifications of the optical system for ALPS-II contributes the largest factor (~ 59) to the improvement of the sensitivity. The main modifications are the increased power build-up of the production cavity (PC) leading to an increased photon flux in front of the wall and the installation of the regeneration cavity (RC), which is expected to enhance the regeneration probability according to Hoogeveen and Ziegenhagen [97] and Sikivie et al. [98].

To describe the functioning of the PC and RC and the limiting factors, it is necessary to introduce a description of Gaussian beams and optical cavities.

4.3.1 Gaussian Beam and Optical Cavity

The complex amplitude of the electric field of a Gaussian beam, as the one produced by the MOPA laser system, is described by [163]

$$E(r,z) = A\,\frac{w_0}{w(z)}\,\exp\left\{-\left(\frac{r}{w(z)}\right)^2 - ik\left(\frac{r^2}{2R(z)} + z\right) + i\zeta(z)\right\}\,,$$

where A is a constant, r is the distance from the beam axis and z the distance along the beam axis. The width of the beam, $w(z)$, is defined by $E(w(z),z) =$

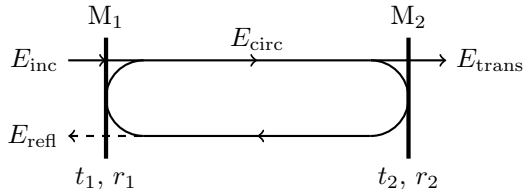

Figure 4.3: Illustration of fields in an optical cavity between two mirrors M_1 and M_2 with amplitude transmission t and reflectivity r. For details see text. (Adapted from Siegman [164])

$E(0,z)/e$ and is given by

$$w(z) = w_0 \sqrt{1 + \frac{z^2}{z_\mathrm{R}^2}} \,,$$

with the Rayleigh range

$$z_\mathrm{R} = \frac{\pi\, w_0^2}{\lambda} \,,$$

$w_0 = w(0)$ the waist of the beam, i.e. the minimal width, and λ the wavelength. The radius of curvature of the surfaces of constant phase, $R(z)$, is given by

$$R(z) = z \left(1 + \frac{z_\mathrm{R}^2}{z^2}\right) \,, \tag{4.1}$$

and $\zeta(z) = \arctan(z/z_\mathrm{R})$ the Gouy phase. At any position z along the beam axis, a fraction of e^{-n^2} of the total power density is outside of the $r_n = n\, w(z)$ contour. At a distance z_R from the waist the beam width grows by a factor of $\sqrt{2}$ and, hence, the area of the beam containing $1 - e^{-n^2}$ of total power density doubles. The divergence angle is given by

$$\theta = \lim_{z\to\infty} \frac{w(z)}{z} = \frac{\lambda}{\pi\, w_0} \,,$$

i.e. one has to compromise between a collinear ($\theta \approx 0$) or thin ($w_0 \approx 0$) beam.

The Fabry-Pérot interferometer is a simple example for an optical cavity. Ideally, it consists of two infinite-sized plane mirrors at distance L. Normal-incident plane waves are reflected by the inner surfaces of the mirrors. They encounter constructive interference and form a standing wave if twice the distance is a multiple of the wavelength,

$$2L = n\lambda \,. \tag{4.2}$$

In this case the intensity between the mirrors can be much higher than the incident intensity.

When constructing optical cavities for lasers, the distance can be much larger than the mirror diameters and the above plane-wave approximation is not valid. Instead, the radius of curvature of the surfaces of constant phase, R, has to be taken into account. Therefore, curved mirrors are used.

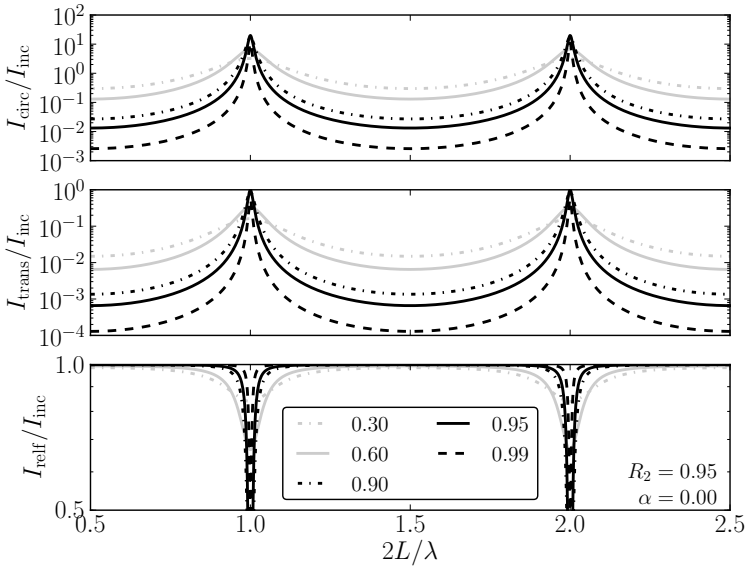

Figure 4.4: From top to bottom: circulating, reflected and transmitted intensity ratio of an optical cavity consisting of two mirrors for a fixed reflectivity of the second mirror of $R_2 = 0.95$ and varying reflectivity of the first mirror. Perfect mirrors ($T + R = 1$) and no losses in the cavity medium ($\alpha = 0$) are assumed. Note that all three panels are shown with logarithmic y-scale.

Fig. 4.3 shows a schematic view of an optical cavity consisting of two mirrors. The incident electric field, E_{inc}, enters the cavity through mirror M_1. A fraction of the electric field circulating between the mirrors, E_{circ}, leaves the cavity through the end mirror M_2. Another fraction is lost through M_1. Together with the reflected portion of E_{inc}, this field component forms the field, E_{refl}, that is reflected by the cavity.

The ratio of amplitudes of the circulating and incident electric fields is given by [164, Chap. 11]

$$\frac{E_{\mathrm{circ}}}{E_{\mathrm{inc}}} = \frac{i\,t_1}{1 - g(\omega)}$$

with

$$g(\omega) = r_1\, r_2\, \exp\left(-\alpha + 2\pi i\, \frac{2L}{\lambda}\right)$$

the amplitude gain of one round-trip where t_k and r_k are the amplitude reflectivity and transmission of mirror k, respectively, and α corresponds to losses in the cavity medium. The resonance condition, Eq. (4.2), is included by the second term in the argument of the exponential. The transmitted and reflected amplitude ratios are given by [164, Chap. 11]

$$\frac{E_{\mathrm{trans}}}{E_{\mathrm{inc}}} = -\frac{t_1 t_2}{1 - g(\omega)}\sqrt{\frac{g(\omega)}{r_1 r_2}} \qquad \text{and} \qquad \frac{E_{\mathrm{refl}}}{E_{\mathrm{inc}}} = r_1 - \frac{t_1^2}{r_1}\frac{g(\omega)}{1 - g(\omega)} \quad .$$

Fig. 4.4 shows the ratio of circulating, transmitted and reflected to incident intensity ($I \propto |E|^2$) for $R_2 = 0.95$ assuming perfect mirrors and no losses, i.e. $T + R = t^2 + r^2 = 1$ and $\alpha = 0$. One can clearly see the increase of the circulating intensity for light fulfilling the resonance condition Eq. (4.2).

On resonance, the ratio of circulating to incident power defines the *power build-up*, β, which can be approximated for $T_1, T_2, \alpha \ll 1$ by [164, Chap. 11]

$$\beta = \frac{I_{\text{circ}}}{I_{\text{inc}}} \approx \frac{4T_1}{(T_1 + T_2 + 2\alpha)^2} \,, \tag{4.3}$$

where $T_k = t_k^2$ is the power transmission of mirror k and perfect mirrors are assumed again. It is maximal when $T_1 = T_2 + 2\alpha$. In this case the reflected amplitude becomes zero. Such a cavity is called impedance matched ($R_1 = 0.95$ in Fig. 4.4). In this situation, for light fulfilling the resonance condition Eq. (4.2), the transmitted intensity equals the incident intensity if $\alpha = 0$, i.e. an impedance matched, lossless cavity is transparent for resonant light.

The distance of the resonance peaks in frequency space,

$$\Delta\nu_{\text{FSR}} = \frac{c}{2L} \,,$$

defines the free spectral range with c the speed of light in the cavity medium. The full-width half maximum of the resonance peak is given in the frequency domain by

$$\delta\nu \approx \frac{1 - |g(\omega)|}{\pi\sqrt{|g(\omega)|}} \, \Delta\nu_{\text{FSR}} \,.$$

The factor

$$\mathcal{F} = \frac{\pi\sqrt{|g(\omega)|}}{1 - |g(\omega)|} \approx \frac{\delta\nu}{\Delta\nu_{\text{FSR}}}$$

is called finesse of the cavity, which is a measure of the resolution power of the cavity. For $|g(\omega)| \approx 1$ it is related to the power build-up by [164, Chap. 11]

$$\beta \approx \frac{T_1 \, \mathcal{F}^2}{\pi^2} \,.$$

Hence, for a low-loss cavity, a high power build-up requires a high finesse.

4.3.2 ALPS-II Optical System

A schematic view of the setup of the optical system of ALPS-II is shown in Fig. 4.5. The narrow-linewidth MOPA laser system of ALPS-I will be used [161]. The Pound-Drever-Hall (PDH) scheme [165] will be used to match the length of the cavities to the frequency of the laser and differential wave-front sensing (DWS) [166] will be used to control the alignment of the laser beams with the optical axis of the cavities. The fundamental part is the "central breadboard", indicated by the beige area in Fig. 4.5. The PC and RC are defined by curved end and plane central mirrors as indicated in Fig. 4.6.

ALPS-II will use the infra-red ($\lambda = 1064\,\text{nm}$) beam produced by the MOPA laser system. This has a number of advantages compared to ALPS-I: First, the SHG step necessary in ALPS-I to produce the green laser beam can be omitted and the full power of 35 W of the laser can be fed to the PC. Second, it is

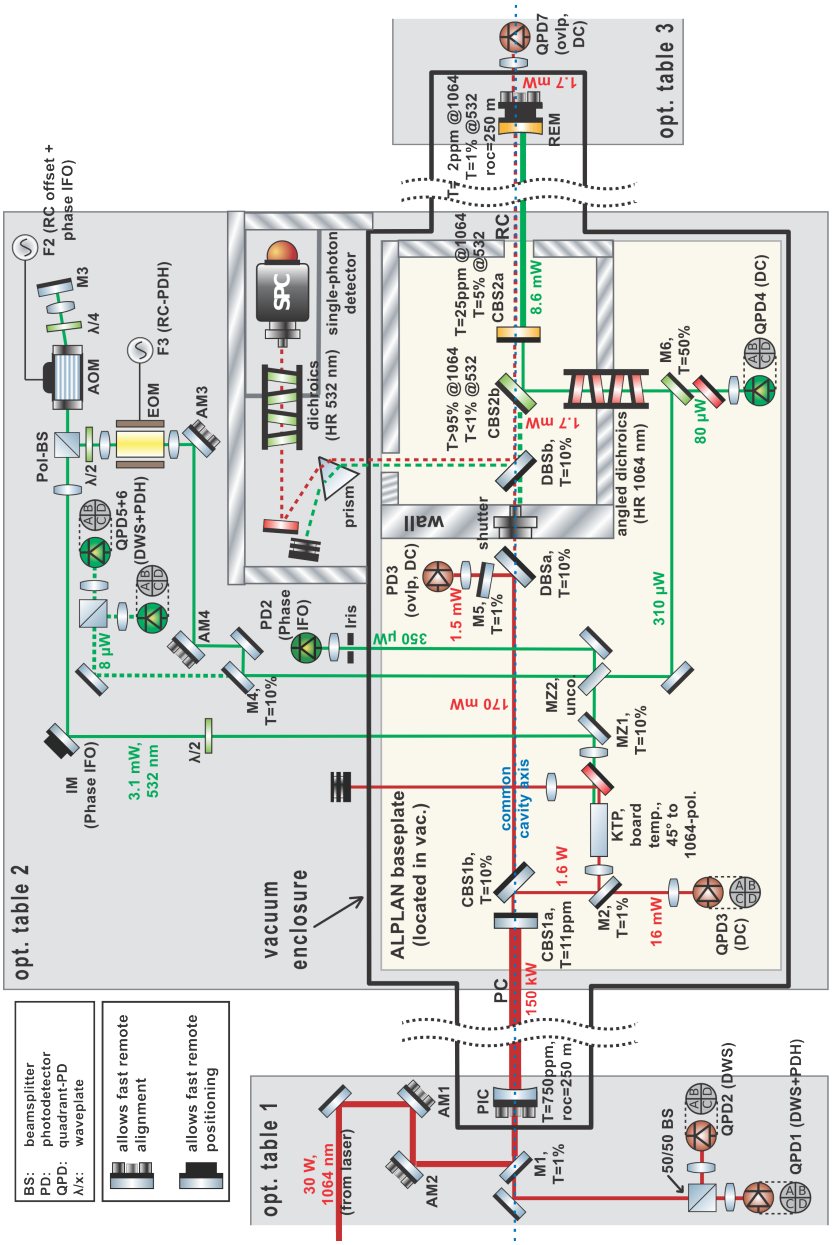

Figure 4.5: Optical layout of ALPS-II. Refer to the text for more information. (Courtesy of R. Bähre)

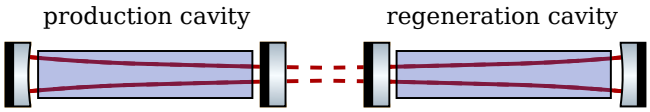

Figure 4.6: Width of the Gaussian beam in the production and regeneration cavity. The mode of the regeneration cavity is an extension of the mode of the production cavity. The shaded areas indicate the beam pipe, which limit the width of the beam at the outer mirrors. (Adapted from Bähre et al. [160])

known from gravitational wave experiments that the mirrors intended to be used in ALPS-II withstand the occurring high intensities at 1064 nm. Hence, a degradation of the cavity power build-up as it was observed in ALPS-I is not expected for ALPS-II. Third, the scheme for locking the PC and RC as elaborated below relies on the possibility to generate a second beam which has a fixed frequency relation to the PC beam. By using an infra-red beam in the PC, this can be easily achieved by SHG of a green beam.

Concerning the stabilization of the PC, the frequency of the MOPA laser is adjusted to match the eigenmode of the cavity, i.e. to correct length variations of the cavity. The frequency sidebands necessary for the PDH sensing are imprinted on the laser signal with an electro-optical modulator built into the laser. The Gaussian laser beam is spatially matched to the eigenmode of the PC by two lenses (not shown in Fig. 4.5) and two mirrors controlled by piezo-electric transducers (PZTs) (AM1 and AM2). A portion of the light reflected by the cavity is directed to two quadrant photo-diodes (QPDs) (QPD1 and QPD2). Lateral and angular misalignment is detected by DWS. For this a lens is placed in front of one of the photo diodes to shift the Gouy phase of the beam by 90° as proposed by Morrison et al. [166]. The differential signals of the QPDs are used to sense tilts and shifts perpendicular to the optical axis of the PC, which is corrected for by the two PZT-controlled mirrors (AM1 and AM2). The sum of the quadrant signals is used for the PDH sensing. To fix the position of the optical axis of the PC with respect to the central breadboard, QPD3 is included in the control loop for the PC.

The stabilization of the RC is even more demanding. In order to enhance the regeneration probability of WISPs, the cavity eigenmode has to be an extension of the eigenmode of the PC [97, 98]. This is achieved by using planar central mirrors in both cavities and curved end mirrors as shown in Fig. 4.6. Hence, the waist of the Gaussian beam is between the central mirrors of the two cavities. To ensure that the eigenmodes of the two cavities overlap, the flat surfaces of the central mirrors are required to be parallel within 10 µrad [160]. The infra-red beam used for locking the RC must not be shifted laterally by more than 1 mm due to optical elements on the central breadboard. These requirements are for the 2×100 m experiments (ALPS-IIb and c). For ALPS-IIa the requirements are slightly less strict.

The beam of green light ($\lambda = 532$ nm) for locking the RC is produced by SHG in a KTP[2] non-linear crystal from the light transmitted by the central mirror of the PC. Remaining infra-red light is filtered by a dichroic mirror. The frequency sidebands for the PDH sensing are again imprinted by an electro-

[2]KTP = potassium titanyl phosphate ($KTiOPO_4$)

optical modulator (EOM). An acousto-optical modulator (AOM) is used to shift the frequency of the green light. This can be necessary in order to achieve resonance of the RC for both the green and infra-red beams. The green beam is then fed to the RC by two PZT-steered mirrors (AM3 and AM4). Again, DWS is used to control tilts and shifts perpendicular to the optical axis of the cavity. PDH sensing is used to stabilize the resonance of the cavity. However, contrary to the PC the frequency of the light is now given by the frequency of the infra-red beam in the PC and cannot be varied. Hence, the length of the RC is adjusted by moving the end mirror with piezo actuators. The position of the green beam with respect to the central breadboard is measured with QPD4.

The procedure to lock the cavities starts with the locking of the PC. After the DWS and PDH control loops including QPD3 are locked, the shutter between cavities is opened and the end mirror position of the RC is varied to lock the cavity for the infra-red beam from the PC with QPD7. Third, the PZT mirrors and the acousto-optical modulator (AOM) are used to make the green beam in the RC collinear to the infra-red beam and lock its frequency to the eigenmode of the RC. The position of the green beam with respect to the central mirror of the RC is then noted by QPD4 and the lock for the green beam in the RC is acquired. In this state the RC is resonant for both the infra-red and the green beam. The lock for the green beam is then hold by actuating the end mirror of the RC. This ensures that this "dual-lock" state is maintained. Finally, the shutter is closed again. In this state, the experiment can search for WISPs.

The maximum achievable power build-up of the production cavity is limited by the damage threshold of the mirrors of a few $\mathrm{MW\,cm^{-2}}$ and the aperture of the beam pipes of the HERA dipole magnets. A higher power build-up results in an increased intensity on the mirrors which requires then a larger beam width to stay below the damage threshold. However, increasing the beam width leads to reflection and diffraction on the wall of the beam pipes, which reduces the power build-up again. To be well below the damage threshold a maximal intensity of $500\,\mathrm{kW\,cm^{-2}}$ is chosen in the design. This corresponds to 150 kW of circulating power or a power build-up of $\beta_{\mathrm{PC}} \approx 5000$ [160]. The transmissions of the PC mirrors are chosen such that the largest fraction of the incoming power is reflected by the cavity. Hence, the PC is not impedance matched.

Assuming an aperture of the magnets of 50 mm and a safety margin of 10 mm to account for an alignment uncertainty of the magnets, a cavity length of 100 m can be achieved [160]. Considering typical mirror losses of 8 ppm, similar losses due to clipping and minimal transmission of the RC end mirror, impedance matching is achieved by a transmission $T_1 \approx 25$ ppm of the central RC mirror. According to Eq. (4.3), this allows for an infra-red power build-up in the RC of $\beta_{\mathrm{RC}}^{\mathrm{IR}} \approx 40000$. For the green beam, the RC is not impedance matched. The power build-up is $\beta_{\mathrm{RC}}^{\mathrm{green}} \approx 60$. The length of the two cavities is chosen to be the Rayleigh range of the Gaussian beam. Hence, the radius of curvature is given by twice the Rayleigh range, $R_{\mathrm{roc}} = 2z_{\mathrm{R}} = 200\,\mathrm{m}$ (cf. Eq. (4.1)). This design proves to have the smallest clipping losses [160].

4.4 Vacuum System

For the vacuum system of ALPS-II, pump stations from HERA will be reused [160]. ALPS-IIa uses spare parts of the vacuum system of the HERA proton ring while straight sections of the HERA proton ring will be used for ALPS-IIb. ALPS-IIc will use the beam pipes of straightened HERA dipole magnets (see next section) as vacuum vessel and oil-free turbo molecular pump stations and NEG pumps, which pump chemically active gases. During cryogenic operation the surface of the beam pipe is at 4.2 K and acts as a cryo-pump.

The roots of the oscillatory terms in the conversion probabilities, Eqs. (2.9) and (2.13), cause gaps in the exclusion curves (cf. for example the ALPS-I curves in Figs. 2.3 and 2.4). To fill these gaps the mass difference between the WISP and the photon has to be modified. This is achieved by tuning the index of refraction in the cavities by inserting a buffer gas. In ALPS-I argon was used for this and this will also be used in ALPS-IIa and ALPS-IIb. In ALPS-IIc argon cannot be used because of the low temperatures of the beam-pipe surface. Instead helium will be used. After insertion, the helium first condensates on the beam-pipe surface. But once the surface is covered by a monolayer of helium atoms, additional helium leads to an increased pressure [160].

The pressure, p_w, will be measured at room temperature, T_w, outside of the cryogenic environment. It is related to the pressure, p_c, in the cryogenic beam pipe at temperature T_c by [160]

$$\frac{p_\mathrm{c}}{p_\mathrm{w}} = \sqrt{\frac{T_\mathrm{c}}{T_\mathrm{w}}} \,. \tag{4.4}$$

The refractive index of helium can be calculated using the Lorentz-Lorenz equation [167],

$$n - 1 = \frac{3}{2} \frac{A_\mathrm{R}\, p}{R\, T} \,,$$

where $A_\mathrm{R} = 0.518\,\mathrm{cm}^3/\mathrm{mol}$ is the molar polarizability and R the universal gas constant. The numerical value is for helium and 1064 nm light. Hence, to achieve a refractive index, n_c, of the cavity medium in the cold bore of the magnets, the helium pressure measured at room temperature has to be

$$p_\mathrm{w} = 3.80 \times 10^6\,\mathrm{mbar} \cdot (n_\mathrm{c} - 1) \cdot \left(\frac{T_\mathrm{c}}{4.2\,\mathrm{K}} \frac{T_\mathrm{w}}{300\,\mathrm{K}} \right)^{1/2} \,. \tag{4.5}$$

To protect the central breadboard from vibrations of the vacuum system (e.g. due to operation of the pumps), it is supported by three posts that are decoupled from vibrations of the vacuum system. Soft bellows are used as feedthroughs. The posts are fixed to an optical table while the vacuum vessel is standing on dedicated posts connected with the laboratory floor.

4.5 Magnets

The second largest contribution to the gain in sensitivity on $g_{\mathrm{a}\gamma}$ is due to the larger magnetic length, BL, which is achieved by increasing the number of HERA dipole magnets (cf. Tab. 4.1). The length of the magnetic field region of the dipoles is 8.83 m with a magnetic field strength of the 5.3 T. At the

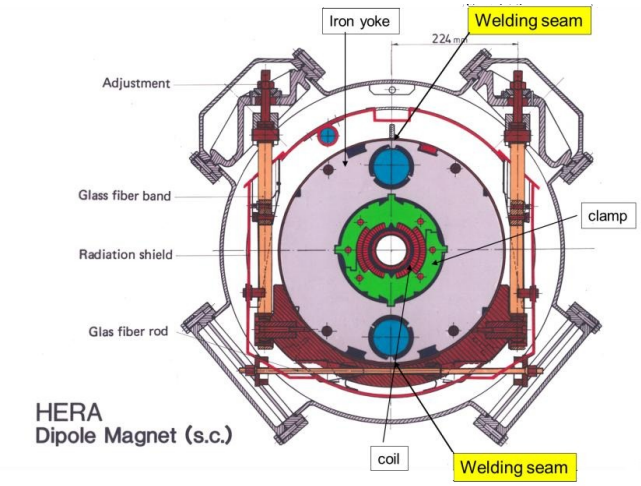

Figure 4.7: Cross section of HERA dipole magnet. (Taken from Bähre et al. [160])

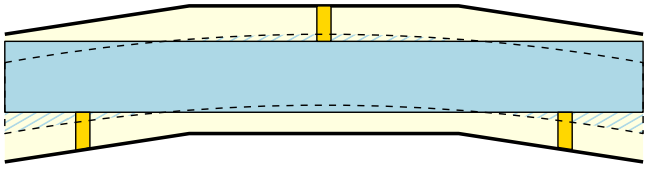

Figure 4.8: Illustration of the straightening of the beam pipe by installing pressure props (orange blocks). The initial form of the beam pipe and surrounding components is indicated by the dashed contour. The light blue shaded solid contour is the final shape of the straightened beam pipe. Note that the true final shape is not perfectly straight but remain bent at the ends [160].

connection of two dipoles the length of the field free region is 0.936 m. A cross section of the dipoles is shown in Fig. 4.7. The beam pipe of the HERA dipole magnets has a diameter of 55 mm. It is surrounded by the super conducting coils of the magnet, clamps and the iron yoke. During fabrication these components were initially straight but forced into a curved shape before the final welding of the two half cylinders that surround the yoke. This limits the usable horizontal aperture of the beam pipes to ≈ 35 mm, which allows for only 2×4 HERA dipoles before clipping losses limit the possible power build-up of the cavities [160].

A simple method to straighten the magnets is to install "pressure props" between the outer polygon-shaped vacuum vessel of the magnets and the half cylinders that contain the yoke as depicted in Fig. 4.8. Two props are installed near both ends of the magnet inside the radius of curvature of the beam pipe. Outside the radius of curvature a third prop is installed at half the length of the beam pipe. First results of this technique show that a horizontal aperture of 50 mm can be achieved. Tests with the magnet used in ALPS-I, which is installed in the magnet test bench of HERA, show that the quench current was not reduced by this mechanical deformation. The measured cryogenic losses showed no difference compared to the unmodified magnet [160].

For the operation during ALPS-IIc the cryogenic infrastructure and power supply of HERA will be reused.

4.6 Detector

The transmission of the central mirror of the RC for infra-red light is chosen to be much higher than the transmission of the end mirror (25 ppm vs. 2 ppm). Thus, regenerated photons from WISP-photon oscillations leave the RC primarily from the central mirror, where the detector will be integrated. The central mirror was chosen to extract the beam of regenerated photons because here the width of the beam is smaller by a factor $\sqrt{2}$ than at the end mirror and the position of the beam is well defined (by the reference point on QPD4). This simplifies the coupling to the detector.

The green beam used to keep the RC locked and the potential infra-red beam from regenerated photons are collinear and have to be separated before they reach the detector to avoid an exposure of the detector to the green beam. To achieve this, a prism is used to separate the beams and the green beam is dumped. After that remaining green photons are filtered by a series of dichroic mirrors that are highly reflective for green light (cf. Fig. 4.5). These filters are designed such that the remaining beam contains green photons at a rate below the dark count rate of the detectors.

A potential background are infra-red photons that enter the RC collinear with the green beam. These can be stray-light photons collinear with the green beam by chance. A second, more important source are photons from the infra-red beam that passed the dichroic mirrors which filter the green beam behind the SHG. These collinear photons are then coupled into the RC and exit it in the same way as the photons from a potential signal. A third source of background can arise from infra-red photons produced by (non-linear) interactions of the green beam with the optical elements, e.g. due to fluorescence. These photons can accidentally be collinear with the infra-red beam and mimic a signal.[3]

To protect the RC from infra-red photons, the RC is separated from the PC by a light-tight shutter box. The inlet for the green beam is guarded by a series of dichroic mirrors highly reflective at 1064 nm ("angled dichroics" in Fig. 4.5). These dichroics and the connections of the shutter box to the baseplate of the central breadboard and to the ports of the central vacuum vessel as well as the installed shutter are tested to match the required attenuation of the infra-red stray light and the remaining infra-red photons in the green beam, which is given by the background rate of the detector.

4.6.1 Transition Edge Sensor

Because of the changed wavelength, the CCD detector used in ALPS-I has a reduced efficiency (cf. Fig. 5.15), which influences the sensitivity negatively. This is discussed in detail below in Sec. 5.4. As alternative detector, a transition edge sensor (TES) is developed in ALPS-II.

Fig. 4.9a sketches the setup of a TES. It consists of a superconducting photon absorber with heat capacity C, which is coupled to a cold bath by a heat

[3] Another source of background is thermal ambient emission, which may be non-negligible if the TES is used as detector.

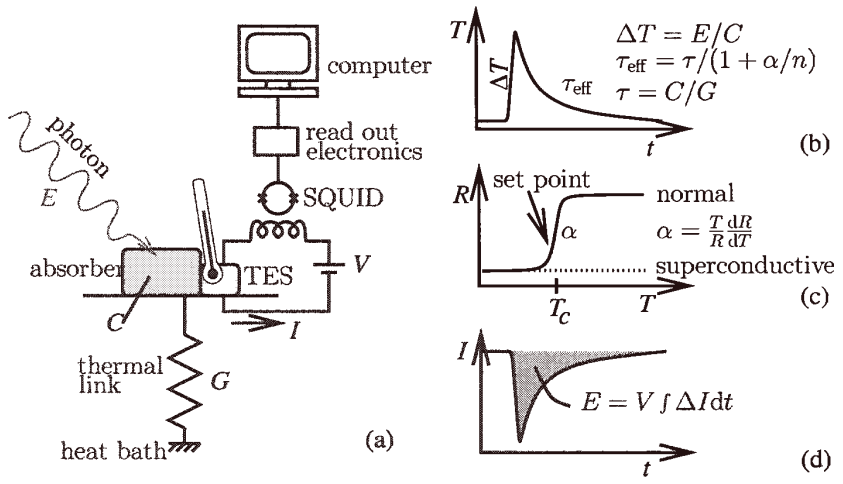

Figure 4.9: TES operating principle. (a) shows the setup. (c) the dependency of the resistance, R, on the temperature of the absorber, T, at the superconducting phase transition. (b) and (d) show the response of the temperature, T, and the current, I, to an absorbed photon, respectively. (Taken from Korte et al. [168])

conductivity, G. The TES is operated at a temperature T_c set at the superconducting phase transition (cf. Fig. 4.9c). The resulting current is measured by a SQUID sensor. When a photon is absorbed, the corresponding energy leads to a temperature rise, ΔT, of the absorber. This results in an increase of the resistance and, hence, a drop in the current measured by the SQUID as shown in Figs. 4.9b to d. Because of the reduced current, the ohmic heat load on the absorber is smaller. The absorber thermalizes with the cold bath with a time constant τ_{eff} and the TES returns to its working point. The integrated current signal is a measure for the absorbed energy E. An energy resolution of $\Delta E/E \approx 8\,\%$ has been measured [169].

The cryogenic environment for the TES and SQUID is provided by an anti-demagnetization refrigerator. Because the TES devices and the SQUIDs are operated at cryogenic temperatures, their intrinsic noise is very low. For ALPS-II a dark count rate of $10^{-6}\,\text{s}^{-1}$ or below is targeted. TES can reach high quantum efficiencies of 95 % for specific photon energies by manufacturing an optical cavity around the absorber material [170].

The signal beam is coupled into an optical fiber, which guides the light to the TES. The sensors under study for ALPS-II were manufactured by NIST and AIST. The coupling of the fiber to the TES is accomplished by modified fiber connectors on the NIST device. The AIST device has a fiber glued to it, which can be spliced to another fiber. Both methods give high coupling efficiencies of $\sim 98\,\%$ [171, 172]. A design value of 75 % is set for the combined efficiency, i.e. including the coupling of the signal into the optical fiber, the transport efficiency of the fiber and the coupling of the signal to the TES sensitive area.

4.6.2 CCD Camera

The integration and operation of the CCD camera is much simpler. The signal beam can be focussed on the chip of the CCD using a lens. A focal spot size of one pixel ($13 \times 13\,\mu\mathrm{m}^2$) is targeted. The working principle, the analysis of the CCD data and the expected sensitivity are described in detail in Chap. 5. Because of the reduced sensitivity, the CCD is foreseen to be used during commissioning and as backup detector in case of unexpected problems with the TES setup.

4.7 Expected Sensitivity

The sensitivity of the experiment on the HP parameters can be easily calculated using Eqs. (2.13) and (2.20). Assuming equal PC and RC lengths, l, the parameter space above

$$\chi_\alpha = \frac{\omega q}{m_{\gamma'}^2 \left|\sin\frac{ql}{2}\right|} \left(\frac{\dot{N}_\alpha}{\eta\,\beta_{\mathrm{PC}}\beta_{\mathrm{RC}}^{\mathrm{IR}}\dot{N}_{\mathrm{in}}}\right)^{1/4}, \tag{4.6a}$$

can be excluded with confidence α, where $\dot{N}_\alpha$ is the α-CL upper limit on the count rate, η the efficiency of the detector setup, β_{PC}, $\beta_{\mathrm{RC}}^{\mathrm{IR}}$ the power build-up of the PC and RC for the infra-red beam, respectively, and $\dot{N}_{\mathrm{in}}$ the rate of photons coupled into the PC. In case of evacuated cavity volumes and $m_{\gamma'} \ll \omega$ Eq. (2.14) becomes

$$q = \frac{m_{\gamma'}^2}{2\omega}$$

and the above simplifies to

$$\chi_\alpha = \frac{1}{2\left|\sin\frac{m_{\gamma'}^2 l}{4\omega}\right|} \left(\frac{\dot{N}_\alpha}{\eta\,\beta_{\mathrm{PC}}\beta_{\mathrm{RC}}^{\mathrm{IR}}\dot{N}_{\mathrm{in}}}\right)^{1/4}, \tag{4.6b}$$

i.e. for small masses $\chi_\alpha \propto m_{\gamma'}^{-2}$.

For axions and ALPs, the form factor (Eq. (2.10b)) has to be modified for ALPS-IIc because the strings of HERA magnets do not provide a continuous magnetic field but are intersected by field-free regions at the connections of the magnets. Assuming that the length of the field-free region, Δ, is the same for each connection, the form factor reads [48]

$$|F(qL)| = \left|\frac{2}{qL}\sin\left(\frac{qL}{2N}\right)\frac{\sin\left[\frac{q}{2}\left(L+\Delta N\right)\right]}{\sin\left[\frac{q}{2}\left(L/N+\Delta\right)\right]}\right|,$$

where N is the number of magnets with a magnetic field region of length ℓ and $L = N\,\ell$ the total length of the magnetic field. The sensitivity on the coupling is given by

$$g_\alpha = \frac{2}{BL\,|F|}\sqrt{\frac{k_{\mathrm{a}}}{\omega}} \left(\frac{\dot{N}_\alpha}{\eta\beta_{\mathrm{PC}}\beta_{\mathrm{RC}}^{\mathrm{IR}}\dot{N}_{\mathrm{in}}}\right)^{1/4}, \tag{4.7a}$$

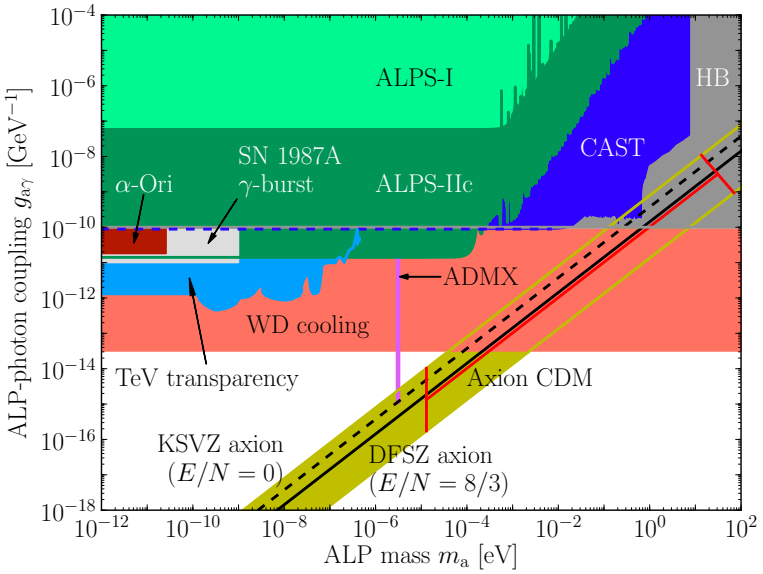

Figure 4.10: Planned 95 % CL sensitivity reach of ALPS-IIc for axions and ALPs (dark green). The sensitivity reach is compared with constraints and hints shown in Fig. 2.3. See caption of Fig. 2.3 and Sec. 2.5 for details of the different observations.

where it was assumed that the magnet strings of the PC and RC are alike. For small masses, $m_a \ll \omega$, the square root becomes unity,

$$g_\alpha = \frac{2}{BL\,|F|} \left(\frac{\dot{N}_\alpha}{\eta \beta_{\mathrm{PC}} \beta_{\mathrm{RC}}^{\mathrm{IR}} \dot{N}_{\mathrm{in}}} \right)^{1/4} . \tag{4.7b}$$

The expected reach of ALPS-II is estimated by the 95 % CL sensitivity (see Sec. 5.3.3). Figs. 4.10 and 4.11 show the sensitivity on the ALP and HP parameters, respectively, expected for ALPS-II using the design parameters mentioned in the previous sections and listed for reference in Tab. 4.2. It was assumed that the detection system of the experiment reaches a quantum efficiency of 75 % and allows to constrain an upper limit on the count rate of $2.15 \times 10^{-6}\,\mathrm{s}^{-1}$. These values correspond to the design efficiency and the expected sensitivity of the TES system as estimated below in Sec. 5.4.

The improvement of three orders of magnitude in the ALP-photon coupling is clearly visible in Fig. 4.10. For masses $m_a \lesssim 10^{-4}\,\mathrm{eV}$, ALPS-IIc will improve over the limits from CAST [54–56], the lifetime of horizontal-branch stars [26, 29] and the limit from X-ray non-observation of α-Ori, which was derived in Chap. 2. ALPS-IIc will cover a portion of the parameter space regions favored by anomalous white dwarf cooling [44, 58] and by the TeV-transparency [59].

Because the longer magnetic length, BL, does not contribute to the conversion probability of HPs, a smaller improvement of ≈ 140 can be achieved. The $m_{\gamma'}$-value of the first minimum in the LSW sensitivity is set by the length of the cavities, l, and the photon energy, ω, while the detector parameters, cavity

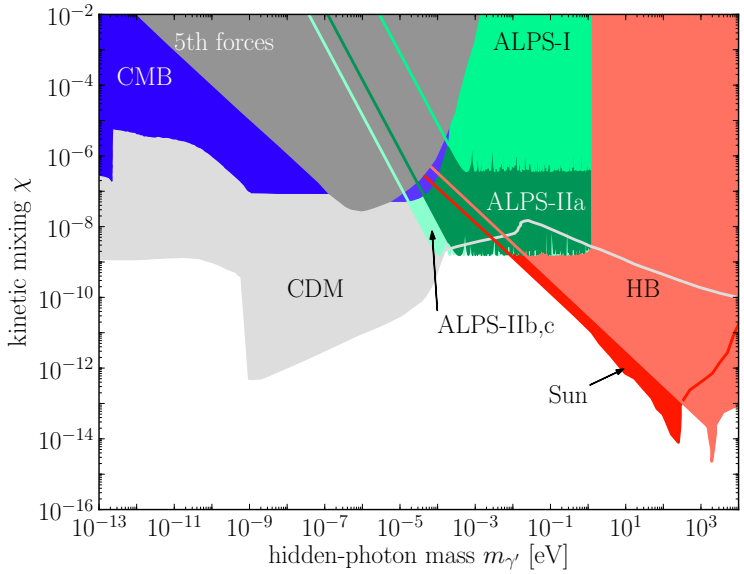

Figure 4.11: Planned sensitivity reach of the different stages of ALPS-II for 95 % CL (dark green and turquoise, this work [160]) for HPs. The sensitivity reach is compared with constraints shown in Fig. 2.4. See caption of Fig. 2.4 and Sec. 2.5 for details of the different observations.

	optics				magnets				detector	
experimental phase	P_{in} [W]	β_{PC} –	$\beta_{\text{RC}}^{\text{IR}}$ –	l [m]	N –	ℓ [m]	Δ [m]	B [T]	η [%]	$\dot{N}_{0.95}$ [s^{-1}]
ALPS-I	5	200	1	[a]8.4, 7.6	1	4.43	–	5.0	95	7.3×10^{-4}
ALPS-IIa	30	5000	40000	10	–	–	–	–	75	2.2×10^{-6}
ALPS-IIb	30	5000	40000	100	–	–	–	–	75	2.2×10^{-6}
ALPS-IIc	30	5000	40000	100	10	8.83	0.936	5.3	75	2.2×10^{-6}

[a]The optical setup in ALPS-I was asymmetric. The length of the production cavity was 8.4 m the length of the vacuum vessel behind the wall was 7.6 m. The length of the magnetic field regions was the same on both sides of the wall.

Table 4.2: Experimental parameters used to calculate the sensitivity of the different stages of ALPS-II. The sensitivity on the ALP and HP parameters depend on the optics (incident power, power build-up in the production and regeneration cavity and cavity length), the magnet setup (number of magnet, length of magnetic field region, size of field free gaps, and field strength), and the detector (quantum efficiency and count-rate upper limit).

power build-ups and laser power determine the χ-value (Eqs. (4.6)). Therefore, ALPS-IIb and IIc cannot reach lower χ values but lower values of $m_{\gamma'}$. Conservation of momentum sets an upper bound on the HP mass (Eq. (2.15)),

$$m_{\gamma'} \leq \omega \approx 1.2\,\mathrm{eV}\ ,$$

for 1064 nm light. At masses $m_{\gamma'} \gtrsim 2 \times 10^{-5}\,\mathrm{eV}$ ALPS-II will improve over the limits from CMB-distortion [61, 62]. In this mass region, ALPS-II will also be able to confirm the CDM constraint [63]. For masses $m_{\gamma'} \gtrsim 4 \times 10^{-2}\,\mathrm{eV}$ the bounds from the Sun and HB-star lifetimes [64–66] are stronger.

The gaps in the sensitivity in Figs. 4.10 and 4.11 are caused by the roots of the oscillatory terms in Eqs. (4.7) and (4.6), respectively. They can be covered by modifying the refractive index of the medium in the cavities. In ALPS-II, the refractive index will be increased by inserting a buffer gas into the vacuum vessels that houses the cavities.

In ALPS-IIc, helium will be used as buffer gas. According to Eq. (4.5), a refractive index of $n-1 = 4 \times 10^{-9}$ can be achieved by injecting helium into the vacuum system until a pressure of 0.015 mbar (measured at room temperature) is reached. Fig. 4.12 compares the sensitivity of ALPS-IIc with and without buffer gas. One can see, how the locations of maximal sensitivity, i.e. the minima of the sensitivity curves, change due to the buffer gas.

The improvements of the sensitivity allow all stages of ALPS-II to cover new parameter space. ALPS-IIc will reach an interesting region of parameter space that is indicated both by anomalous white dwarf cooling and TeV-transparency.

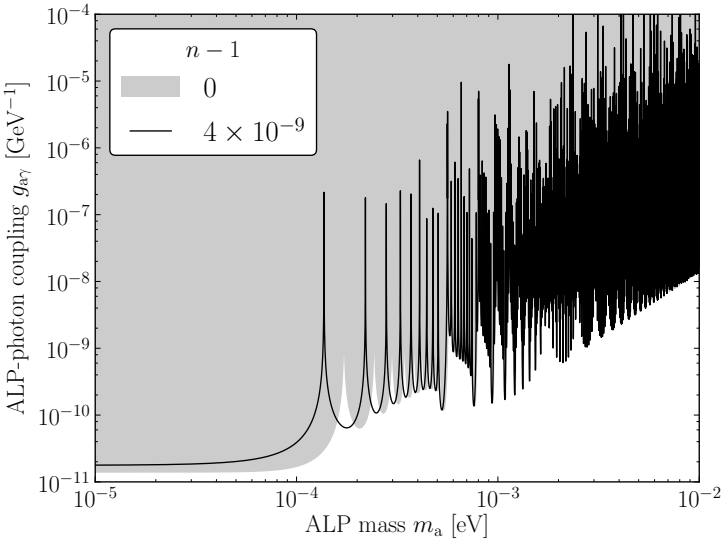

(a) axion-like particles (ALPs)

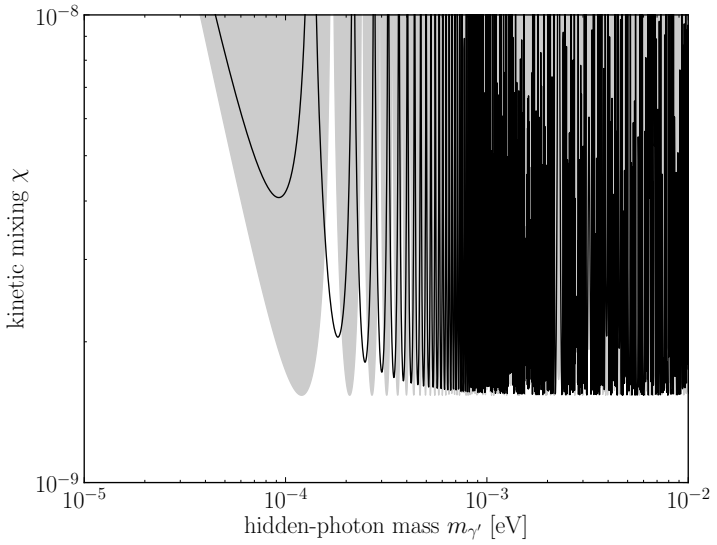

(b) hidden photons (HPs)

Figure 4.12: Influence of the buffer gas on the sensitivity. Compared is the ALPS-IIc 95 % CL sensitivity without a buffer gas (gray area) with the sensitivity with a buffer gas (black line). (a) shows the sensitivity on the ALP parameters. (b) shows the sensitivity on the HP parameters. To reach a refractive index of $n - 1 = 4 \times 10^{-9}$ a helium pressure at room temperature of $p_w = 0.015\,\text{mbar}$ is necessary.

Chapter 5

Low-flux Photon Detection with an Ordinary CCD

Besides the TES detector described above in Sec. 4.6.1, the PIXIS 1024B CCD (PIXIS CCD below) that was used as detector for ALPS-I will be used as detector during the commissioning of ALPS-II and as backup detector. This CCD is a commercially available, back-illuminated, liquid cooled Si-CCD [159]. The liquid cooling allows to reach temperatures of the CCD chip of $-70\,^{\circ}\mathrm{C}$, which results in a dark charge rate estimated in Sec. 5.2.5 to be below $8 \times 10^{-4}\,\mathrm{e}^{-}/(\mathrm{px\,s})$. However, because the regeneration of photons from ALPs is expected to be a very rare process in ALPS-II, a possible signal of these photons will be hidden in the accumulated dark charge and the additional noise of the read-out electronics. Therefore, the only chance to find such a signal is by analyzing a large sample of both data containing only background and data containing also a potential signal. Another obstacle is the reduced quantum efficiency of 1.2 % (Sec. 5.2.3) that results from the fact that the photon energy of the laser used in ALPS-II is near the band gap of silicon.

In this chapter, a short overview of the history of CCD development is given and the working principles of CCD imaging detectors are described in the first section, followed by a presentation of the properties of the PIXIS CCD with a focus on its operation as low-flux single photon detector in ALPS-II, namely the quantum efficiency (Sec. 5.2.3), the fixed-pattern noise (Sec. 5.2.4), the dark count rate and its variation over the chip area (Sec. 5.2.5). The third section contains the proposed algorithm for the statistical analysis, which is based upon the construction of confidence intervals using hybrid resampling. In the concluding discussion, the performance of the PIXIS CCD using the developed analysis algorithm will be compared to the expectations for a TES and an electron multiplying CCD.

5.1 Charge-coupled Devices

5.1.1 History of CCD Development

Initially, charge-coupled devices (CCDs) were conceived as electronic memory devices consisting of series of MIS[1]capacitors, which store packets of charge carriers [173, 174]. By manipulating the voltages of adjacent capacitors it is possible to move these packets along the whole device.

Since photons from the visible spectrum are energetic enough to create electron-hole pairs in silicon, it was quite obvious, that this kind of device was a perfect candidate for an imaging photon detector. Taking an image with such a device consists of two phases: First, the device is exposed to light without modifying the gate voltages of the capacitors. After the exposure is finished, the generated charges are moved to a analog-to-digital converter, that converts the number of electrons to a digital signal. The result is a sequence of digital signal values, which can be further manipulated and visualized using a computer.

An early device was the "Travelling CCD Camera System" developed at NASA's Jet Propulsion Laboratory in 1973. It was installed in various astronomical observatories. Its performance was much better compared to the by-then standard of photographic films. Its sensitivity exceeded that of photographic films by a factor of 100. This led to a huge interest of astronomers in CCD cameras. Since the end of the 1980s, space craft missions were equipped with CCD cameras, e.g. the Wide Field/Planetary Camera aboard the Hubble Space Telescope. Since the end of the last century, the CCD camera technique started to replace photographic films in the consumer market. By now, this technique is widely used both in every day life and scientific research [175]. This was recognized by awarding W.S. Boyle and G.E. Smith, the inventors of the CCD, the 2009 Nobel Prize.

5.1.2 Imaging with a CCD

Fig. 5.1 shows a schematic layout of a CCD imaging device. A matrix of pixels[2] constitute the imaging area. The pixels are arranged in columns separated by *channel stops* that prevent charge diffusion into neighbor columns. After an exposure, the accumulated charges are shifted downwards row-by-row into a line of transport elements (transport register). Its content is then shifted pixel-by-pixel to the read-out electronics, where the charge packet is converted into a voltage signal that is then digitized.

A popular analogy to illustrate how a CCD image is taken is that of a series of buckets mounted on conveyor belts located in an open field combined with a scale: When it is raining, the buckets are filled with water. After some time the conveyor belts are set into motion and the amount of water of each bucket is measured with the scale. This analogy is very fruitful as it shows a number of problems that can occur when such a device is operated:

- The size of the buckets is limited. A maximum value of water (charge carriers) can be collected in each bucket (capacitor). In the context of CCDs this amount is known as *full well capacity*. When this value is

[1]Or metal-oxide-semiconductor (MOS) because the insulating layer is usually made of silicon dioxide.

[2]Short for picture element.

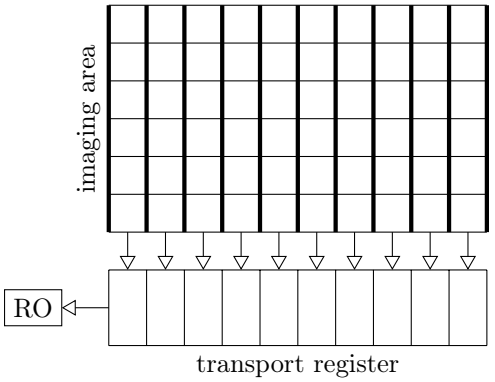

Figure 5.1: Schematic layout of a CCD imaging device. The channel stops of the imaging area are indicated by thicker lines separating the columns. After exposure each line is shifted in the transport register and from there each pixel is shifted to the read-out electronics (RO).

reached, additional water cannot be stored and is lost or spills over to the neighboring buckets (capacitors) known as blooming.

- When the buckets are moved, collected water can spill over into other buckets or be lost. In a CCD, charge carriers can be trapped by defects of the semiconductor while they are shifted from one pixel to another. The average fractional amount of lost and successfully shifted charge carriers are called *charge transfer inefficiency* (CTI) and *charge transfer efficiency* (CTE), respectively.

- The scale measures the amount of water with limited precision. The noise of the read-out structure has the same effect (*read-out noise*). An additional source of uncertainty stems from the discrete nature of the output digital values, which can be important in the case of large gain values of the analog-to-digital converter (ADC) of the read-out structure.

- The size of the buckets may vary and, therefore, the amount of water each bucket collects even if it rains uniformly. Similarly, the thickness of the insulating layer and the density of doping in bulk material vary due to imperfections of the production process. Therefore, the active region of each pixel has a different size.

Unfortunately, this analogy is not perfect and other effects cannot be described in this picture:

- Due to the thermal generation of electron-hole pairs in the active region of each pixel, charge carriers are collected in each pixel even without incident photons. This is known as *dark current* or *dark count rate*. It can be reduced by operating the CCD at lower temperatures.

- Each time before a pixel content is converted into a digital value, the ADC amplifier is biased, i.e. some charges are injected to the read-out capacitor. This is to assure that the charge in the read-out capacitor is always above

the threshold of the ADC and it results in an offset of the digital signal. However, this offset varies from pixel to pixel but remains constant for individual pixels between different exposures. This is called *fixed pattern noise* (FPN), which is misleading as it can be fully corrected by proper subtraction.

- Because the absorption length depends on the photon energy so does the probability for a photon to reach the active region and be absorbed there. Thus, the quantum efficiency depends on the photon energy. For ALPS-II, this effect is important because the infra-red photons have an energy near the band gap of silicon, which results in a decrease of the quantum efficiency of the PIXIS CCD compared to ALPS-I.
- During the transfer of the charge packets during the read-out, additional charges can be generated by impact ionization. These *clock-induced charges* (CIC) add to the FPN and the statistical uncertainty contributes to the observed read-out noise.

A MIS Capacitor

As mentioned above a pixel of a CCD sensor is basically a MIS capacitor. The most simple MIS capacitor is built from doped silicon. On top of this, an insulating layer, typically a few tens of nanometers of SiO_2, is grown, which is covered by a *gate* electrode. The gate typically consists of doped poly-crystalline silicon. This structure is schematically shown in Fig. 5.2a. From right to left, it shows the doped silicon (S), a thin insulating layer (I), and a metallic gate (M). For the sake of simplicity, the following will consider only p-type doped silicon as bulk material.

By putting the silicon bulk to ground and applying a positive voltage to the gate, $V_\mathrm{G} > 0$, the majority carriers of the p-type doped silicon (holes) are repelled from the insulator-semiconductor interface, leaving negatively charged ions. The free charge carrier density is depleted in the doped silicon near the insulator-semiconductor interface (depletion region). Hence, this situation is called *deep depletion*. This situation is shown in Fig. 5.2.

The gate voltage divides into the voltage drops over the insulator, Φ_I, and over the semiconductor, Φ_S,

$$V_\mathrm{G} = \Phi_\mathrm{I} + \Phi_\mathrm{S} \,. \tag{5.1}$$

The width of the depletion region, x_D, is given by [176, Eq. (1.4)]

$$x_\mathrm{D} = \sqrt{\frac{2\varepsilon_\mathrm{Si}\,\Phi_\mathrm{S}}{e\,N_\mathrm{A}}} \,,$$

where ε_Si is the permittivity of silicon, e the elementary charge, and N_A the doping concentration in the p-type silicon. The charge density of the negatively charged ions per unit area of the insulator-semiconductor interface, q_D, is given by

$$q_\mathrm{D} = x_\mathrm{D}\, e\, N_\mathrm{A} \,.$$

As SiO_2 is a dielectric, the voltage drop over the insulator layer is given by

$$\Phi_\mathrm{I} = \frac{x_\mathrm{I}\, q_\mathrm{D}}{\varepsilon_\mathrm{I}} \,,$$

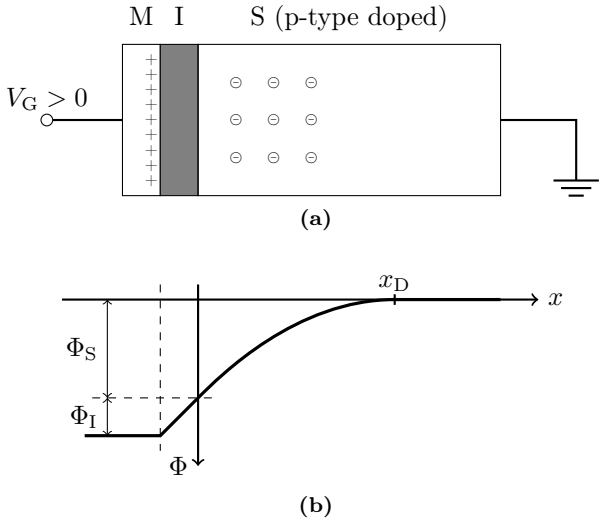

Figure 5.2: A metal-insulator-semiconductor (MIS) capacitor in deep depletion. (a) shows a cross section of a MIS capacitor operated in deep depletion ($V_G > 0$). The majority charge carriers are driven out of the p-type doped semiconductor bulk, leaving behind a depletion region of width x_D containing only negatively charged ions ($\ominus$). (b) shows the electric potential as a function of the distance, x, from the insulator-semiconductor interface. The potential axis is pointing downwards to indicate the direction in which free electrons move. The gate voltage, V_G, divides into voltage drops over the insulator, Φ_I, and semiconductor, Φ_S.

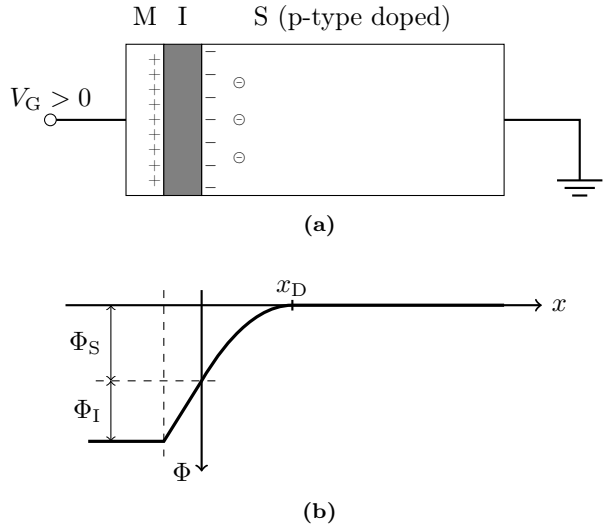

Figure 5.3: A MIS capacitor in weak inversion. (a) shows a cross section of a MIS capacitor operated in weak inversion ($V_G > 0$ with additional free charges). Free electrons ($-$) replace a part of the negatively charged ions ($\ominus$) reducing the size of the depletion zone compared to the deep depletion state Fig. 5.2. (b) shows the electric potential with the potential axis pointing downwards. See Fig. 5.2 for more information.

where x_I and ε_I are the width and the permittivity of the insulator layer, respectively. Hence, Eq. (5.1) can be written as

$$V_G = \frac{x_I}{\varepsilon_I}\sqrt{\frac{2\varepsilon_{Si}\Phi_S}{eN_A}} + \Phi_S \; .$$

If electron-hole pairs are produced in the depletion region of the silicon bulk, e.g. by thermal generation or the inner photoelectric effect, the negatively charged electrons are attracted by the gate voltage while the holes are repelled by it. Hence, the charges are separated. As the electrons are highly mobile minority charge carriers in the p-type silicon bulk, they can move freely to the insulator-semiconductor interface. The shape of the potential forms a *potential well* for the free electrons as shown in Fig. 5.2b. With q_n as their density per unit area, the gate voltage is given by

$$V_G = \Phi_I + \Phi_S = \frac{x_I}{\varepsilon_I} q_n + \frac{x_I}{\varepsilon_I}\sqrt{\frac{2\varepsilon_{Si}\,\Phi_S}{e\,N_A}} + \Phi_S \; .$$

Since V_G is kept constant, the potential difference over the semiconductor bulk is smaller compared to the deep-depletion state. Accordingly, the same holds for the width of depletion zone, x_D, and the density of charged ions, q_D.

This state is called *weak inversion* and it is the operational state of MIS capacitors used in CCD imaging. Because the electrons are stored at the surface of the semiconductor, this type of devices is called surface channel CCD (SCCD).

As more and more electron-hole pairs are generated, the size of the depletion regions shrinks until all charges stored by the capacitor are free charge

carriers. The gate voltage is screened by the free charge carriers at the insulator-semiconductor interface. The rate of production of electron-hole pairs equals the recombination rate. Hence, at this point the capacitor is in equilibrium. The initial potential well is full. The total charge stored in this state defines the *full-well capacity*, which depends on the thickness of the insulator and the applied gate voltage.

Photon Sensing

Incident photons can excite valence electrons via the inner photoelectric effect to the conduction band, producing "free" electrons and positively charged holes, which diffuse into the lattice structure and, if not hindered by additional measures, recombine after a lifetime of $\mathcal{O}(100\,\mu s)$ [175, p. 7].

The band gap between valence and conduction band is $E_g = 1.14\,eV$ for silicon at $-70\,°C$ [177]. Photons with energies below this value are not energetic enough to excite electron-hole (e-h) pairs and cannot be detected with a silicon-based device. Whereas higher energetic photons can excite e-h pairs. The yield of e-h pairs per incident photon depends on the energy of the photon. Photons with energies $E_g \leq E_\gamma \leq 5\,eV$, i.e. from the near infra-red to the extreme ultra-violett spectrum generate one e-h pair. For higher energetic photons, the number of e-h pairs increases, e.g. at 10 eV three e-h pairs are generated on average and in the soft X-ray spectrum (0.1 to 10 keV) several hundred e-h pairs [175, p. 7].

Because the thickness of the bulk material in early CCDs was high, the gate-side of these devices was illuminated (front-side illumination). For detection in a front-side illuminated CCD, photons have to pass the gate and insulator material to reach the depletion region. Because of the small absorption length of ultra-violett (UV) photons ($\lesssim 10\,nm$), most UV photons are absorbed outside of the depletion region. Hence, only a low quantum efficiency can be reached with front-side illuminated CCDs. This problem was solved by reducing the total thickness of the devices to $\sim 10\,\mu m$, so that they can be back-side illuminated. The distance photons have to travel through the bulk material to reach the depletion region is decreased. Hence, more photons reach the depletion region and back-side illuminated CCDs have much higher quantum efficiencies in the UV. The thinning is achieved by etching the back-side of the bulk material (back-thinning).

Charge Transport

As already mentioned, a CCD sensor consists of an array of pixels connected to a digitizing read-out structure. The array is organized in separated columns of closely connected pixels. The columns are separated by channel stops. On a p-type bulk, typically highly doped p^+-type regions are used that form potential barriers between the columns. Each pixel consists of a number of capacitors, typically three. During exposure, the voltages of the gates are kept constant with a positive voltage on the central gate and e.g. zero voltage on the two outside gates. This builds up a potential barrier between neighboring pixels to prevent diffusion of charges into the neighbor pixels. A sketch of this is shown in Fig. 5.4.

During read-out, the accumulated charges of each pixel must be transferred

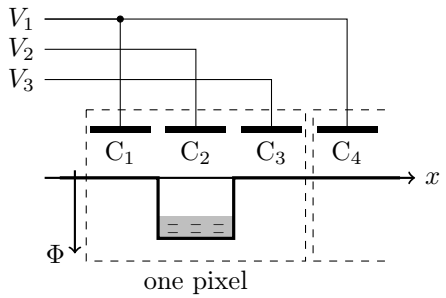

Figure 5.4: A series of four MIS capacitors (C_i) as part of a column of a CCD array. Three capacitors form one pixel (C_1 to C_3). C_4 is part of the next pixel. The gate voltages, V_k, are kept constant during exposure. Every third gate is connected to the same voltage. Potential wells are formed under the central gates (C_2) by applying a positive gate voltage, $V_2 > 0$. Potential barriers between the pixels are created by applying zero voltage on the outside gates of each pixel (C_1, C_3 and C_4). The potential of each gate is sketched in the lower part. Accumulated charges are illustrated by the gray shaded area in the potential well.

to the read-out structure. This is achieved by adjusting the gate voltages. Fig. 5.5 illustrates this process.

At t_1 only the central capacitor, C_2, is biased and contains free electrons. Then, the gate voltage of the next capacitor, C_3, is increased to the same level as C_2. This removes the potential barrier between these two capacitors and the free electrons can distribute over the now larger potential well (t_2 in Fig. 5.5). This is driven by thermal diffusion due to the inhomogeneous charge distribution and drift induced by the potential difference due to the inhomogeneous charge distribution.

The depth of the potential well of C_2 is then decreased by lowering the gate voltage, V_2. During this process (t_3) the fringing fields between C_2 and C_3 push the free electrons into the potential well of C_3. By this operation the charges initially located in C_2 moved to C_3. Performing the same procedure on the next capacitors, C_3 and C_4 moves the charges even further. Hence, repeating this operation with the appropriate pixels allows to transport the charges over a line of pixels.

If the read-out speed is sufficiently high, the electric field between the capacitors can become so high that the accelerated charges of the shifted charge packets can generate additional electron-hole pairs via impact ionization. These clock-induced charges (CIC) (or spurious charges) contribute to the observed FPN with a non-vanishing noise because the generation of CIC is a stochastic process.

Buried Channel CCD

In SCCDs, as indicated in Fig. 5.3a, the free electrons are stored directly at the insulator-semiconductor interface. However, at the interface between the mono-crystalline semiconductor bulk (p-type Si) and the typically amorphous insulator (SiO_2) a high density of lattice defects exist in the bulk, in which free

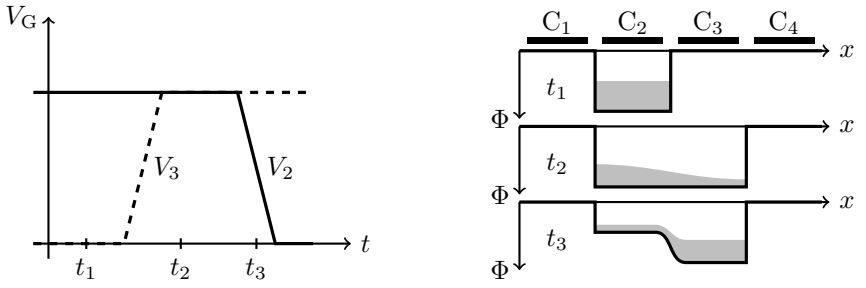

(a) Gate voltages **(b)** Potential wells

Figure 5.5: Charge transport between MIS capacitors of a CCD column. (a) shows the time-dependence of the gate voltages of the central (C_2) and neighboring (C_3) capacitors. (b) shows the potential wells at three different times. The distribution of the free electrons is indicated by the shaded areas.

electrons can be trapped. The lifetime of these trapped states is much larger than the time that is available to conveniently read out a CCD. As a result, an efficiency of the transport process (charge transfer efficiency, CTE) of 98 % was reached with SCCDs [175, p. 9], much to low for scientific imaging, especially if a large number of pixels is needed.

A solution for this is to "bury" the p-type doped silicon under a thin layer of n-type doped silicon, followed by the insulating layer and the gate electrode (Fig. 5.6a). By choosing the right dopant concentration for the n-type layer according to its depth and the dopant concentration of the p-type layer, it can be achieved that it is fully depleted after interacting with the p-type layer.

When biased, the space charge of the n-type layer changes the shape of the potential compared to the SCCD (Figs. 5.6b and 5.2b, respectively). The maximum of the potential is now located inside the n-type bulk and the free electrons cannot interact with the lattice defects at the insulator-semiconductor interface. With such a layout CTEs of 99.999 % and above can be reached (e.g. [178]).

Read-out

The final step of taking an image with a CCD sensor is to read-out the accumulated charges. This is typically achieved by converting it into a voltage signal that can be digitized. A common structure for this is a *floating diffusion* output structure as shown in Fig. 5.7 [176, Sec. 2.4.1]. At the end of the transport register lies an output gate (OG) followed by an n^+-type region, which is typically formed by implanting and diffusing appropriate dopant atoms. This is connected to the gate of an on-chip amplifier, e.g. a source follower built from a metal-oxide-semiconductor field effect transistor (MOSFET). Additionally, this region is connected to a positive supply voltage (drain voltage), V_{RD}, by a second transistor (reset transistor). The gate of the reset transistor is controlled by the reset voltage, V_R. The output gate is present to shield the n^+-region from the pulsed gates of the transport register. It is biased by a constant, positive voltage below the maximal bias voltage of the transport gates, $0 < V_{OG} < V_{i,max}$.

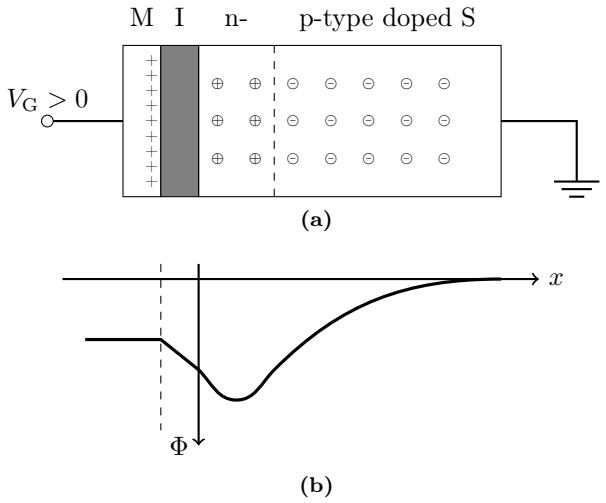

Figure 5.6: A biased buried channel MIS capacitor. (a) shows the cross section. Between the insulator and the p-type doped semiconductor is a completely depleted, thin n-type doped layer. The maximum of the potential shown in (b) moved away from the insulator-semiconductor interface compared to Fig. 5.2. Note that the potential axis is pointing downwards to stress the existence of the potential well. See Fig. 5.2 for more information.

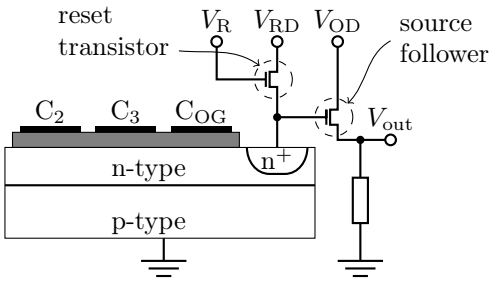

Figure 5.7: Schematic view of the read-out structure of a buried channel CCD using a floating diffusion. The on-chip source follower and reset structure are also shown. See text for description.

Initially, the floating diffusion is reset by setting $V_{\mathrm{R}} > 0$ which opens the reset transistor. The n^+-region is then biased by the constant drain voltage, $V_{\mathrm{RD}} > 0$. This builds up a depletion layer at the pn-junction between the p-type bulk and the n^+-region. The reset transistor is closed again, separating the n^+-region from the drain voltage, V_{RD}.

The charges are then shifted to the n^+-region as described above. The potential barrier between C_3 and C_{OG} is lower than that between the last transport gates C_2 and C_3 because $V_{\mathrm{OG}} > 0$. Hence, the charges can pass this barrier when V_3 is lowered during charge transport and reach the n^+-region. The additional charges in the n^+-region result in a change

$$\Delta V_{\mathrm{out}} = A\frac{Q}{C} \tag{5.2}$$

of the output voltage of the source follower, where $A \approx 1$ is the amplification of the source follower, Q is the stored charge and

$$C = C_{\mathrm{r}} + C_{\mathrm{pn}}$$

is the capacitance given by the parasitic capacitance of the reset transistor, C_{r}, and the capacitance of the pn-junction, C_{pn}. Via the source follower this voltage drop is fed to an analog-to-digital converter where the voltage is converted into a digital signal. This ADC is typically located outside of the CCD chip and is not shown in Fig. 5.7.

From Eq. (5.2) one can see that a high change in voltage is achieved when the total capacitance is small. Devices with $C \sim 10\,\mathrm{fF}$ have been built [176, Sec. 2.4.1], corresponding to a conversion factor of $\sim 16\,\mu\mathrm{V/electron}$.

This output structure introduces several types of noise [176, Sec. 3.4]. The potential of the n^+-region is different after each reset due to thermal variation of the channel resistance of the reset MOSFET. Additionally, the reset voltage V_{RD} may vary during the read out of a full CCD frame due to imperfections of the circuitry. Both affect the baseline for the voltage difference of Eq. (5.2), which can differ for each read-out charge packet. Second, the output voltage of the source follower exhibits white thermal noise and $1/f$ flicker noise.

The digitization in the ADC is also a source of thermal electronic noise. The fact that the voltage range is split into discrete intervals and input voltages are converted to a digital value that represents the nearest interval edge introduces digitization noise as a new type of noise, which, however, is negligible for ADC gains of the order of the above mentioned noise contributions. The ADC can also introduce systematic offset variations. Together with the systematic offset variations caused by the reset voltage this makes up the fixed pattern noise, which can be corrected for.

In Sec. 5.2 below, the properties of the PIXIS CCD will be characterized. This includes the quantum efficiency near 1064 nm, the FPN, CIC and the associated combined read-out noise and the dark charge rate. The noise in each pixel value is caused by the read-out process (RO), accumulated signal (S) and dark charges (DC) and CIC, and may be symbolically written as

$$\mathit{Noise} = RO + S + DC + CIC\ ,$$

where *RO* and *CIC* are independent from the exposure time. In the following, σ_{RO} will be used to denote exposure-time-independent noise component, i.e. the combination of *RO* and *CIC*. This read-out noise increases with the rate at which the CCD is read out.

Electron Multiplying CCD

In the case of a low signal and dark count rate, the read-out noise dominates the total uncertainty of the digitized signal. Electron multiplying charge-coupled devices (EMCCD) [179] diminish the effect of the read-out noise by amplifying the charge packets stored in the pixels before they are passed to the read-out structure. This allows to reach sub-electron read-out noise, e.g. [180, 181]. The amplification is achieved by a gain register that is installed between the transport register and the read-out structure. In each stage of the gain register the current is amplified by impact ionization. The mean gain, G, typically $\sim$1000, is given by [180]

$$G = g^N \,,$$

where N is the number of stages and the gain of each stage is small, typically $g = 1.02$. As the process of impact ionization is stochastic, this amplification introduces another source of noise. The total effective noise, σ_{eff}, is given by

$$\sigma_{\mathrm{eff}} = \sqrt{F^2\, S + \frac{\sigma_{\mathrm{RO}}^2}{G}} \,,$$

where

$$F = 2(G-1)G^{-(N+1)/N} + \frac{1}{G}$$

is the excess noise factor caused by the stochastic properties of the amplification process, S the number of electrons before the amplification process and σ_{RO} the combined random noise components discussed in the previous section. For high gains and a large number of amplification elements ($G, N \gg 1$), F is approximately 2, reducing the effective quantum efficiency of the camera to one half of the value without amplification.

In the case of very low signal rates, Daigle et al. [182] propose to interpret the pixel values as binary, i.e. setting a threshold at e.g. $5\sigma_{\mathrm{RO}}$ and discriminating only whether a photon was detected (signal above) or not (signal below the threshold). By this, the original quantum efficiency can be restored. Downsides of this mode of operation are that some part of the signal is lost below the cut and at higher signal rates in coincidences and that the read-out speed of the pixels has to be sufficiently low to reduce the impact of clock induced charge [182]. The expected performance of such a device in ALPS-II is explored in Sec. 5.3.3.

5.2 Properties of the PIXIS

The PIXIS camera is based on an e2v CCD47-10 sensor chip [178]. The control electronics allow for two read-out speeds of 100 kHz and 2 MHz with three different ADC gains of roughly 1, 2, and 4 e^-/ADU. Low dark count rates of approximately $8 \times 10^{-4}\,\mathrm{e}^-/(\mathrm{px\,s})$ are reached by thermo-electric cooling of the chip to temperatures of $-70\,^{\circ}\mathrm{C}$. The camera operations are controlled by a PC via a USB connection.

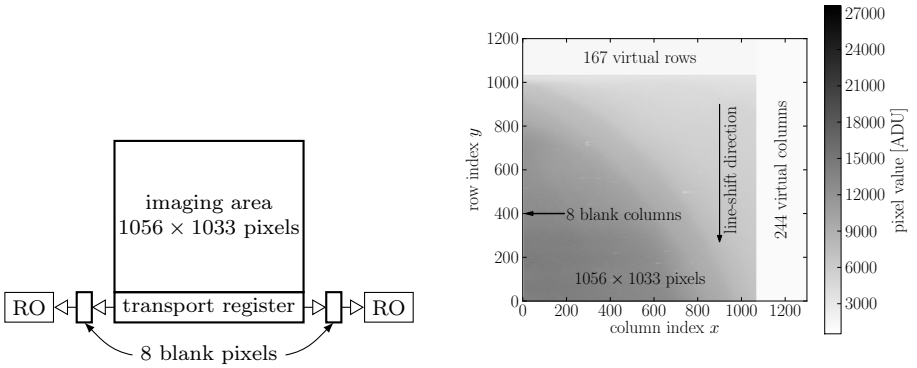

(a) Device Schematics **(b)** Real CCD frame

Figure 5.8: Layout of the e2v CCD47-10 chip used in the PIXIS camera. (a) shows the schematic layout. (b) shows a picture where no pixels were discarded and a total of 1300×1200 pixels were read. The orientation of the frame is the same as in (a), i.e. the transport register is at the bottom. The different regions are annotated and the direction of line-shift is indicated. The transport register is read-out to the left.

In this section, the sensor chip and its operation will be presented together with a description of the background stability and a determination of the quantum efficiency at 1064 nm.

5.2.1 The e2v CCD47-10 Sensor Chip

The e2v CCD47-10 consists of 1056×1033 back-illuminated pixels [178][3]. The pixel size is $13 \times 13\,\mu m^2$ and 1024×1024 pixels are intended to be used for imaging. Hence, the imaging area has a size of $13.3 \times 13.3\,mm^2$. A schematic view of the chip is depicted in Fig. 5.8a. The transport register is at the bottom of the chip. Both sides are terminated by eight additional blank pixels and read-out structures at both sides. The on-chip read-out has a conversion factor of typically 4.5 µV/electron.

5.2.2 PIXIS 1024B

The PIXIS 1024B allows to thermo-electrically cool the CCD47-10 chip to temperatures of −70 °C and below to reduce the dark count rate. The camera is connected to a heat exchanger by a liquid coolant line. The CCD chip is installed in an evacuated housing. The entrance window has a width of 3.17 mm. A mechanical shutter is mounted to the CCD housing.

The camera electronics are controlled by a PC via a USB connection. The electronics are elaborate and allow to bin the pixels into *logical pixels* before read

[3] Note that the data sheet lists 1056×1027. However, this is in contradiction to the listing on the webpage [183] and illuminated frames (e.g. Fig. 5.8b), which both indicate 1056×1033 pixels.

Property	RO-speed	value
dark count rate (at −70 °C)	–	$8 \times 10^{-4}\,\mathrm{e}^-/(\mathrm{px\,s})$
single pixel full well	–	120 ke$^-$
output node full well	–	260 ke$^-$
read-out noise rms	100 kHz	3.85 e$^-$
	2 MHz	13.73 e$^-$
low gain	100 kHz	4.05 e$^-$/ADU
	2 MHz	4.43 e$^-$/ADU
medium gain	100 kHz	2.07 e$^-$/ADU
	2 MHz	2.19 e$^-$/ADU
high gain	100 kHz	1.02 e$^-$/ADU
	2 MHz	1.14 e$^-$/ADU

Table 5.1: Properties of the PIXIS camera as specified by the vendor in a "Certificate of Performance" [184]. Note that the values for the dark count rate and read-out noise listed here differ from the measured values.

out to reduce the impact of the read-out noise for cases when it is not necessary to resolve features of the signal on the scale of a single pixel. By default, the electronics discard the first 24 pixels of each line, i.e. the eight blank pixels and the pixels of the first 16 columns. The electronics can be programmed not to discard these pixels and to read out more pixels than physically exist on the chip (virtual pixels). Fig. 5.8b shows a frame of 1300 × 1200 px taken without discarding any pixels. The eight blank columns are followed by the 1056 columns of the imaging area and additional 244 virtual columns. The 1033 rows of the imaging area are accompanied by 167 virtual rows. This overscanning can be used to correct variations of the offset. As mentioned above, the electronics has two different read-out speeds, 100 kHz and 2 MHz, with three different ADC gains each. The ADC has a resolution of 16 bit.

During the characterization of the camera, very long exposures were taken. It was found, that the maximal possible exposure time is between 139 and 139.5 min. This is assumed to be a limitation of the electronics.

The vendor delivered a "Certificate of Performance" [184] with measurements of the gain, read-out noise, dark count rate and pixel capacity (cf. Tab. 5.1).

5.2.3 Quantum Efficiency

For the optical spectrum, the quantum efficiency, η, of a CCD is defined as the ratio of the number of electrons, N_e, produced over the number of photons, N_γ, of a given wavelength that hit the camera,

$$\eta = \frac{N_\mathrm{e}}{N_\gamma} \,.$$

The data sheet of the PIXIS [159] shows the typical quantum efficiency at room temperature (25 °C) for wavelengths of 250 to 1050 nm (cf. Fig. 5.15). During the commissioning of ALPS-II the camera will be operated at temperatures of −70 °C to achieve a reduced dark count rate. It will be used to detect infrared light with a wavelength of 1064 nm. Thus, the quantum efficiency of the

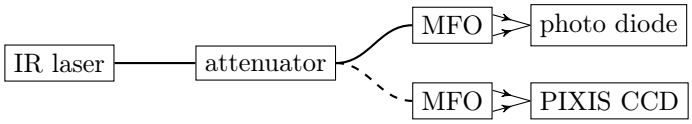

Figure 5.9: Schematic view of the setup used to measure the quantum efficiency of the PIXIS CCD. The infra-red laser is connected to an micro focus optic (MFO) via an attenuator. The unattenuated laser is calibrated with a PIN photo diode. After the calibration, the laser is attenuated and focused on the chip of the PIXIS CCD to take CCD frames. Not shown are the ND filters.

cooled CCD at 1064 nm has to be measured. In addition to the probability for the production of an electron-hole pair in the depletion region of a pixel of the CCD, the value measured here includes other effects as reflection on the vacuum window of the CCD housing.

To measure the quantum efficiency, a calibrated light source is constructed. This is used to illuminate the CCD chip. The quantum efficiency is estimated from the resulting CCD images. Fig. 5.9 shows a sketch of the setup.

Calibrated Light Source

The calibrated light source is constructed from an infra-red, continuous wave diode laser[4] with a vendor specified wavelength of $\lambda = 1066.7\,\mathrm{nm}$. It has an output power tunable between 267 nW and 1 mW. However, a precise selection of the output power is not possible. Therefore, the laser is connected to an attenuator[5] with an optical fiber. The attenuator consists of two collimators. The first collimator widens the light from the input fiber to a collimated beam with a large diameter ($\mathcal{O}(2\,\mathrm{cm})$). The second collimator collects the widened beam and couples it into the output fiber. Between the collimators is a steel sphere, which is mounted on a micro meter screw. The sphere blocks a part of the light. Thus, only the remaining fraction can be coupled into the output fiber. The output of the attenuator was connected to another collimator[6] by an optical fiber. A MFO[7] with a numeric aperture of 0.22 was mounted to this collimator. The distance of the focus from the housing is 25.2 mm. The collimator with the MFO is mounted on a three-axis micro-positioning table[8]. Additionally, the power is further attenuated by neutral density (ND) filters, which were attached to the MFO.

This setup (cf. Fig. 5.9) is calibrated using a PIN photo diode[9] with a vendor tabulated photo sensitivity. Its active area has a diameter of 1 mm. The photo sensitivity near 1066.7 nm is shown in Fig. 5.10.

The photo diode was installed in a transimpedance amplifier as shown in Fig. 5.11. An LF356 amplifier and a resistor with $R = 10\,\mathrm{M\Omega}$ were used. The measured output voltage, U_{out}, is given by

$$U_{\mathrm{out}} = U_{\mathrm{ph}} + U_{\mathrm{dark}} = R\,(I_{\mathrm{ph}} + I_{\mathrm{dark}}) \ ,$$

[4] Schäfter+Kirchhoff 51nanoFCM-1064-1-xxx-P-5-2-18-0-150
[5] Schäfter+Kirchhoff 48AT-0-FC-4-A11-03+SMS-4-A11-03
[6] Schäfter+Kirchhoff 60FC-T-4-M40-54
[7] Schäfter+Kirchhoff 13M-M30-37-S
[8] Thorlabs DT12
[9] Hamamatsu G8370-0476(X)

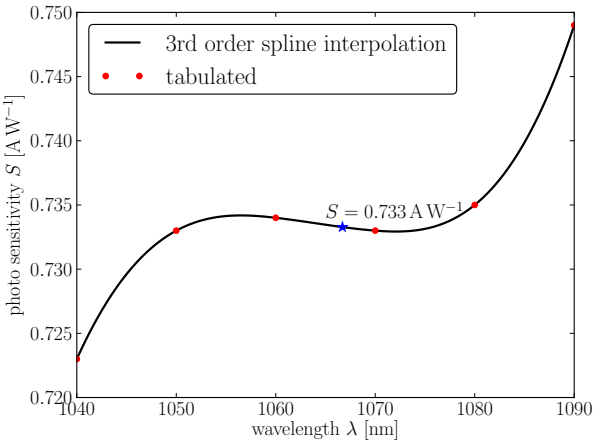

Figure 5.10: Photo sensitivity of the Hamamatsu G8370-0476(X) PIN photo diode near the wavelength of the infra-red laser (1066.7 nm). Shown are the tabulated values (red dots), a cubic spline interpolation of the tabulated data (solid line) and the value of the spline interpolation at the wavelength of the infra-red laser (blue asterisk).

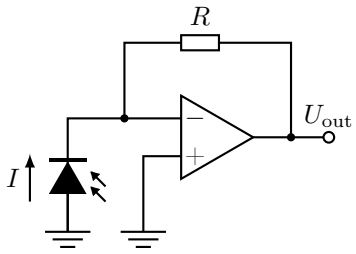

Figure 5.11: Transimpedance amplifier used with the PIN photo diode to calibrate the laser.

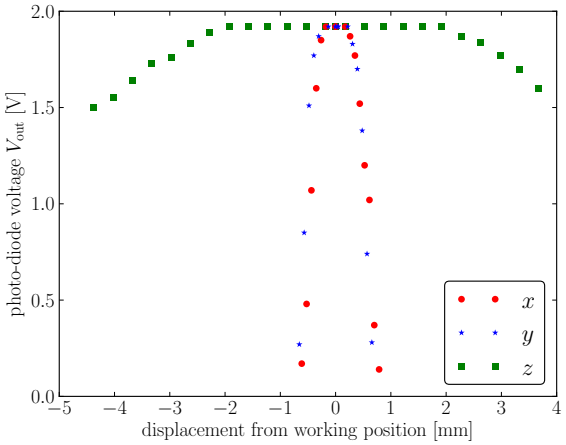

Figure 5.12: Position dependence of the photo-diode output voltage. The position of the micro focus optic was varied in the beam direction (z) and perpendicular to it (x and y).

where I_{ph} is the electric current generated in the photo diode by incident photons and I_{dark} is the thermal dark current. Correspondingly, U_{ph} and U_{dark} denote the parts of the output voltage due to the photo-generated and dark currents. Hence, the power of incident photons is given by

$$P_{\mathrm{ph}} = \frac{I_{\mathrm{ph}}}{S} = \frac{U_{\mathrm{out}} - U_{\mathrm{dark}}}{R\,S} \,, \tag{5.3}$$

where S is the photo sensitivity of the photo diode. U_{dark} is measured in a dedicated measurement without incident light. The voltages are measured using a multi meter[10]. Each voltage is measured several times to estimate the statistical uncertainty. The systemic uncertainties are taken from the data sheet [185].

After assembling all components, the in- and output collimators of the attenuator are aligned. The photo diode is positioned in the focal point of the MFO. The working position is verified by testing that the output of the photo-diode circuit does not depend strongly on variations of the MFO position in all directions (cf. Fig. 5.12). After that, the dependence of the attenuator transmission, T, on the position, p, of the steel sphere is measured. For a reference position, p_0, the transmission is given by

$$T(p) = \frac{U_{\mathrm{ph}}(p)}{U_{\mathrm{ph}}(p_0)} = \frac{U_{\mathrm{out}}(p) - U_{\mathrm{dark}}}{U_{\mathrm{out}}(p_0) - U_{\mathrm{dark}}} \,. \tag{5.4}$$

Fig. 5.13 shows an exemplary transmission curve. The minimal value on the micro-meter screw scale, $p_0 = 3.5\,\mathrm{mm}$, has been chosen as reference position.

Next, the transmission of the ND filters are measured (Tab. 5.2).

CCD Exposure

For the CCD exposures, the laser is set to minimal output power and the output voltage of the photo-diode circuit is recorded. The MFO is placed in front of

[10] Amprobe AM-18

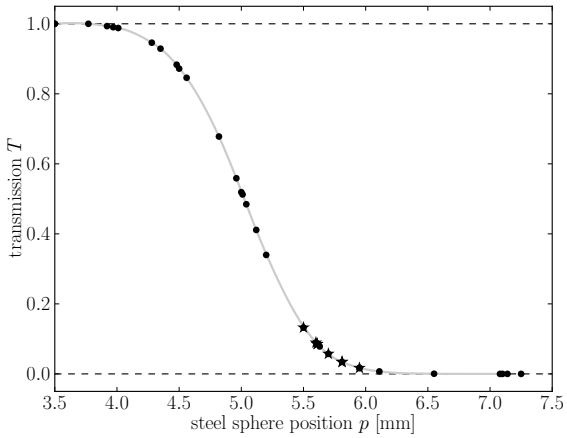

Figure 5.13: Exemplary transmission curve of the attenuator. Shown are measured transmissions (black dots and asterisks) as well as an interpolating curve of these measurements (gray line). The measurements marked by asterisks were used for calibration.

Filter	Transmission	
	nominal[a]	measured
NE10A	0.07	$0.10123 \pm 0.00007(\text{stat}) \pm 0.00089(\text{syst})$
NE20A	0.05	$0.05812 \pm 0.00008(\text{stat}) \pm 0.00063(\text{syst})$

[a] Taken from ref. [186].

Table 5.2: Transmission of ND filters at $\lambda = 1066.7\,\text{nm}$.

the CCD. The output power is attenuated with the steel sphere attenuator and optionally with ND filters. The CCD chip is exposed to the laser light for different exposure times. The intensity of even the attenuated laser is so high that a large full width half maximum (FWHM) of the laser spot on the CCD of $\sim 120\,\mathrm{px}$ is necessary in order to achieve exposure times above 1 s. Exposure times of this length are necessary because below this value the time necessary to open and close the shutter cannot be neglected.

Each exposure is repeated three times. An offset correction is done by subtracting the average pixel value of the first ten rows,[11]

$$v_{\mathrm{cor},f}(x,y) = v_f(x,y) - \frac{1}{N_{\mathrm{px}}} \sum_{\substack{x' \\ y'<10}} v_f(x',y') \;, \tag{5.5}$$

where $v_f(x,y)$ is the read-out value of a pixel in column x and row y of frame f and $N_{\mathrm{px}}$is the number of pixels included in the sum. The FPN and accumulated dark counts are estimated from dedicated background frames, which are taken with closed shutter. For each exposure time, three background frames are taken. These are corrected according to Eq. (5.5), stacked and averaged. A pixel value, $b_t(x,y)$, of these averaged background frames is given by

$$b_t(x,y) = \frac{1}{3} \sum_{f\in\mathcal{B}(t)} v_{\mathrm{cor},f}(x,y) \;,$$

where $\mathcal{B}(t)$ is the set of the three background frames taken with exposure time t. Finally, the average background frame is subtracted from the averaged signal (shutter open) frame, giving

$$c_f(x,y) = v_{\mathrm{cor},f}(x,y) - b_t(x,y) \;.$$

Fig. 5.14a shows such a corrected frame. The profiles in Fig. 5.14b show that the spot is completely contained within the CCD area and that the background is properly subtracted by the used method as the corrected values are zero at the borders of the imaging area. The profiles in the upper panel pierce the maximum value pixel, $(x_{\mathrm{m}}, y_{\mathrm{m}})$, i.e. they show $c_f(x, y_{\mathrm{m}})$ (solid red line) and $c_f(x_{\mathrm{m}}, y)$ (dashed blue line). The profiles in the middle panel show the same but pierce $(x_{\mathrm{m}}+\mathrm{FWHM}/2, y_{\mathrm{m}}-\mathrm{FWHM}/2)$. The lower panel shows the averaged profiles given by

$$\langle c_f\rangle_x(y) = \frac{1}{N_{\mathrm{col}}} \sum_{x=0}^{N_{\mathrm{col}}-1} c_f(x,y) \qquad \text{(dashed blue)}$$

$$\langle c_f\rangle_y(x) = \frac{1}{N_{\mathrm{row}}} \sum_{y=0}^{N_{\mathrm{row}}-1} c_f(x,y) \qquad \text{(solid red)} \;,$$

where N_{row} and N_{col} are the number of rows and columns, respectively.

The electron rate is given by

$$\dot{N}_{\mathrm{e}} = \frac{1}{G\, t_{\mathrm{exp}}} \sum_{x,y} c_f(x,y) \;,$$

[11] This offset correction is sufficient here (cf. Fig. 5.14). Hence, the more complicated offset correction involving the overscan feature of the PIXIS electronics that is used below was not necessary.

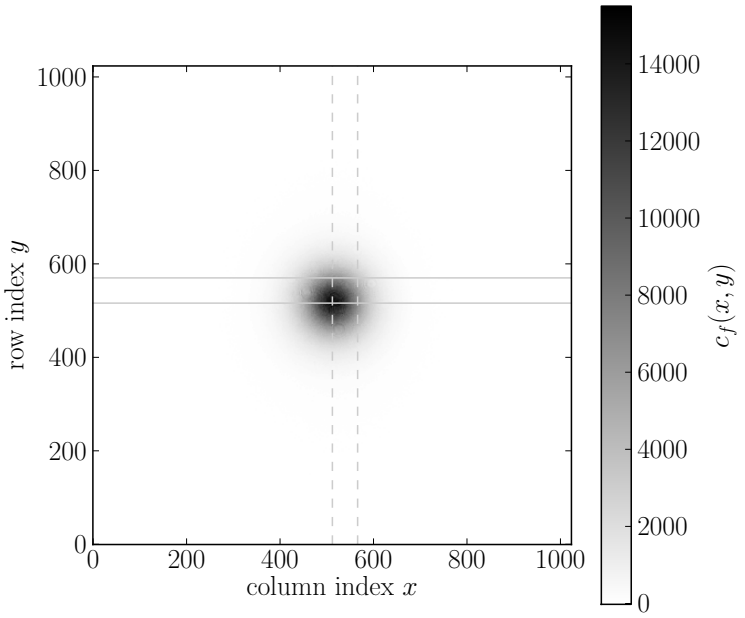

(a) Corrected frame

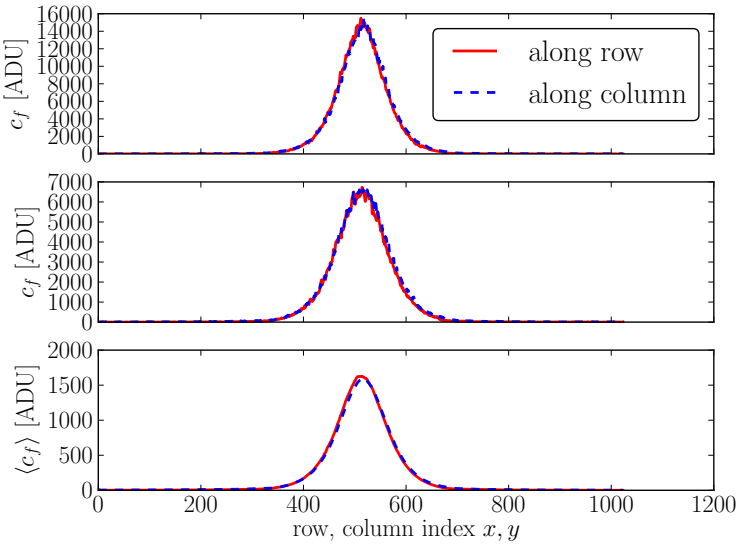

(b) Values along rows/columns

Figure 5.14: Corrected CCD frames for quantum efficiency estimation. The signal frame was taken with $t_{\text{exp}} = 1\,\text{s}$, $p = 5.50\,\text{mm}$ and the NE10A ND filter. (a) shows a gray-scale plot of a corrected CCD frame used for quantum efficiency estimation. (b) shows the pixel values along rows (solid, $y = \text{const}$) and columns (dashed, $x = \text{const}$). The upper panel shows the profile for the row and column piercing the maximal value. The middle panel shows the profile for a row and column offset from the maximum by FWHM/2. The location of the rows and columns is indicated by the lines in (a). The lower panel shows the average values per row/column. See text for more information.

where the sum is taken over the whole frame, G is the gain of the CCD's ADC and t_{exp} the duration of the exposure. The vendor specified value for the gain (Tab. 5.1, [184]) is used.

Calculating the Quantum Efficiency

The quantum efficiency is given by

$$\eta = \frac{\dot{N}_{\mathrm{e}}}{T\, P_\gamma / E_\gamma} \,, \tag{5.6}$$

where T is the combined transmission of the attenuator and optional ND filters, P_γ the unattenuated laser power measured by the photo diode and E_γ the photon energy.

The statistical and systematic uncertainties of all measured quantities and their correlations (cf. App. A.4) were taken into account. The uncertainties of the voltage measurement influence the transmission, T, and the photo-power, P_γ. The systematic uncertainty of the resistance, R, (5 %) influences only P_γ. Hence, the largest contribution to the systematic uncertainty comes from voltage measurements. A possible drift in the laser power was checked for and found to be negligible. The statistical uncertainties of the electron rate is estimated from the three different exposures that were taken for each exposure time and attenuation. Tab. 5.3 lists the single measurements and the combined result. Compared to the systematic uncertainty, the statistical uncertainty is negligible. In Fig. 5.15 the combined result is compared with the typical quantum efficiency as listed in the datasheet [159]. In this comparison, one has to keep in mind that, for wavelengths $\lambda \gtrsim 900\,\mathrm{nm}$, the quantum efficiency of silicon-based CCDs deceases when the temperature is decreased [187]. At $\lambda = 1066.7\,\mathrm{nm}$, the quantum efficiency at $-70\,^{\circ}\mathrm{C}$ is expected to be a factor of $\gtrsim 3$ below the value at $25\,^{\circ}\mathrm{C}$ [188].

The quantum efficiency was measured for a wavelength of 1066.7 nm, slightly above the value of the laser in ALPS-II (1064 nm). Extrapolating the curve in Fig. 5.15 to 1066.7 nm shows that the value expected for 1064 nm is higher,

$$\eta(1064\,\mathrm{nm}) > \eta(1066.7\,\mathrm{nm}) \,.$$

Hence, using the obtained numerical value

$$\eta = 1.208 \pm 0.002(\mathrm{stat}) \pm 0.079(\mathrm{syst})$$

for 1064 nm as well is a lower limit. This conservative approach is used here.

Since it is possible – though with a low efficiency – to detect infra-red photons with the PIXIS CCD, it can be used during commissioning and as backup detector for ALPS-II. For this, it is necessary to have a very good understanding of the noise sources of the device. To this end, the FPN and the dark count rate of the camera are estimated in the next sections.

5.2.4 Fixed Pattern Noise

Fig. 5.16a shows a typical bias frame, i.e. a frame taken with zero exposure time, at a read-out speed of 100 kHz. Hence, charge in the pixels could only

t_{exp} [s]	p [mm]	NE10A	NE20A	T [10^{-3}]	η [%]
1.0	5.50	•		13.41	$1.223 \pm 0.003(\mathrm{stat}) \pm 0.080(\mathrm{syst})$
2.5	5.70	•		5.81	$1.195 \pm 0.003(\mathrm{stat}) \pm 0.084(\mathrm{syst})$
5.0	5.60	•		9.05	$1.200 \pm 0.003(\mathrm{stat}) \pm 0.084(\mathrm{syst})$
5.0	5.61	•	•	0.50	$1.290 \pm 0.004(\mathrm{stat}) \pm 0.108(\mathrm{syst})$
5.0	5.61		•	4.96	$1.195 \pm 0.003(\mathrm{stat}) \pm 0.088(\mathrm{syst})$
5.0	5.81	•		3.46	$1.188 \pm 0.003(\mathrm{stat}) \pm 0.079(\mathrm{syst})$
5.0	5.81	•		3.46	$1.199 \pm 0.003(\mathrm{stat}) \pm 0.080(\mathrm{syst})$
100.0	5.95	•	•	0.10	$1.174 \pm 0.003(\mathrm{stat}) \pm 0.096(\mathrm{syst})$
combined					$1.208 \pm 0.002(\mathrm{stat}) \pm 0.079(\mathrm{syst})$

Table 5.3: Quantum efficiency measurements. Listed are the exposure time, the used attenuator setting, additional filters, the combined transmission and the quantum efficiency. The last row gives the combined result.

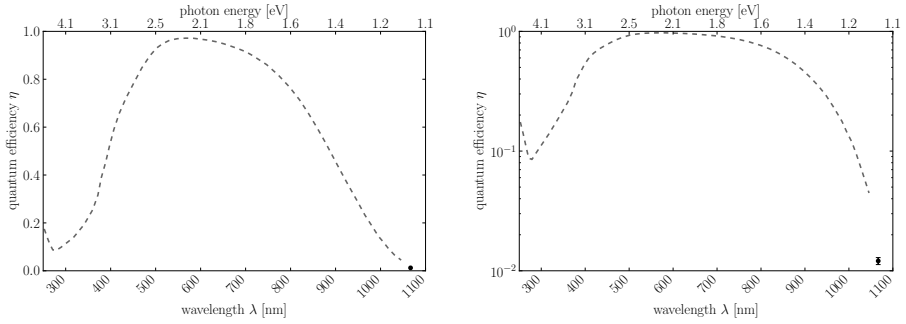

(a) **(b)**

Figure 5.15: Quantum efficiency of the examined PIXIS 1024B at a temperature of $-70\,^{\circ}\mathrm{C}$ for 1066.7 nm (dot) compared with the values specified in the data sheet (dashed) [159] in linear (a) and logarithmic (b) y-scale. The estimated error is too small to be visible in the linear scale plot.

accumulate due to dark counts during the time necessary to read out the CCD (at most 11 s for the pixels most distant from the read-out node). Because the camera was cooled to −70 °C the expected dark counts (0.01 e^-/px) are negligible compared to the read-out noise. The naive expectation for this frame is a regular image with random variations due to the read-out noise.

The observed frames however show some peculiar features. Fig. 5.16b shows the pixel values in rows $y = 10$ and 1000 of the frame shown in Fig. 5.16a. Both exhibit a steep rise in the first eight blank pixels. The 1056 columns of the imaging area show a slight positive gradient ($\sim 3\,\mathrm{ADU}/1000\,\mathrm{px}$). At the end of the imaging area ($x = 1064$), the read-out value drops. For row $y = 10$, the drop is smaller than for $y = 1000$ (4 ADU vs. 11 ADU). The level of the read-out values in the virtual columns is the same for both rows and constant with respect to the column index, x.

Profiles along different columns of the same frame are shown in Fig. 5.16c. For row $y = 0$ all profiles have approximately the same value. The profiles of the imaging area ($y = 200$ and 800) show a clear rise with increasing row index, y, that is independent on the column index and has a slope of 8 ADU/1000 px. In the profile of the virtual column ($x = 1100$) no such rise can be observed.

This indicates that an offset is added to pixels when they are shifted. Because the gradient within one column is much larger than the one within one row, the offset increment per shift within the imaging area is larger than the offset increment per shift within the transport register.

As the same offset shift is observable in all frames taken with zero exposure time, this pattern is the fixed pattern noise of the CCD camera. To correct for this a series of 50 frames was taken. The frames were corrected for variations of the per-row offset by subtracting the average of all virtual columns with $x \geq 1070$ in each row,

$$v_{f,\mathrm{cor}}(x,y) = v_f(x,y) - \frac{1}{N_{\mathrm{px}}} \sum_{x' \geq 1070} v_f(x',y)\ , \tag{5.7}$$

where $v_f(x,y)$ is the read-out value of a pixel in column x and row y of frame f and N_{px} is the number of pixels included in the sum. The value of 1070 was chosen in order to have a safety margin of 6 px to the end of the imaging area pixels in columns 1064 and below.

Fig. 5.17 shows quantiles of the profiles along rows $y = 10$ and 1000 and along columns $x = 200$ and 800 of the corrected 50 frames. The row(column) profiles of the 50 frames are stacked and the 5, 16, 50, 84, and 95 % quantiles are calculated in every column(row) from the respective 50 corrected pixel values,

$$q_\alpha(x,y) = \alpha\text{-quantile}\left\{v_{f,\mathrm{cor}}(x,y) : f \in \mathrm{frames}\right\}\ ,$$

where α is the probability.

The remaining scatter in each pixel can be estimated from the distances of the quantile curves. In case of a Gaussian distribution the distance of the 16 and 84 % quantiles, which contain 68 % of all values, equals approximately 2σ. The distance of the 5 and 95 % quantiles equals 3.29σ. The average distances of the two quantile curves are listed in Tab. 5.4. The parenthesized values are the distances divided by the appropriate factor and are an estimate for the overall noise. One can clearly see, that the noise increases when the distance to the

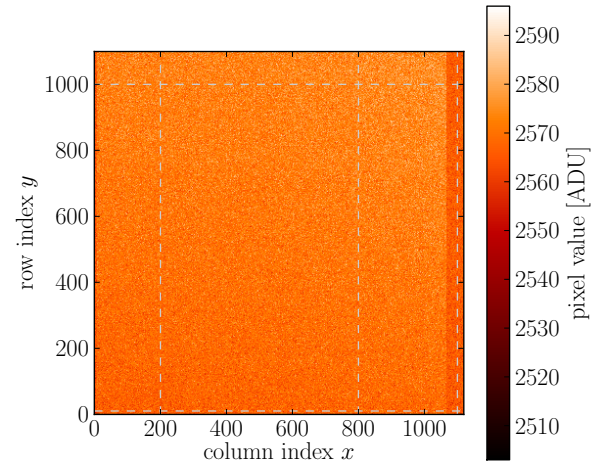

(a) Frame image

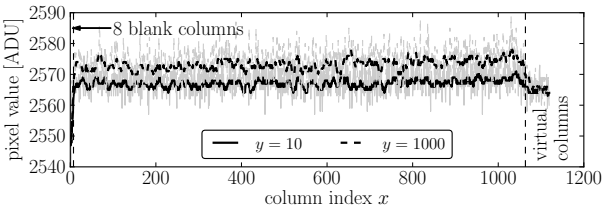

(b) Row profile

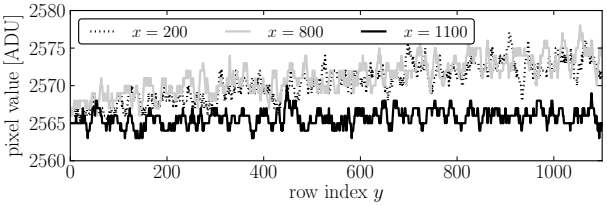

(c) Smoothed column profiles

Figure 5.16: A typical bias frame. (a) shows a bias frame taken at −70 °C with a read-out speed of 100 kHz. (b) shows the pixel values in rows $y = 10$ and 1000 of this frame. The gray lines are the pixel values, the black lines is smoothed by a box-filter of 10 px width. (c) shows the pixel values in columns $x = 200$, 800 and 1100 of this frame, again smoothed by a box-filter of 10 px width. The dashed lines in (a) indicate the location of examined rows and columns. The row profiles in (b) show a slight positive gradient ($\sim$ 3 ADU/1000 px). The gradient of the column profiles of the imaging area ($x = 200, 800$ in (c)) is steeper (8 ADU/1000 px). The virtual-column profile ($x = 1100$) shows no gradient. The gradients of row and column profiles are independent of the position in the imaging area of the chip.

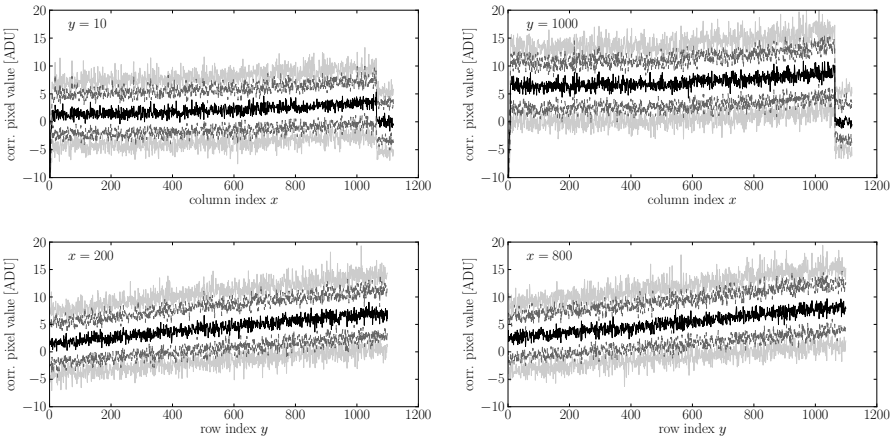

Figure 5.17: Row and column profiles of 50 corrected bias frames. Shown are the 5, 16, 50, 84 and 95 % (from bottom to top) quantiles to indicate the remaining scatter of the pixel values.

		avg. distance [ADU]	
row/column		$q_{84} - q_{16}$	$q_{95} - q_5$
$y =$	10	7.30 (3.65)	11.83 (3.60)
	1000	8.38 (4.19)	13.58 (4.13)
$x =$	200	7.86 (3.93)	12.71 (3.86)
	800	8.12 (4.06)	13.20 (4.01)
	[a]1100	6.55 (3.28)	10.65 (3.24)

[a]Virtual column. Not shown in Fig. 5.17

Table 5.4: Average distance of the 16 and 84 % and 5 and 95 % quantile curves in Fig. 5.17 corresponding to 2 and 3.29σ, respectively, for a Gaussian distribution. The values in parenthesis are the distances divided by the appropriate factors to estimate σ.

read-out structure increases. Fig. 5.18 shows the map of

$$\Delta q(x,y) = \frac{1}{2}[q_{0.84}(x,y) - q_{0.16}(x,y)] \approx \sigma \ .$$

One can clearly observe an increase with increasing row index for the pixels in the imaging area. For the pixels in the virtual columns $x \geq 1064$, such an increase is not observable. For pixels near the read-out structure at $(x, y) =$ (0,0), the observed values are below the value of the read-out noise given in the Certificate of Performance [184] ($3.85\,\mathrm{e}^- \mathrel{\widehat{=}} 3.77\,\mathrm{ADU}$; cf. Tab. 5.1) while this value is exceeded for pixels far away from the read-out structure.

In summary, for pixels in the imaging area, both the FPN offset and the read-out noise increase with the distance from the read-out structure. For the pixels in the virtual columns ($x \geq 1064$) such a behaviour is not observed. This indicates that this two-fold increase is caused by CIC. As the increase is largest

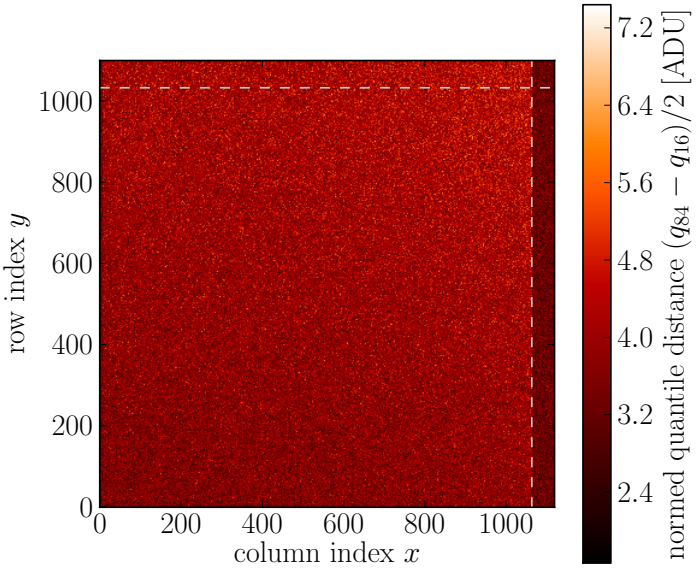

Figure 5.18: Map of scaled quantile distance in 50 corrected bias frames. Plotted is the distribution the distance of the 16 and 84 % quantiles scaled by 1/2 such that it corresponds to 1σ.

with increasing row index (cf. Figs. 5.16c and 5.18) most CIC is picked up during line-shifting. Because the virtual-column pixels are never line-shifted, they are only affected by the CIC accumulated during transfer through the read-out register. Thus, the observed noise in the virtual-column pixels is an estimate for the combination of the read-out noise, σ_{RO}, and the noise due to the accumulated CIC, σ_{CIC}. The average scaled quantile distance, $\langle \Delta q \rangle$ is

$$\langle \Delta q \rangle = \frac{1}{N_{\mathrm{px}}} \sum_{\substack{x \geq 1070 \\ y \in \mathrm{rows}}} \Delta q(x, y) = (3.290 \pm 0.002)\,\mathrm{ADU}\ ,$$

which corresponds to

$$\sqrt{\sigma_{\mathrm{RO}}^2 + \sigma_{\mathrm{CIC}}^2} = G\,\langle \Delta q \rangle = (3.356 \pm 0.002)\,\mathrm{e}^-\ ,$$

where a gain of $G = 1.02\,\mathrm{e}^-/\mathrm{ADU}$ was assumed. This value is below the value given in the Certificate of Performace [184] for the read-out noise ($3.85\,\mathrm{e}^-$; cf. Tab. 5.1).

5.2.5 Noise Map and Dark Count Rate

As seen in the previous section, the shifting of the pixel values adds a random noise component in addition to the FPN. Thus, the noise of each pixel is slightly different. The same can hold true for the dark count rate of each pixel. Therefore, the dark count rate of each pixel was estimated. To this end, dark frames were taken with exposure times of 0, 60, 300, 600, 900, 1200, and 2400 s. The frames were taken in a dedicated dark laboratory with black walls to ensure that no ambient light could contribute to the accumulated charges and mimic any dark counts. At all times, the room illumination was switched off and the control lamps of the laboratory controls where thoroughly covered. For each exposure time 50 frames were taken. Fig. 5.19a shows profiles of the virtual column $x = 1100$ for all exposures, where the global offset was corrected by subtracting the average of all virtual-column pixels,

$$v'_{\mathrm{cor},f}(x, y) = v_f(x, y) - \frac{1}{N_{\mathrm{px}}} \sum_{\substack{x' \geq 1070 \\ y' \in \mathrm{rows}}} v_f(x', y') \tag{5.8a}$$

$$= v_f(x, y) - \bar{v}_{\mathrm{virt},f}\ , \tag{5.8b}$$

where the same nomenclature as in Eq. (5.7) was used and $\bar{v}_{\mathrm{virt},f}$ is the global FPN offset of frame f estimated by the average of all virtual-column pixels. The profiles show that the FPN changes dramatically with the length of the exposure. This change is observable in all real and virtual columns. The shape of the FPN within one row does not depend on the exposure time as one can see in Fig. 5.19b. The offset of the curves in Fig. 5.19b is caused by the fact that the in-column profiles (cf. Fig. 5.19a) differ strongly at $y = 1050$.

Therefore, to estimate the dark count rate, each frame is corrected for this per-row offset (cf. Eq. (5.7)). Second, the remaining FPN is estimated from the $t_{\mathrm{exp}} = 0\,\mathrm{s}$ exposures by stacking the corrected 50 frames and calculating the median value from these 50 frames for every pixel,

$$FPN(x, y) = \mathrm{median}\left\{ v_{\mathrm{cor},f}(x, y) : f \in t_{\mathrm{exp}} = 0\,\mathrm{s\ frames} \right\}\ .$$

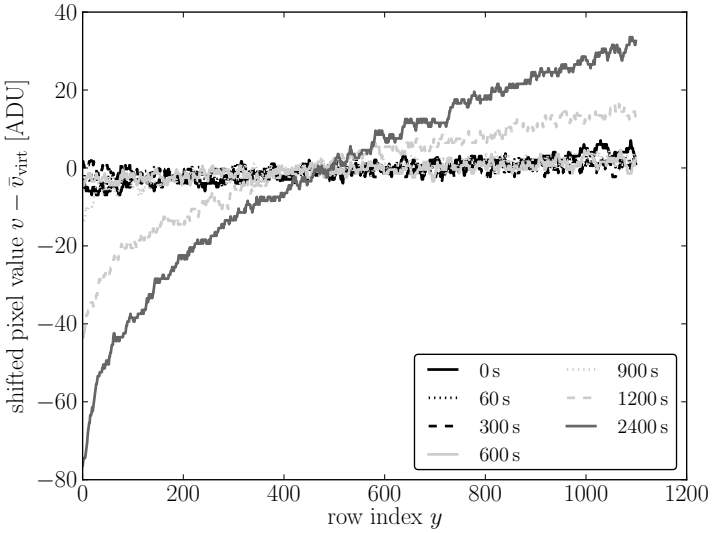

(a) Virtual column ($x = 1100$) profiles

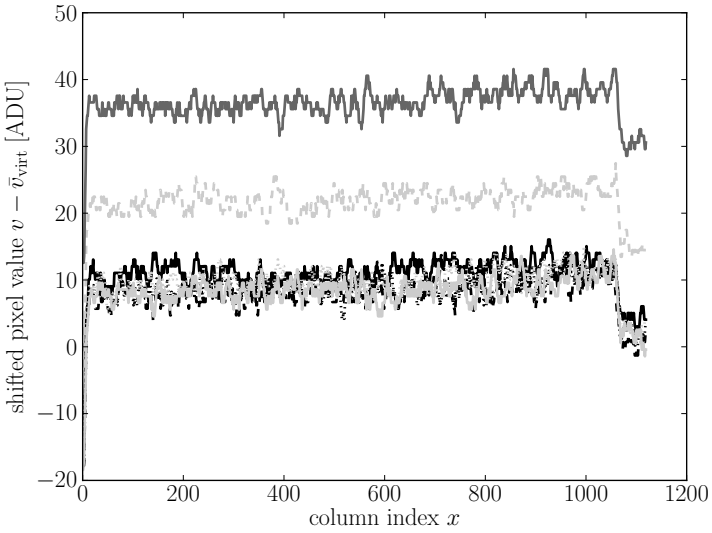

(b) Virtual row ($y = 1050$) profiles

Figure 5.19: Profile of virtual column $x = 1100$ (a) and virtual row $x = 1050$ (b) for different exposure times showing the variation of the FPN with exposure time. The profiles were corrected for a global offset accorting to Eq. (5.8).

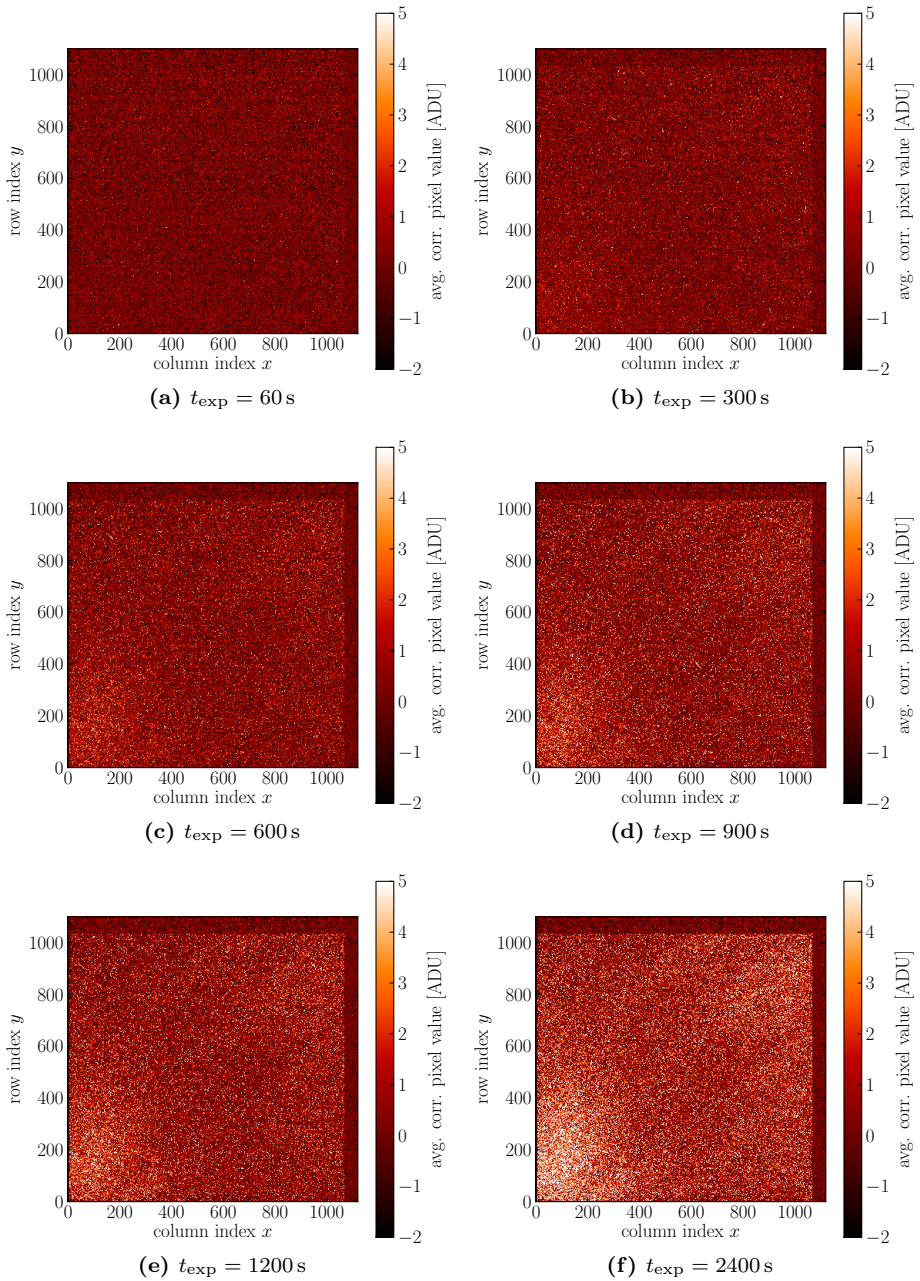

(a) $t_{\mathrm{exp}} = 60\,\mathrm{s}$ **(b)** $t_{\mathrm{exp}} = 300\,\mathrm{s}$

(c) $t_{\mathrm{exp}} = 600\,\mathrm{s}$ **(d)** $t_{\mathrm{exp}} = 900\,\mathrm{s}$

(e) $t_{\mathrm{exp}} = 1200\,\mathrm{s}$ **(f)** $t_{\mathrm{exp}} = 2400\,\mathrm{s}$

Figure 5.20: Averaged dark frames. The frames were corrected for per-row variations and the FPN observed at $t_{\mathrm{exp}} = 0\,\mathrm{s}$. To visualize the pattern the color scale was clipped at 25 and 75 % quantiles of the 2400 s data.

The median is chosen here to reduce the sensitivity to possible outliers. This FPN frame is then subtracted from every frame. Hence, after this procedure, the final corrected pixel values, c_f, are given by

$$c_f(x,y) = v_{\mathrm{cor},f}(x,y) - FPN(x,y) \; .$$

Spurious hot pixels in the imaging area, caused by e.g. cosmic ray muons or ambient radioactivity, are masked by an iterative procedure. Let

$$m_{\mathrm{r},f}(y) = \frac{1}{N_{\mathrm{px}}} \sum_{\substack{x \text{ not} \\ \text{masked}}} c_f(x,y)$$

be the average pixel value of all non-masked pixels in row y and

$$s^2_{\mathrm{r}f}(y) = \frac{1}{N_{\mathrm{px}}-1} \sum_{\substack{x \text{ not} \\ \text{masked}}} \left[c_f(x,y) - m_{\mathrm{r},f}(x,y)\right]^2$$

the empirical variance of these pixels. The iterative process is started by masking the highest valued pixel in row y. If the masked pixel x_{m} has a corrected value

$$c_f(x_{\mathrm{m}},y) > m_{\mathrm{r},f}(y) + k\, s_{\mathrm{r},f}(y) \; , \tag{5.9}$$

it remains masked and the iteration continues by masking the next highest valued pixel of the remaining non-masked pixels. The iteration is stopped when no pixel is found, i.e. when condition (5.9) is not fulfilled. In this case, the last masked pixel is unmasked again and the values of the remaining unmasked pixels in row y are considered to be valid. A value of $k = 4.26$ was chosen. This corresponds to a relative loss of 10^{-5} in case of a Gaussian distribution with no spurious hot pixels.

This cleaning procedure is done row-by-row because this way the algorithm can be applied with or without prior correction of the vertical FPN offset variation (Eq. (5.7)). Adapting this algorithm to work on a per-frame base, i.e. analyzing all pixel of a frame at once, does not change the list of masked pixels significantly.

The frames with the same exposure time, t, are stacked and for every pixel the average, $m_t(x,y)$, is calculated from the valid values of the 50 frames,

$$m_t(x,y) = \frac{1}{N_{\mathrm{fr}}(x,y)} \sum_{f \in \mathcal{V}_t(x,y)} c_f(x,y) \; ,$$

where the set $\mathcal{V}_t(x,y)$ contains all frames for a given exposure time in which pixel (x,y) is valid and N_{fr} is the number of these frames. In Fig. 5.20 the result of this procedure is shown for $t_{\mathrm{exp}} = 60$, 300, 600, 900, 1200, and 2400 s. One can observe that the generation of dark counts is not uniform over the whole frame. Instead, the corner nearest to the read-out at $(0,0)$ shows the strongest increase of $m_t(x,y)$ with exposure time. For $t_{\mathrm{exp}} \geq 300\,\mathrm{s}$, one can nicely observe the darker virtual pixels at the top and right edges, which do not accumulate dark counts.

For a constant dark count rate, R_{DC}, $m_t(x,y)$ is expected to be proportional to the exposure time, t,

$$m_t(x,y) = O(x,y) + R_{\mathrm{DC}}(x,y)\, t \; , \tag{5.10}$$

where the offset O was included to take into account imperfections of the correction algorithm described above, e.g. estimating of the FPN by taking the median of the $t = 0\,\mathrm{s}$ frames. Because the accumulation of dark charges is a process described by Possonian statistics, the variance due to $R_{\mathrm{DC}}(x, y)\, t$ is expected to be proportional to t as well,

$$\mathrm{var}_t(x, y) \propto t \; . \tag{5.11}$$

To verify that this additional time-dependent signal is caused by accumulated electric charges in the pixels of the CCD and not by e.g. unresolved exposure-time dependent FPN variablility, the time dependence of the variance of the signal was estimated and compared to the expectation Eq. (5.11). To estimate the variance of the signal in a pixel, the empirical variance, $s^2_{\mathrm{ip},t}(x, y)$, of the stacked frames was calculated,

$$s^2_{\mathrm{ip},t}(x, y) = \frac{1}{N_{\mathrm{fr}}(x, y) - 1} \sum_{f \in \mathcal{V}_t(x,y)} \left[c_f(x, y) - m_t(x, y)\right]^2 \; . \tag{5.12}$$

Fig. 5.21 shows $s^2_{\mathrm{ip},t}(x, y)$ for the different exposure times. The images with short exposure times (e.g. Figs. 5.21a and 5.21b) show a non-uniform distribution of the observed variances as expected from the CIC observed in the previous section. The variance increases for pixels farther away from the read-out structure. This coincides with the observed non-uniformity of the CIC and the resulting non-uniform distribution of the noise (cf. Fig. 5.18 and Tab. 5.4).

When the exposure time is increased, the pattern of the in-pixel variance changes. The increase in variance is largest in the lower left corner near pixel $(0, 0)$, corresponding to the hot spot in the averaged dark frames (Fig. 5.20).

Fig. 5.22 compares the increase in dark counts with the increase in in-pixel variance for four different regions of interest (ROIs) in the imaging area, which are defined in Tab. 5.5. The dark counts in a ROI, m_{ROI}, are estimated by averaging all valid pixel values for each exposure time,

$$\begin{aligned} m_{\mathrm{ROI}}(t) &= \frac{1}{N_{\mathrm{px}}} \sum_{x,y \in \mathrm{ROI}} \frac{1}{N_{\mathrm{fr}}(x, y)} \sum_{f \in \mathcal{V}_t(x,y)} c_f(x, y) \\ &= \frac{1}{N_{\mathrm{px}}} \sum_{x,y \in \mathrm{ROI}} m_t(x, y) \; , \end{aligned} \tag{5.13}$$

which, following Eq. (5.10), is expected to increase linearly with the exposure time,

$$m_{\mathrm{ROI}}(t) = O'(\mathrm{ROI}) + R_{\mathrm{DC}}(\mathrm{ROI})\, t \; , \tag{5.14}$$

where O' accounts for imperfections of the correction procedure (cf. Eq. (5.10)).

To combine the different in-pixel variances, s^2_{ip}, in one ROI, a maximum likelihood estimator for the variance was used,

$$\hat{\sigma}^2_{\mathrm{ML}}(t) = \sum_{x,y \in \mathrm{ROI}} \left(N_{\mathrm{fr}}(x, y) - 1\right) s^2_{\mathrm{ip},t}(x, y) \Bigg/ \sum_{x,y \in \mathrm{ROI}} \left(N_{\mathrm{fr}}(x, y) - 1\right) \; , \tag{5.15}$$

i.e. the weighted mean with the number of degrees of freedom of the empirical variance $(N_{\mathrm{fr}}(x, y) - 1)$ as weights. This estimator is unbiased because the

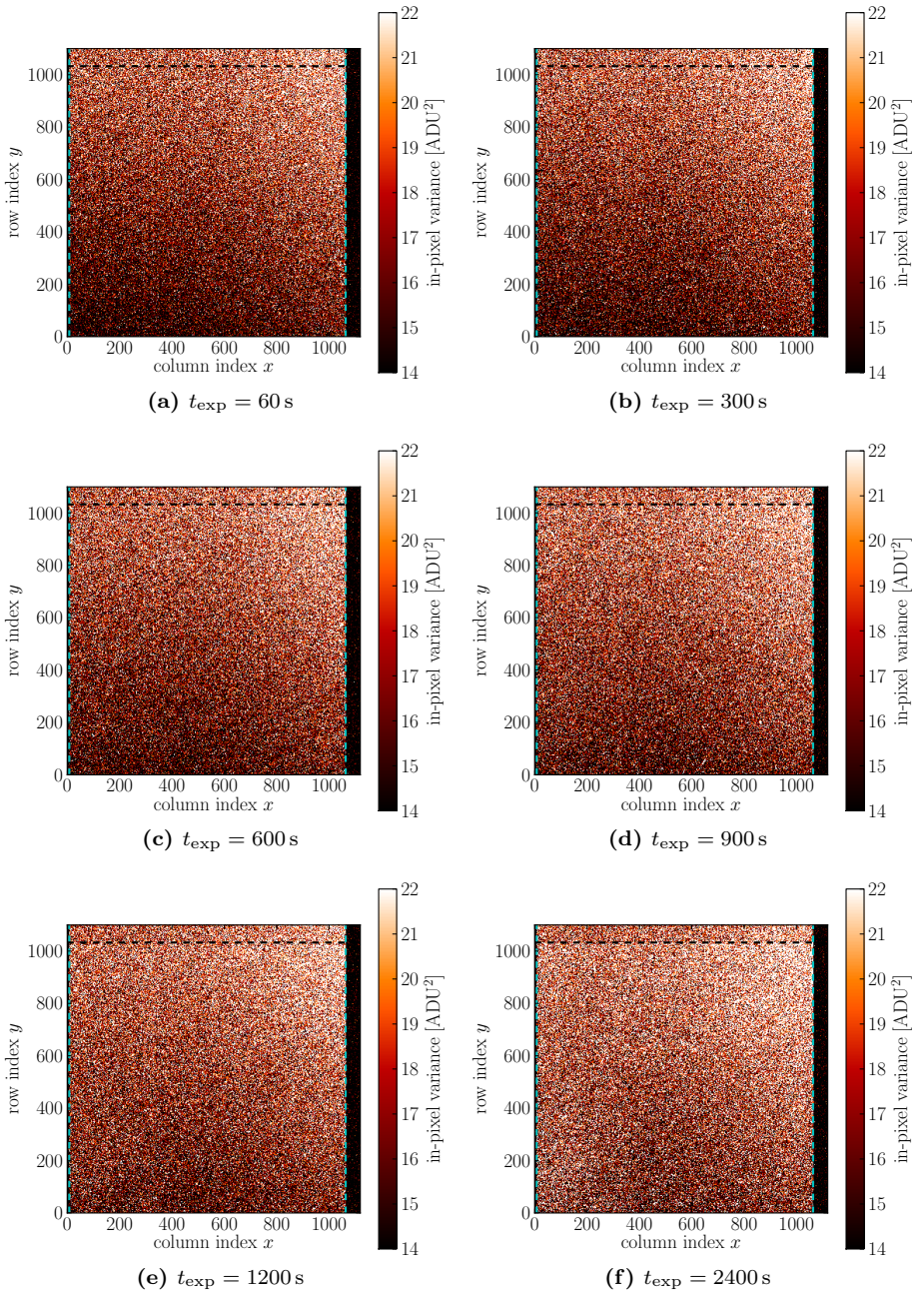

(a) $t_{\mathrm{exp}} = 60\,\mathrm{s}$ **(b)** $t_{\mathrm{exp}} = 300\,\mathrm{s}$

(c) $t_{\mathrm{exp}} = 600\,\mathrm{s}$ **(d)** $t_{\mathrm{exp}} = 900\,\mathrm{s}$

(e) $t_{\mathrm{exp}} = 1200\,\mathrm{s}$ **(f)** $t_{\mathrm{exp}} = 2400\,\mathrm{s}$

Figure 5.21: In-pixel variance frames. The frames were corrected for per-row variations and the FPN observed at $t_{\mathrm{exp}} = 0\,\mathrm{s}$. To visualize the pattern the color scale was clipped at the lowest 25 % and highest 75 % quantiles of all frames. The dashed lines indicate the boundaries of the imaging area.

ROI	columns x	rows y
top left	150 ... 200	800 ... 850
top right	800 ... 850	800 ... 850
bottom left	150 ... 200	150 ... 200
bottom right	800 ... 850	150 ... 200

Table 5.5: Definition of the regions of interest (ROIs) used in Fig. 5.22. Note that the indexing of rows and columns starts at $x, y = 0$ and the upper bound of the given ranges is exclusive, e.g. the interval $x_a \ldots x_b$ contains columns $x_a \leq x < x_b$.

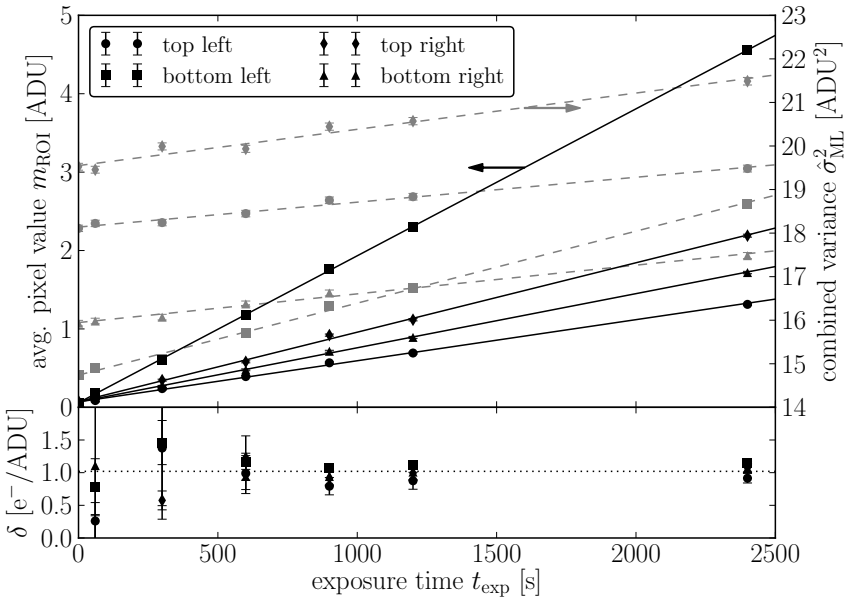

Figure 5.22: Average pixel value and variance for different ROIs. Upper panel: Shown are the average pixel value (black, left scale, Eq. (5.13)) and variance estimator (gray, right scale, Eq. (5.15)) on different scales for four different ROIs defined in Tab. 5.5. The solid black lines are linear fits of the average pixel values, Eq. (5.14). The dashed gray lines are linear fits of the combined variance, Eq. (5.16). See Tab. 5.6 for numerical results. Lower panel: Shown is the ratio of increases, Eq. (5.17). The dotted line represents the expectation for a gain of $G = 1.02\,\mathrm{e}^-/\mathrm{ADU}$. Refer to the text for more details.

ROI	O' [ADU]	R_{DC} [$10^{-4}\,\mathrm{ADU\,px^{-1}\,s^{-1}}$]	χ^2/N_{df}
top left	0.0698 ± 0.0067	5.242 ± 0.069	1.8
top right	0.0730 ± 0.0071	8.855 ± 0.079	4.1
bottom left	0.0587 ± 0.0063	18.743 ± 0.076	1.2
bottom right	0.0690 ± 0.0063	6.905 ± 0.067	1.2

(a) Fit to mean pixel values $m_{\mathrm{ROI}}(t)$

ROI	σ^2_{RO} [ADU^2]	ζ [$10^{-4}\,\mathrm{ADU^2\,px^{-1}\,s^{-1}}$]	χ^2/N_{df}
top left	18.138 ± 0.040	5.72 ± 0.38	0.7
top right	19.550 ± 0.043	8.32 ± 0.41	2.9
bottom left	14.739 ± 0.033	16.53 ± 0.34	1.5
bottom right	15.946 ± 0.035	6.59 ± 0.33	0.7

(b) Fit to combined variance $\hat{\sigma}^2_{\mathrm{ML}}$

Table 5.6: Results of the fits in Fig. 5.22. The last column lists the reduced χ^2 of the fits as an estimate for the goodness-of-fit. (a) The average pixel value was fitted by Eq. (5.14). (b) The combined variance was fitted by Eq. (5.16).

empirical variance of Eq. (5.12) is unbiased. The associated 68 % CL interval is given by an uncertainty of

$$\Delta\hat{\sigma}^2_{\mathrm{ML}}(t) = \frac{2\left[\hat{\sigma}^2_{\mathrm{ML}}(t)\right]^2}{\sum\limits_{x,y\in\mathrm{ROI}} (N_{\mathrm{fr}}(x,y)-1)\left[2s^2_{\mathrm{ip},t}(x,y) - \hat{\sigma}^2_{\mathrm{ML}}(t)\right]} \,.$$

The upper panel of Fig. 5.22 shows the average pixel value, $m_{\mathrm{ROI}}(t)$, and the combined variance, $\hat{\sigma}^2_{\mathrm{ML}}(t)$, on different scales. The increase of the average pixel value due to accumulated dark counts is visible. At $t_{\mathrm{exp}} = 0\,\mathrm{s}$ the same average pixel value, $m_{\mathrm{ROI}}(t)$, is found for all four ROIs, while they differ for higher exposure times. This indicates that a residual FPN remained after the correction of the FPN.

At $t_{\mathrm{exp}} = 0\,\mathrm{s}$, the combined variance values have different values in the four ROIs. This is expected from the observed noise variation due to CIC. Similar to the average pixel value, the increase of the combined variance depends on the position of the ROI.

Eq. (5.14) is fitted to the average pixel value. The combined variance is fitted by

$$\hat{\sigma}^2_{\mathrm{ML}}(t) = \sigma^2_{\mathrm{RO}} + \zeta\, t \,. \tag{5.16}$$

The numerical results of these fits are listed in Tab. 5.6. The quality of the fits is good as indicated by the values of the reduced χ^2 (χ^2/N_{df}) in the last columns. The reason for the high reduced χ^2 value of the fit of the values of the top right ROI is unknown. A possible cause is an unsystematic temperature fluctuation of this part of the CCD chip in the frames taken with exposure times $t_{\mathrm{exp}} \leq 300\,\mathrm{s}$, which causes a deviation from the linear behaviour of m_{ROI} and $\hat{\sigma}^2_{\mathrm{ML}}$. The observed non-zero offset O' in Tab. 5.6a for all four ROIs is caused by a residual FPN mentioned above.

The dark count rates in the top left and bottom right ROIs are below the value specified by the vendor [184] (see Tab. 5.1),

$$8 \times 10^{-4}\,\mathrm{e}^{-}/(\mathrm{px\,s}) \mathrel{\widehat{=}} 7.8 \times 10^{-4}\,\mathrm{ADU}/(\mathrm{px\,s})\ .$$

The dark count rate in the top right ROI is slightly above this value, while in the bottom left ROI, i.e. near the read-out structure, the observed dark count rate exceeds this value by more than a factor of two.

The ADU dark count rate, R_{DC}, estimated above is related to the physical dark charge production rate Γ_{e} by the gain, G, of the ADC,

$$R_{\mathrm{DC}} = \frac{1}{G}\,\Gamma_{\mathrm{e}}\ .$$

The same is true for the total dark counts, N_{DC}, accumulated over an exposure time, t_{exp},

$$N_{\mathrm{DC}} = R_{\mathrm{DC}}\,t_{\mathrm{exp}} = \frac{1}{G}\,N_{\mathrm{e}}\ ,$$

where $N_{\mathrm{e}} = \Gamma_{\mathrm{e}} \cdot t_{\mathrm{exp}}$ is the number of accumulated dark charges. As N_{e} is distributed after a Poissonian distribution, the uncertainty of N_{DC} is given by

$$\sigma_{\mathrm{DC}} = \frac{1}{G}\sqrt{N_{\mathrm{e}}}\ .$$

Hence, the total variance of the read-out, digitized signal is given by

$$\begin{aligned}\sigma^2_{\mathrm{tot}} &= \sigma^2_{\mathrm{DC}} + \sigma^2_{\mathrm{RO}} \\ &= \frac{1}{G^2}\,N_{\mathrm{e}} + \sigma^2_{\mathrm{RO}}\ .\end{aligned}$$

The ratio, δ, of the increase of accumulated dark counts $(m_{\mathrm{ROI}}(t) - m_{\mathrm{ROI}}(0\,\mathrm{s}))$ and the increase of the observed total noise $(\hat{\sigma}^2_{\mathrm{ML}}(t) - \hat{\sigma}^2_{\mathrm{ML}}(0\,\mathrm{s}))$ is given by

$$\delta = \frac{m_{\mathrm{ROI}}(t) - m_{\mathrm{ROI}}(0\,\mathrm{s})}{\hat{\sigma}^2_{\mathrm{ML}}(t) - \hat{\sigma}^2_{\mathrm{ML}}(0\,\mathrm{s})} = \frac{[R_{\mathrm{DC}}\,t + O'] - O'}{[\sigma^2_{\mathrm{DC}} + \sigma^2_{\mathrm{RO}}] - \sigma^2_{\mathrm{RO}}} = \frac{\frac{1}{G}\,\Gamma_{\mathrm{e}} t}{\frac{1}{G^2}\,\Gamma_{\mathrm{e}} t} = G\ , \qquad (5.17)$$

and, hence, can be used to estimate the gain of the ADC. The lower panel of Fig. 5.22 shows this ratio. The observed values for the gain are in good agreement with the value, $G = 1.02\,\mathrm{e}^{-}/\mathrm{ADU}$, specified by the vendor (Tab. 5.1, [184]) and indicated by the dotted line in the lower panel of Fig. 5.22.

Alternatively, using Eqs. (5.14) and (5.16), one finds

$$G = \frac{R_{\mathrm{DC}}}{\zeta}\ . \qquad (5.18)$$

Tab. 5.7 lists the resulting gain for the four ROIs. The averaged value is

$$G = (1.041 \pm 0.025)\,\frac{\mathrm{e}^{-}}{\mathrm{ADU}}\ ,$$

which agrees with the vendor specified value.

ROI	G [e $^-$/ADU]
top left	0.916 ± 0.061
top right	1.063 ± 0.053
bottom left	1.134 ± 0.024
bottom right	1.048 ± 0.054
average	1.041 ± 0.025

Table 5.7: Estimation of the gain using Eq. (5.18). Listed are the estimates of the gain, G, based on the results of the linear fits in Fig. 5.22. The last row shows the average of the four ROIs.

To conclude, after correcting the measured data, the dark count rate was estimated. The estimation of the associated noise confirms that the increased signal is indeed caused by accumulated charges. Similar to the FPN, the dark count rate shows a non-trivial distribution over the imaging area, which is most likely caused by unbalanced cooling of the chip. Except for the region near the read-out structure, the observed dark count rate has the same order of magnitude as the value specified by the vendor. The measured gain of the ADC matches the vendor-specified value.

Discussions with the vendor [189] indicate that the reason for the non-uniform dark count rate is an error in the firmware of the control electronics of the CCD chip. Because of this error, some parts of the control electronics near the chip are not properly switched off during operation. This produces a non-uniform thermal load on the CCD chip. The resulting temperature gradient causes spatial variations of the rate at which charge is produced due to thermal noise and, hence, the observed non-uniform dark count rate. Unfortunately, an update for the firmware is not available.

Looking at the in-pixel variance frame for an exposure time of 2400 s in Fig. 5.21f, the region with the lowest total noise, σ_{tot}, is near pixel $(600, 200)$. Its noise level is even below the bottom-right ROI, which has the lowest noise level of all four analysed ROIs (cf. Fig. 5.22). Extrapolating the fits of Eq. (5.16) to the combined variance to an exposure time of one hour, shows that the bottom right ROI remains the ROI with the lowest noise. Therefore, the pixels in rows $y < 400$ and columns $x > 600$ are preferred for data taking.

5.3 Statistical Analysis

Because ALPS-II will be probing new parameter space, it cannot be predicted if a signal will be found or not. Therefore, the algorithm for the analysis has to be prepared for both of these cases. The analysis is based on the assumption that the potential signal is contained in one pixel of the CCD, which can be arranged for by means of binning the hardware pixels into logical pixels. The analysis uses frequentist statistics. The confidence intervals are constructed using likelihood ratios [136] and hybrid resampling is used to treat nuisance parameters [190, 191].

This section describes the statistical model used for the data and an analysis algorithm based on hybrid resampling. This algorithm is compared to a simpler

algorithm that was used in ALPS-I but does not take nuisance parameters into account. Additionally, the sensitivities for two benchmark configurations are presented and compared to the sensitivity of a TES and an EMCCD.

5.3.1 Observable

The read-out value, v, of pixel (x, y), is corrected for the per-row FPN offset according to Eq. (5.7) and is then multiplied by the gain, G, of the camera's ADC to acquire corrected values, c, in units of electron counts. This corrected value consists of several components

$$c(x, y) = S + R_{\mathrm{DC}}\, t_{\mathrm{exp}} + \mathit{FPN}(x, y) \ ,$$

where S is the component due to charges produced by incident light. The second term is due to the dark current produced at a rate R_{DC} and integrated over the exposure time t_{exp} and may depend on the coordinates of the pixel. *FPN* represents any residual fixed pattern of the used correction algorithm. The first two components are Poisson distributed. The read-out noise, σ_{RO}, is attributed to the fixed pattern. Note that, in contrast to the previous Sec. 5.2, the symbols here denote quantities in units of electrons not ADUs. As the components are additive, the distribution of c is given by a convolution,

$$c \sim \mathrm{Poi}(\lambda_{\mathrm{sig}}) \oplus \mathrm{Poi}(R_{\mathrm{DC}} t_{\mathrm{exp}}) \oplus \mathcal{N}(\mathit{FPN}(x, y), \sigma_{\mathrm{RO}}) \ ,$$

where $\sim$ is used to denote "is distributed as". $\mathrm{Poi}(\lambda)$ is a Poisson distribution with expectation value λ, λ_{sig} is the expectation value for the number of charges produced by incident light, $\mathcal{N}(\mu, \sigma)$ is a Gaussian distribution with expectation value μ and standard deviation σ, and $\oplus$ is used to denote the convolution. For large constant exposure times, the dark count and FPN component can be combined for simplicity,

$$\mathrm{Poi}(R_{\mathrm{DC}} t_{\mathrm{exp}}) \oplus \mathcal{N}(\mu'_{\mathrm{FPN}}, \sigma_{\mathrm{RO}}) \simeq \mathcal{N}\left(\mu_{\mathrm{FPN}}, \sigma_{\mathrm{B}}\right) \ ,$$

where $\sigma_{\mathrm{B}}^2 = R_{\mathrm{DC}} t_{\mathrm{exp}} + \sigma_{\mathrm{RO}}^2$ is now the variance of the background in each pixel and μ_{FPN} contains the residual fixed pattern and the accumulated dark charges. Fig. 5.23 compares the cumulative distribution function of this approximation with the exact result from the convolution. The good agreement between the two curves justifies that this simplification will be used in the following,

$$c \sim \mathrm{Poi}(\lambda_{\mathrm{sig}}) \oplus \mathcal{N}(\mu_{\mathrm{FPN}}, \sigma_{\mathrm{B}}) \ .$$

As seen in the previous section, the CCD shows a complicated FPN structure and a non-uniform dark count rate. A flexible method to handle this was developed for ALPS-I [51]. It takes a large number of pixels located near the signal pixel to estimate the local FPN and accumulated dark charges.

These pixels are scanned for hits from cosmic rays or ambient radioactivity and other spurious hot pixels by an iterative procedure. The procedure is similar to that used to mask spurious hot pixels before when the in-pixel variance was calculated (cf. Sec. 5.2.5). First, the pixel with the largest value is masked. Second, the average, m, and empirical standard deviation, s, of the remaining pixels are calculated. If the value of the pixel is above $m + k \cdot s$, this pixel stays

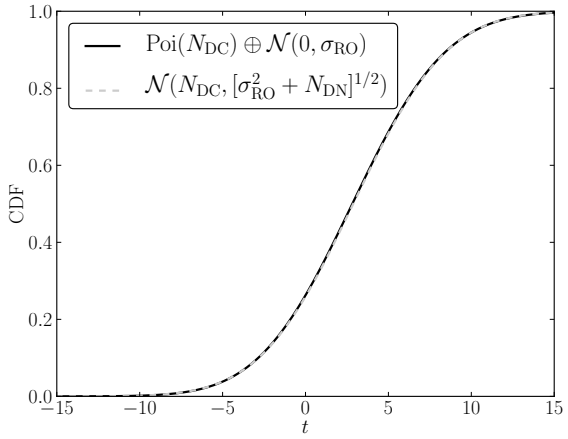

Figure 5.23: Comparison of the cumulative distribution functions (CDFs) of a convolution of a Poisson and Gauss distribution with an approximation by a Gauss distribution. The parameter used are typical expectations for the PIXIS CCD when used in ALPS-II: $N_{\mathrm{DC}} = 2.88\,\mathrm{e}^-$, $\sigma_{\mathrm{RO}} = 4.1\,\mathrm{e}^-$.

masked and the procedure continues at the first step by masking the largest-value pixel of the remaining pixels. Otherwise the pixel is unmasked and the iteration is stopped. If a pixel in the direct neighborhood of the signal pixel was masked by this procedure, the complete frame is excluded from the further analysis. This is done to make sure that no signal is mimicked by a potential influence of the masked pixel on the signal pixel.

After this, the average of the remaining, i.e. valid pixels is calculated and subtracted from the value of the signal pixel located at $(x_{\mathrm{s}}, y_{\mathrm{s}})$,

$$t = c(x_{\mathrm{s}}, y_{\mathrm{s}}) - \frac{1}{N_{\mathrm{valid}}} \sum_{x,y \in \mathrm{n-hood}} c(x, y) \;, \tag{5.19}$$

where the sum runs over all non-masked pixels and N_{valid} is the number of the valid pixels. Because the sum runs over pixels where no signal is expected, t is distributed as

$$t \sim \mathrm{Poi}(\lambda_{\mathrm{sig}}) \oplus \mathcal{N}\left(\mu, \sigma_{\mathrm{B}} \left[1 + 1/N_{\mathrm{valid}}\right]^{1/2}\right) \;. \tag{5.20}$$

Let

$$P_{\mathrm{P}}(k; \lambda) = e^{-\lambda} \frac{\lambda^k}{k!}$$

denote the probability mass function of the Poisson distribution with expectation value λ and

$$f_{\mathrm{G}}(x; \mu, \sigma) = \frac{1}{\sqrt{2\pi}\,\sigma} \exp\left(-\frac{(x-\mu)^2}{2\sigma^2}\right) \;.$$

the probability density function (PDF) of the Gauss distribution with mean μ

and variance σ^2. The PDF for t is then given by

$$\begin{aligned} f(t;\lambda_{\text{sig}},\mu,\sigma_{\text{B}}) &= \sum_{k=0}^{\infty} P_{\text{P}}(k;\lambda_{\text{sig}})\, f_{\text{G}}(t-k;\mu,\sigma_{\text{B}}) \\ &= \frac{e^{-\lambda_{\text{sig}}}}{\left[2\pi\sigma_{\text{B}}^2(1+1/N_{\text{valid}})\right]^{1/2}} \cdot \\ &\quad \cdot \sum_{k=0}^{\infty} \frac{\lambda_{\text{sig}}^k}{k!} \exp\left(-\frac{(t-k-\mu)^2}{2\sigma_{\text{B}}^2(1+1/N_{\text{valid}})}\right) , \end{aligned} \tag{5.21}$$

where λ_{sig} is the parameter of interest and μ and σ_{B} are nuisance parameters.

5.3.2 Analysis Algorithm

The run procedure for the CCD operation in ALPS-II foresees to run the experiment in dedicated on (off) modes where a signal is (not) expected [160]. To construct a confidence interval for λ_{sig}, the method proposed by Sen et al. [190] is used which extends the "unified method" [136] to problems which include nuisance parameters.

The Unified Method

The concept of confidence intervals was introduced by Neyman [192]. Assume an observable X that is distributed after some PDF $f(x;\theta)$ with parameter θ. A confidence interval for θ is defined by

$$P[\theta_1(x) \leq \theta \leq \theta_2(x)] \geq 1-\alpha \,, \tag{5.22}$$

where the interval bounds $\theta_{1,2}$ are functions of the measured value x. Eq. (5.22) is interpreted as follows: If the experiment is repeated n times each experiment will yield a different confidence interval

$$[\theta_1(x_i), \theta_2(x_i)] \qquad (1 \leq i \leq n) \,.$$

These intervals will contain the constant but unknown true value θ in a fraction $1-\alpha$ of the conducted experiments [136]. $1-\alpha$ is then the confidence level (CL) of the interval. The probability that the confidence level does not include the true value is given by α. This is known as "type I error". For a given value of θ, a confidence interval has *(over-)coverage* if Eq. (5.22) holds with (in-)equality. If Eq. (5.22) does not hold, the interval has *undercoverage*, which is considered a serious flaw.

Fig. 5.24a illustrates the classical construction of confidence intervals. First, for every value, θ', of the parameter θ intervals $[x_1(\theta'), x_2(\theta')]$ are calculated such that

$$P(x_1 \leq x \leq x_2) \geq 1-\alpha \,.$$

The endpoints of this intervals define functions $x_{1,2}(\theta)$. Assuming $x_{1,2}$ to be monotonic, these functions can be inverted

$$\theta_1 = x_2^{-1} \,, \qquad\qquad \theta_2 = x_1^{-1} \,,$$

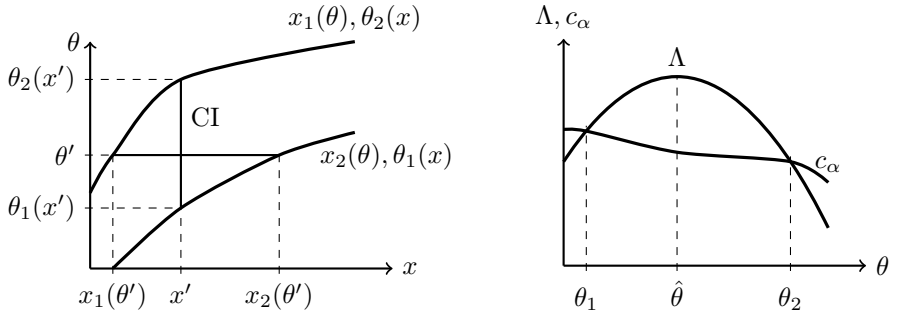

(a) Classical construction **(b)** Using critical values

Figure 5.24: Construction of confidence intervals. (a) illustrates the classical construction [192]. (b) shows the construction based on likelihood ratios [136, 190].

giving the functions $\theta_{1,2}$ used in Eq. (5.22). The interval $[\theta_1(x'), \theta_2('x)]$ then has coverage for every measured value x' [192].

The intervals defined by Eq. (5.22) are not unique as different choices of functions $x_{1,2}$ can produce intervals $[\theta_1, \theta_2]$ satisfying Eq. (5.22). Feldman and Cousins [136] propose to construct $x_{1,2}$ by ordering the x-values by their likelihood ratios,

$$\Lambda(\theta; x) = \frac{\mathcal{L}(\theta; x)}{\mathcal{L}(\hat{\theta}(x); x)} \ ,$$

where $\mathcal{L}(\theta; x) = f(x; \theta)$ is the likelihood function and $\hat{\theta}(x)$ maximizes the likelihood over the range of allowed values of θ. Starting with the maximizing value

$$x_{\text{start}}(\theta) = \arg\max_x \Lambda(\theta; x) \ ,$$

the x values with the highest likelihood ratios are added to the interval until the requested coverage is reached.

Realizing that Λ is a random variable, this is equivalent to finding a critical value $c_\alpha(\theta)$ for each allowed value of θ that solves

$$P[\Lambda(\theta; x) \geq c_\alpha(\theta) : x \sim f(x; \theta)] \geq 1 - \alpha \ , \tag{5.23}$$

where $c_\alpha(\theta)$ is chosen to be the largest value that satisfies this condition. As shown in Fig. 5.24b, for a measured value x' the confidence interval is then given by

$$\{\theta : \Lambda(\theta; x') \geq c_\alpha(\theta)\} \ . \tag{5.24}$$

This method nicely solves the problem of choosing whether a one- or two-sided interval should be calculated in cases with a constrained parameter space, hence its name "unified method".

The Hybrid Method

The unified method of constructing confidence intervals can be easily extended to cases with nuisance parameters, ν. Eq. (5.23) has to be extended to hold for

all values of the nuisance parameters,

$$P[\Lambda(\theta; x) \geq c_\alpha(\theta) : x \sim f(x; \theta, \nu)] \geq 1 - \alpha \qquad \forall \nu \; . \tag{5.25}$$

The likelihood ratio is now given by

$$\Lambda(\theta; x) = \frac{\mathcal{L}(\theta, \hat{\hat{\nu}}(x, \theta); x)}{\mathcal{L}(\hat{\theta}(x), \hat{\nu}(x); x)} \; ,$$

where $\hat{\theta}$ and $\hat{\nu}$ globally maximize the likelihood for given x, and $\hat{\hat{\nu}}$ maximizes the numerator for given θ and x.

The problem of this approach is that Eq. (5.25) has to be verified for the whole nuisance parameter space, which is typically of infinite size. The *hybrid method* solves this problem [191, 193, 194]. Instead of sampling x from $f(x; \theta, \nu)$ a modified PDF is used,

$$x^* \sim f^*(x^*; \theta, x') = f(x^*; \theta, \hat{\hat{\nu}}(\theta, x')) \; ,$$

where x' is the measured value. The critical value c^*_α is then defined by

$$P[\Lambda(\theta; x^*) \geq c^*_\alpha(\theta, x') : x^* \sim f^*(x^*; \theta, x')] \geq 1 - \alpha \; .$$

Modifying Eq. (5.24) accordingly yields the corresponding confidence interval

$$\{\theta : \Lambda(\theta; x') \geq c^*_\alpha(\theta, x')\} \; ,$$

where x' is again the measured value, which the critical value c^*_α now depends on. The belief that this method gives proper coverage is founded both on asymptotic arguments and simulations [191, 194].

Hybrid Confidence Intervals for λ_{sig}

Using the hybrid method allows to construct confidence intervals for λ_{sig}. A sample of the CCD data consists of n *off* and m *on* frames. The off frames are taken in a mode of operation where no signal is expected. For each frame f, the sample contains three observables: t_f given by the difference of the signal-pixel value and the average of the neighborhood pixels (Eq. (5.19)), the number of valid pixels in the neighborhood, $N_{\mathrm{valid},f}$, and an efficiency q_f that contains the performance of the experimental setup while the frame was taken (e.g. quantum efficiency, power build-up of the laser cavities). The efficiency of the off frames is implicitly zero. Hence, a measurement is given by two sets,

$$x_{\mathrm{on}} = \{(t_1, N_{\mathrm{valid},1}, q_1), \ldots, (t_n, N_{\mathrm{valid},n}, q_n)\} \qquad \text{(on frames)},$$

and

$$x_{\mathrm{off}} = \{(t_{n+1}, N_{\mathrm{valid},n+1}), \ldots, (t_{n+m}, N_{\mathrm{valid},n+m})\} \qquad \text{(off frames)}.$$

To include the efficiency, λ_{sig} is replaced by $q_i \, \lambda_{\mathrm{sig}}$ in Eq. (5.20),

$$t_i \sim \mathrm{Poi}(q_i \, \lambda_{\mathrm{sig}}) \oplus \mathcal{N}\left(\mu, \sigma_{\mathrm{B}} \left[1 + 1/N_{\mathrm{valid},i}\right]^{1/2}\right) \; .$$

The likelihood for a measurement $(x_{\text{on}}, x_{\text{off}})$ is then given by

$$\begin{aligned}\mathcal{L}(\lambda_{\text{sig}}, \mu, \sigma_{\text{B}}; x_{\text{on}}, x_{\text{off}}) &= \prod_{i=1}^{n+m} f(t_i; q_i\lambda_{\text{sig}}, \mu, \sigma_{\text{B}}\sqrt{1+1/N_{\text{valid},i}}) \\ &= (2\pi\sigma_{\text{B}})^{-(n+m)/2}\, e^{-\lambda_{\text{sig}}Q} \prod_{a=1}^{n+m}\left(1+\frac{1}{N_{\text{valid},a}}\right)^{-1/2} \\ &\quad \cdot \prod_{b=1}^{n}\sum_{k=0}^{\infty}\frac{(q_b\lambda_{\text{sig}})^k}{k!}\exp\left(-\frac{(t_b-k-\mu)^2}{2\sigma_{\text{B}}^2(1+1/N_{\text{valid},b})}\right) \\ &\quad \cdot \prod_{c=n+1}^{n+m}\exp\left(-\frac{(t_c-\mu)^2}{2\sigma_{\text{B}}^2(1+1/N_{\text{valid},c})}\right)\,,\end{aligned} \tag{5.26}$$

with $Q = \sum_{i=1}^{n} q_i$.

Given a measurement $(x_{\text{on}}, x_{\text{off}})$, the confidence interval for λ_{sig} is then constructed using the hybrid method described above. The parameters maximizing the likelihood function,

$$\begin{aligned}(\hat{\hat{\mu}}, \hat{\hat{\sigma}}_{\text{B}}) &= \arg\max_{\mu,\sigma_{\text{B}}} \mathcal{L}(\lambda_{\text{sig}}, \mu, \sigma_{\text{B}}; x_{\text{on}}, x_{\text{off}}) \\ (\hat{\lambda}_{\text{sig}}, \hat{\mu}, \hat{\sigma}_{\text{B}}) &= \arg\max_{\lambda_{\text{sig}},\mu,\sigma_{\text{B}}} \mathcal{L}(\lambda_{\text{sig}}, \mu, \sigma_{\text{B}}; x_{\text{on}}, x_{\text{off}})\,,\end{aligned}$$

are given by systems of non-linear equations. Hence, numerical methods are used to find them.

The critical value $c_\alpha^*(\lambda_{\text{sig}}, x_{\text{on}}, x_{\text{off}})$ is determined using toy Monte-Carlo (MC) methods. In each MC iteration, a toy measurement, $(x'_{\text{on}}, x'_{\text{off}})$ is sampled from

$$f\left(t'_i; q_i\lambda_{\text{sig}}, \hat{\mu}(\lambda_{\text{sig}}, x_{\text{on}}, x_{\text{off}}), \hat{\sigma}_{\text{B}}(\lambda_{\text{sig}}, x_{\text{on}}, x_{\text{off}})\cdot\sqrt{1+1/N_{\text{valid},i}}\right)\,,$$

with $i = 1, \ldots, n+m$, and the associated likelihood ratio,

$$\Lambda'(\lambda_{\text{sig}}; x'_{\text{on}}, x'_{\text{off}}) = \frac{\mathcal{L}\left(\lambda_{\text{sig}}, \hat{\hat{\mu}}(\lambda_{\text{sig}}, x'_{\text{on}}, x'_{\text{off}}), \hat{\hat{\sigma}}_{\text{B}}(\lambda_{\text{sig}}, x'_{\text{on}}, x'_{\text{off}}); x'_{\text{on}}, x'_{\text{off}}\right)}{\mathcal{L}\left(\hat{\lambda}_{\text{sig}}, \hat{\mu}(x'_{\text{on}}, x'_{\text{off}}), \hat{\sigma}_{\text{B}}(x'_{\text{on}}, x'_{\text{off}}); x'_{\text{on}}, x'_{\text{off}}\right)}\,,$$

is calculated. c_α^* is then given by the α-quantile of the toy-MC sample $\{\Lambda'_a\}$,

$$\frac{\#\left\{\Lambda'_a \geq c_\alpha^* : a = 1, \ldots, N_{\text{MC}}\right\}}{N_{\text{MC}}} \geq 1-\alpha\,,$$

where N_{MC} is the size of the toy-MC sample and $\#\{\ldots\}$ measures the size of a set. To ensure the above (in)equality, a "conservative" quantile estimate, Q_α^{cons}, is used,

$$c_\alpha^* = Q_\alpha^{\text{cons}}(\{\Lambda'_a\})\,,$$

that ensures

$$\frac{\#\left\{s_a < Q_\alpha^{\text{cons}}(S)\right\}}{N} \leq \alpha$$

for some sample $S = \{s_1, \ldots, s_N\}$.

A bisection algorithm is used to find the endpoints of the confidence interval. The algorithm is implemented in Python [195] using the Numpy [196] and SciPy [197] libraries. Time-critical code, namely the numerical evaluation of the convolving sums in Eq. (5.26), is written in Cython [198] and makes use of the GNU Scientific Library [199] to calculate the Taylor factor, $x^k/k!$, and the exponential.

5.3.3 Performance

To test the performance of the algorithm developed in the previous section, parameters are chosen which have values that

(i) are expected for the CCD operation in ALPS-II or serve for comparison with ALPS-I,

or

(ii) define special cases, e.g. a small/large number of measurements.

To calculate the expected background uncertainty, σ_B, a value of $\sigma_\mathrm{RO} = 4.18\,\mathrm{e}^-$, and a dark charge rate of $R_\mathrm{DC} = 7.52 \times 10^{-4}\,\mathrm{e}^-/(\mathrm{px\,s})$ are assumed. These values are in the range of the observed values (cf. Tab. 5.6). The background uncertainty is calculated as

$$\sigma_\mathrm{B} = \sqrt{\sigma_\mathrm{RO}^2 + R_\mathrm{DC}\, t_\mathrm{exp}}\,.$$

A sample consisting of $T_\mathrm{on} = 27\,\mathrm{h}$ of on-mode data and $T_\mathrm{off} = 100\,\mathrm{h}$ of off-mode data is assumed. This corresponds to the largest sample in ALPS-I [51]. The tested parameter values are listed in the first six columns of Tab. 5.8. The tested CLs are those that are commonly used when specifying upper limits: 90, 95 and 99 %.

The first three groups of results correspond to parameter values that resemble the largest-statistic sample of ALPS-I and values expected for ALPS-II with 1 and 2 h exposure time, respectively. In ALPS-I, the signal was contained in a 3×3 binned logical pixel. Accordingly, the background uncertainty is given by

$$\sigma_\mathrm{B}^\mathrm{ALPS\text{-}I} = \sqrt{\sigma_\mathrm{RO}^2 + 9R_\mathrm{DC}\, t_\mathrm{exp}}\,.$$

For ALPS-II, it is expected that the signal can be focussed to a single pixel. Hence, σ_B is larger for ALPS-I compared to ALPS-II with 1 h exposure times. The expectation value of the signal, $\lambda_\mathrm{sig}^\mathrm{true}$, is set to zero. This allows to calculate the sensitivity (see below). The efficiency factor, q, is set to the quantum efficiency of the PIXIS CCD for green (ALPS-I) or infra-red (ALPS-II) light. The fourth set of parameters tests the performance with increased sample sizes n and m and arbitrary values for the other parameters. The fifth and sixth set have reduced sample sizes where the on-sample size of the sixth set is exceptionally low. The last five groups are used to compare the scaling of the sensitivity when changing the experimental running time or the efficiency with the expectation. This is discussed below.

Coverage

To test the coverage for given parameter values, toy measurements are sampled M times. The hybrid confidence interval was calculated for each of these measurements and the coverage of the interval was tested,

$$\lambda_{\mathrm{sig},1}(x_{\mathrm{toy}}) \leq \lambda_{\mathrm{sig}}^{\mathrm{true}} \leq \lambda_{\mathrm{sig},2}(x_{\mathrm{toy}}) \ ,$$

with the known true parameter value $\lambda_{\mathrm{sig}}^{\mathrm{true}}$. Hence, the observed CL is given by

$$\mathrm{CL}_{\mathrm{obs}} = \frac{\#\{\text{confidence interval covered } \lambda_{\mathrm{sig}}^{\mathrm{true}}\}}{M} \ .$$

For a target CL of $1-\alpha$ the expected 1σ statistical uncertainty due to the limited MC sampling is approximately given by the standard deviation of the binomial distribution,

$$\Delta\mathrm{CL} \simeq \sqrt{\frac{\alpha(1-\alpha)}{M}} \ .$$

Tab. 5.8 gives the results of the tests performed. For almost all tested parameters, the observed CL shows mild overcoverage. Taking into account the uncertainty ΔCL, the observed undercoverage is in good agreement with the targeted CL. Thus, it is concluded that the developed algorithm yields proper confidence intervals.

Comparison to ALPS-I

In ALPS-I, a simplified approach was used. The same data reduction was performed. But instead of the full likelihood, the averages of the neighborhood-subtracted signal pixel values were calculated,

$$\bar{t}_{\mathrm{on}} = \frac{1}{n}\sum_{i=1}^{n} t_i \ , \qquad \bar{t}_{\mathrm{off}} = \frac{1}{m}\sum_{i=n+1}^{n+m} t_i \ ,$$

and their difference,

$$d = \bar{t}_{\mathrm{on}} - \bar{t}_{\mathrm{off}} \ ,$$

was used as test statistic. Its distribution was assumed to be Gaussian,

$$d \sim \mathcal{N}(\lambda_{\mathrm{sig}}, \sigma_{\mathrm{B}}\sqrt{1/n + 1/m}) \ .$$

The variance was estimated from the "off" data,

$$\sigma_{\mathrm{B}}^2 = \frac{1}{m-1}\sum_{i=n+1}^{n+m} (t_i - \bar{t}_{\mathrm{off}})^2 \ .$$

The coverage of this method is tested as well. The observed coverages are listed in Tab. 5.9 for different values of λ_{sig} and σ_{B}. The last row gives the averages of the observed CLs. For all target CLs the average observed CL is slightly too low. Hence, the confidence intervals given by this method undercover. In other tests, the sample sizes, n, m, were decreased and the observed undercoverage worsened. Therefore, this undercoverage is probably caused by ignoring the uncertainty of the nuisance parameter, σ_{B}. A solution for this could be to use Student's t-distribution instead of a Gaussian. This was, however, not tested, because using the full likelihood is more flexible. For example, it can be adapted to include frames taken with different exposure times, which might be necessary if the periods of stable lock of the optical cavities is short (see Sec. 5.4).

experimental parameters							CL [%]			
n	m	$\lambda_{\text{sig}}^{\text{true}}$	q	μ	σ_{B}	M	$1-\alpha$	ΔCL	CL_{obs}	sens.
[a]27	100	0.0	0.95	-3.0	6.46	500	90	1.3	91.4	2.568
						999	95	0.7	95.3	2.787
						500	99	0.4	99.2	3.995
[b]27	100	0.0	0.012	-3.0	4.48	485	90	1.3	90.9	131.0
						996	95	0.7	96.4	162.2
						500	99	0.4	100.0	220.6
[c]13	50	0.0	0.012	-3.0	4.77	500	90	1.3	90.6	210.1
						999	95	0.7	94.5	248.7
						500	99	0.4	98.8	340.0
30	70	1.2	1	-3.0	4.35	486	90	1.4	90.3	–
						500	95	1.0	96.0	–
						100	99	1.0	98.0	–
10	20	10	1	5.0	3.00	200	90	2.1	89.5	–
						200	95	1.5	97.0	–
						50	99	1.4	100.0	–
3	20	10	1	5.0	3.00	500	90	1.3	92.0	–
						500	95	1.0	95.6	–
						100	99	1.0	100.0	–
[d]20	10	0	1	-3.0	4.35	500	90	1.3	92.6	2.81
						999	95	0.7	95.7	3.41
						500	99	0.4	99.6	4.71
[d]20	10	0	0.6	-3.0	4.35	500	95	1.0	94.6	5.75
[d]20	10	0	0.2	-3.0	4.35	500	90	1.3	92.6	13.6
						999	95	0.7	94.4	17.4
						500	99	0.4	98.8	23.7
[d]40	20	0	1	-3.0	4.35	500	95	1.0	95.8	2.37
[d]100	50	0	1	-3.0	4.35	496	90	1.3	89.7	1.34
						999	95	0.7	95.5	1.52
						500	99	0.4	99.6	1.98

[a]Parameters for largest sample of ALPS-I [51].
[b]Parameters for ALPS-II with 1 h exposures.
[c]Parameters for ALPS-II with 2 h exposures.
[d]Used for calculation of the sensitivity scaling. See Fig. 5.25.

Table 5.8: Results of the coverage tests and sensitivity calculation for λ_{sig}. Listed are the experimental parameters, the number of toy-MC experiments, M, the target CL, $1-\alpha$, the expected statistical uncertainty, ΔCL, and the observed CL. The last column lists the sensitivity where applicable. For more information refer to the text.

parameters		confidence level [%]				
λ_{sig}	σ_{B}	50.00	68.32	90.00	95.00	99.00
0.0	0.5	51.00	71.80	90.90	93.40	98.30
	1.0	52.40	66.30	91.10	95.10	98.70
	2.0	48.40	68.20	90.30	93.90	98.60
	3.0	48.40	70.30	90.00	95.40	99.00
	4.0	50.50	68.70	90.10	94.40	99.40
	5.0	52.20	65.40	90.70	95.60	99.30
0.1	0.5	49.90	69.50	89.30	94.40	99.00
	1.0	49.50	68.40	88.10	93.70	98.60
	2.0	49.50	67.90	89.70	93.90	99.20
	3.0	49.00	67.10	89.40	93.90	98.90
	4.0	49.90	67.30	89.60	95.90	99.10
	5.0	48.20	65.60	90.10	94.20	98.70
0.2	0.5	47.30	68.00	88.60	93.40	98.20
	1.0	46.70	67.90	88.50	93.80	98.60
	2.0	50.40	66.20	88.70	94.70	99.00
	3.0	47.80	68.50	88.60	94.90	98.90
	4.0	48.80	68.00	91.00	94.20	98.90
	5.0	47.80	68.90	89.90	94.60	97.90
0.3	0.5	47.80	68.80	88.80	94.60	98.30
	1.0	51.00	67.50	89.90	95.10	98.70
	2.0	50.20	67.90	88.70	94.60	97.80
	3.0	52.20	68.70	89.70	95.90	99.30
	4.0	49.30	65.80	89.10	94.60	99.10
	5.0	50.50	67.30	89.50	93.70	99.10
0.4	0.5	49.90	63.70	90.00	94.00	98.50
	1.0	49.70	67.60	88.80	95.40	98.40
	2.0	48.90	64.10	87.60	93.60	99.30
	3.0	49.40	67.90	89.40	93.90	98.90
	4.0	47.60	67.40	88.60	94.70	99.10
	5.0	50.30	66.80	89.20	94.60	98.50
0.5	0.5	46.80	68.30	88.40	93.20	97.90
	1.0	48.90	67.40	89.30	95.00	98.30
	2.0	49.20	67.20	87.40	94.40	98.60
	3.0	49.20	69.40	87.90	95.20	98.70
	4.0	50.90	68.30	89.50	94.00	98.50
	5.0	47.90	68.20	89.60	94.80	98.40
1.0	0.5	49.90	67.30	89.40	92.90	98.60
	1.0	50.20	66.00	88.60	94.10	98.20
	2.0	48.70	68.90	88.30	95.40	98.40
	3.0	48.80	66.10	89.50	94.90	99.10
	4.0	51.20	66.00	89.80	94.50	98.50
	5.0	48.30	67.40	88.10	94.30	98.20
1.5	0.5	48.00	69.70	90.00	94.20	99.00
	1.0	50.70	65.40	90.50	92.60	98.60
	2.0	48.90	67.80	88.90	95.60	98.20
	3.0	48.50	69.80	89.30	94.20	98.20
	4.0	45.90	65.70	89.30	95.10	98.40
	5.0	50.20	66.50	86.60	94.90	98.40
2.0	0.5	50.30	68.10	89.60	93.60	98.60
	1.0	48.30	68.90	87.90	94.70	99.30
	2.0	48.60	68.60	88.90	94.50	98.80
	3.0	46.90	70.40	90.40	94.10	98.30
	4.0	46.70	64.20	90.10	95.10	98.70
	5.0	50.30	65.60	89.10	95.00	99.00
	average	**49.22**	**67.57**	**89.26**	**94.45**	**98.67**

Table 5.9: Coverage of ALPS-I confidence intervals. Listed is the observed coverage for different target CLs given in the header. For the tests $n = 27$ and $m = 100$ was assumed. For each $(\lambda_{\text{sig}}, \sigma_{\text{B}})$ pair $M = 1000$ toy experiments were conducted. The last row lists the average of each column.

Sensitivity

The sensitivity is defined as the average upper limit observed in toy MC experiments where the signal is set to zero, i.e. $\lambda_{\text{sig}}^{\text{true}} = 0$ [136]. This is the null hypothesis. Thus, the sensitivity specifies the expected upper limit if the null hypothesis is true. Therefore, the sensitivity, S_α, for a CL $= 1 - \alpha$, can be interpreted as: "We expect that the experiment will exclude the parameter space $\lambda_{\text{sig}} \geq S_\alpha$ with confidence $1 - \alpha$ if the null hypothesis is true." Comparing the sensitivity of different experimental setups allows to find an optimal choice, i.e. the experiment with the smallest sensitivity.

The last column of Tab. 5.8 lists the sensitivity for the parameter sets with $\lambda_{\text{sig}}^{\text{true}} = 0$. Because the efficiency factor, q, was chosen to include the quantum efficiency of the CCD for green (ALPS-I) or infra-red (ALPS-II) light, the listed sensitivities give the expected upper limits on the average number of photons that reached the CCD during a single on-mode exposure. Hence, they translate in the sensitivity for the rate of reconverted photons by division by the exposure time of a single CCD frame. The 95 %-CL sensitivities on the photon rate are listed in the first three rows of Tab. 5.10 and will be discussed below.

The expected scaling of the sensitivity, S, with the total experimental run time, T, is $S \propto T^{-1/2}$ and inversely with the efficiency, $S \propto q^{-1}$. To describe the dependence of the on- and off-mode sample sizes, n and m, on the run time,

$$n = \frac{T}{T_0}\, n_0 \qquad \text{and} \qquad m = \frac{T}{T_0}\, m_0$$

are used. The scaling of the 95 %-CL sensitivities of last five groups in Tab. 5.8 is calculated. The results are compared to the expected scaling in Fig. 5.25 and show a good agreement. Hence, the sensitivity values in Tab. 5.8 can be used to calculate the sensitivity of the CCD for quantum efficiencies, η, other than $\eta_0 = 1.2\,\%$ by multiplying with η_0/η.

EMCCD and TES

For an ideal EMCCD in binary operation (see Sec. 5.1.2) the experiment reduces to a counting experiment. If the exposure time of the frames is sufficiently low, the dark count rate per frame is low enough such that no signal is lost due to coincidences. For simplification, it is assumed that the uncertainty of background can be neglected. This allows to use the original unified method [136]. Assuming a dark count rate comparable to the PIXIS CCD ($8 \times 10^{-4}\,\text{e}^-/(\text{px}\,\text{s})$, cf. Tab. 5.1), the expected number of dark counts is $b_{\text{exp}} = 77.76\,\text{e}^-/\text{px}$ for a total running time of 27 h. Using unified confidence intervals, a sensitivity of $19.64\,\text{e}^-/\text{px}$ is found at 95 % CL, corresponding to a rate of $2.02 \times 10^{-4}\,\text{e}^-/(\text{s}\,\text{px})$. This result has to be divided by the quantum efficiency to get the sensitivity for the incident photon rate,

$$2.53 \times 10^{-4}\,\gamma/(\text{s}\,\text{px}) \quad (\eta = 80\,\%)\,, \qquad 168 \times 10^{-4}\,\gamma/(\text{s}\,\text{px}) \quad (\eta = 1.2\,\%)\,.$$

The same method can be used to derive the sensitivity for the TES. Using the design values from the technical design report [160] for the efficiency and dark count rate (cf. Sec. 4.6.1), one finds $b_{\text{exp}} = 9.72 \times 10^{-2}\,\gamma$ and

$$2.87 \times 10^{-6}\,\gamma/\text{s} \quad (\eta = 75\,\%, R_{\text{DC}} = 10^{-6}\,\text{s}^{-1})\,.$$

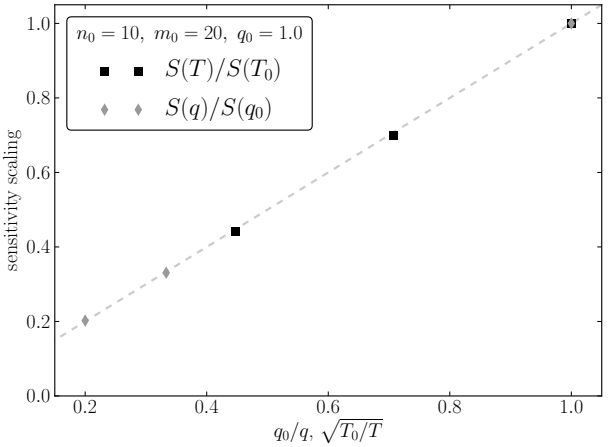

Figure 5.25: Scaling of the sensitivity (CL = 95 %). The scaling with the total run time, T, (black squares) and with the efficiency, q, (gray diamonds) is shown. The dashed line shows the expectation. The experimental parameters are $\lambda_{\text{sig}} = 0$, $\mu = -3.0$, and $\sigma_{\text{B}} = 4.35$ (cf. Tab. 5.8).

Tab. 5.10 compares these results to the sensitivity of the PIXIS CCD, which will be discussed below.

5.4 Summary

In this study, the PIXIS CCD has been examined. The measured quantum efficiency of $\eta = 1.208 \pm 0.002(\text{stat}) \pm 0.079(\text{syst})$ at a temperature of $-70\,^{\circ}\text{C}$ for 1066.7 nm is necessary to interpret measurements with the PIXIS CCD in ALPS-II. Furthermore, even if the CCD is not used as detector in ALPS-II, it is used extensively during the preparation and commissioning of ALPS-II, e.g. as a photo-detector for 1064 nm that is much more sensitive than ordinary power meters. For this, knowledge of the quantum efficiency is necessary as well.

It was found that the fixed pattern noise (FPN) (Fig. 5.16), the associated read-out noise (Fig. 5.18) and the dark count rate (Fig. 5.21) depend on the pixel position on the CCD chip. The spatial variation of the FPN is caused by clock-induced charges (CIC). Near the read-out of the chip, the observed read-out noise including effects of the CIC is below the specified value. For pixels far away from the read-out, this value is exceeded. An error in the firmware of the camera control electronics leads to a non-uniform thermal load. This non-uniformity causes a spatial variation of the dark count rate. Except for pixels near the read-out structure, the observed dark count rate is of the order of the vendor-specified value or below. This can be used to find a position with the lowest background variance to achieve the best performance of the camera. The gain of the ADC ($G = (1.041 \pm 0.025)\,\text{e}^{-}/\text{ADU}$) was found to be compatible with the value specified by the vendor. Long-time exposures showed that the camera is limited to exposure times below 139 min.

	sensitivity	
detector	total [cnt]	rate [γ/s]
CCD ALPS-I	2.8	7.7×10^{-4}
CCD ALPS-II 1 h	162.2	4.5×10^{-2}
CCD ALPS-II 2 h	248.7	3.5×10^{-2}
EMCCD ($\eta = 1.2\,\%$)	–	1.7×10^{-2}
TES	–	2.9×10^{-6}

Table 5.10: 95 %-CL sensitivity (photon counts and rate) of different detectors for a on- and off-mode run times similar to ALPS-I ($T_{\text{on}} = 27\,\text{h}$, $T_{\text{off}} = 100\,\text{h}$). The numerical values include the effect of the different quantum efficiencies. The first three rows correspond to the first three groups in Tab. 5.8, namely the PIXIS CCD with ALPS-I parameters and with ALPS-II parameters assuming 1 h and 2 h exposure times. For comparison, the sensitivities for an EMCCD with the quantum efficiency of the PIXIS CCD at 1066.7 nm and for a TES assuming the design values of the technical design report [160] are listed. Refer to the text for more information.

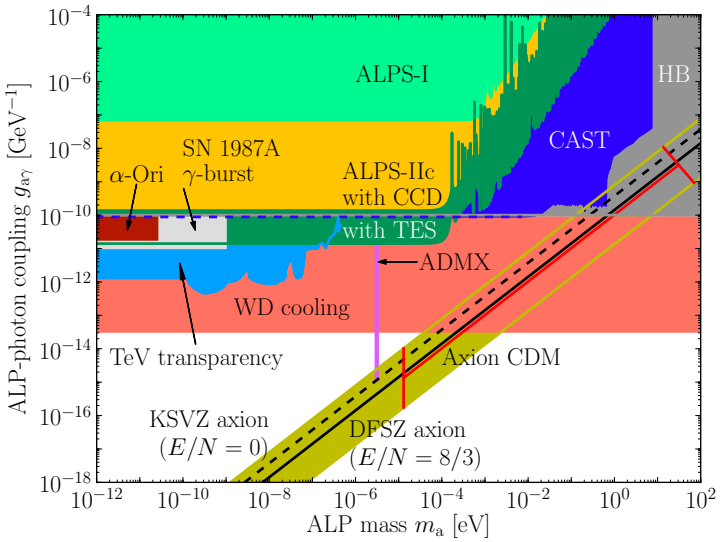

Figure 5.26: ALPS-IIc sensitivity with the PIXIS CCD (95 % CL). Shown is the sensitivity of ALPS-IIc with the PIXIS CCD an 1 h exposures (orange, cf. Tab. 5.10) and with the TES (dark green). Additionally, the same constraints and hints are shown as in Fig. 2.3.

To prepare a possible deployment of the PIXIS CCD as a detector in ALPS-II, a new analysis method for the CCD data has been developed. The proposed algorithm takes the existing nuisance parameters into account. The numerical implementation was tested and it was found that the calculated confidence intervals indeed have coverage, while a slight undercoverage was found for the method used in ALPS-I.

The sensitivity of the CCD was calculated for benchmark scenarios with an experimental run time similar to ALPS-I and values of the quantum efficiency and background noise as estimated in this chapter. These were compared to the sensitivities of an EMCCD (assuming the same quantum efficiency as the PIXIS CCD) and a TES (using the design values of the ALPS-II technical design report [160]) in Tab. 5.10. Compared to ALPS-I, the sensitivity on the photon rate in ALPS-II is worse by two orders of magnitude. The EMCCD is only slightly better than the PIXIS. This deterioration is caused by the much smaller quantum efficiency of silicon-based CCDs at 1064 nm. However, using specialized infra-red CCDs, e.g. based on InGaAs, offers no solution, because their dark count rate is six orders of magnitude larger [200].

The TES has the best sensitivity of all studied options. It is four orders of magnitude below the sensitivity of the PIXIS CCD for ALPS-II. Additionally, the TES can be operated more flexible than the PIXIS CCD, because it is a true single-photon detector. Hence, its mode of operation can be easily adapted if the periods of stable lock of the optical cavities in ALPS-II happen to be short. However, because the sensitivity on the ALP-photon coupling, $g_{a\gamma}$, or the HP kinetic mixing, χ, is proportional to the fourth root of photon-rate sensitivity (cf. Eqs. (4.6) and (4.7)), the sensitivity of ALPS-II will worsen by one order of magnitude if ALPS-II used the PIXIS CCD instead of the TES. This can be seen in Fig. 5.26 where the sensitivity on the ALP parameters of ALPS-IIc with a TES detector is compared to the sensitivity with the PIXIS CCD as detector. In this case, ALPS-II will reach a similar sensitivity as CAST.

Chapter 6

Conclusion

Many extensions of the Standard Model of Particle Physics (SM) predict weakly interacting slim particles (WISPs). The solution of the strong CP-problem by an axial symmetry proposed by Peccei and Quinn in 1977 predicts the axion, which is very weakly coupled to SM particles and has a very low mass and, therefore, is considered a WISP. Embedding the SM in string theories predicts the existence of a large number of axion-like particles (ALPs) (axiverse), which couple to photons via the process $a \rightarrow \gamma\gamma$. Additionally, unbroken hidden U(1) symmetries may exist with associated hidden photons (HPs). If any of these WISP candidates exists, it may influence cosmology and stellar evolution. Therefore, analyses of cosmological and astrophysical observables can be used to detect WISPs or constrain the WISP parameter space. Observations of the white dwarf luminosity function and of the transparency of the Universe to ultra-high energy gamma rays can be explained in the presence of an ALP and predict regions in parameter space. Both predicted regions overlap.

One consequence of the existence of an ALP is that photons can convert to ALPs in a stellar core. Because of their tiny coupling to SM particles, these ALPs, in contrast to photons, escape the stellar core. α-Ori (Betelgeuse) is a red supergiant with an atmosphere that does not emit X-rays according to the SM. However, in the presence of ALPs, a part of the ALP flux from its core should reconvert to photons during the travel through the galactic magnetic field (GMF) from α-Ori to Earth. These photons have the same X-ray energies as the initial photons in the stellar core. Thus, α-Ori could be visible in the X-ray regime.

In Chap. 3 of this thesis, the evolution of a star similar to α-Ori was modelled using EZ-Web. The evolution of a $17.5\,M_{\odot}$ star at an age of 11.5 Myr showed good agreement with observed properties of α-Ori. The modelled stellar profile was used to estimate the ALP production rate in the core of α-Ori. A lower limit on the field strength of the regular component of the GMF perpendicular to the line of sight to α-Ori was used to calculate the probability for ALP-to-photon reconversion. Plasma effects of the interstellar medium (ISM) were taken into account. For this, the average value of the free electron density along the line of sight was calculated using the NE2001 model. The expected X-ray spectrum at Earth was calculated for ALP masses where the strong-mixing assumption is valid ($m_{\mathrm{a}} \lesssim 2.6 \times 10^{-11}$ eV). From this spectrum, the expected count rates with the HRC-I, HRC-S and ACIS-I instruments of the Chandra X-ray Observatory

satellite were estimated using the PIMMS program.

α-Ori was observed regularly by Chandra from 2001 to 2007. From these observations, the 95 % confidence level (CL) upper limits on the count rate have been calculated. Comparison with the expected count rates allows to constrain the ALP-photon coupling to $g_{a\gamma} \lesssim 1.8 \times 10^{-11}\,\mathrm{GeV}^{-1}$ for $m_a \lesssim 2.6 \times 10^{-11}\,\mathrm{eV}$. This result is compatible with a similar study [113]. In addition, the expected count rate expected for a 10 ks observation with the NuSTAR satellite, launched in 2012, was calculated. The 95 % CL sensitivity of NuSTAR on $g_{a\gamma}$ ($g_{0.95}^{\mathrm{NuSTAR}} = 0.46 \times 10^{-11}\,\mathrm{GeV}^{-1}$) is a factor four better than the result obtained with Chandra. Further improving this limit by using longer observations, X-ray observations of other red supergiants or observations made with different satellite observatories was found to be difficult.

Because of the assumptions on the stellar evolution of α-Ori and the properties of the ISM along the line of sight, the interpretation of the limits in terms of confidence level is model dependent. Laboratory based experiments can help to derive less model dependent limits – ideally surpassing them. ALPS-II is a light-shining-through-a-wall type (LSW) experiment. In its final stage it will use 2×10 superconducting HERA dipole magnets to provide the magnetic field necessary for photon-ALP oscillations. LSW experiments exploit that WISPs can pass barriers that are opaque for SM particles. Via the process $\gamma \to \mathrm{wisp} \to \gamma$, photons can effectively shine through the barrier (wall).

It is planned to use a highly efficient, very low-noise TES detector in ALPS-II. Together with improvements in the other components of the experiment, this will increase the sensitivity on the ALP parameters by three orders of magnitude better compared to the current best limit from LSW, which is set by its predecessor experiment ALPS-I.

The PIXIS 1024B CCD that was used as detector in ALPS-I is foreseen as backup detector in ALPS-II. Additionally, it will be used for the characterization of the transition edge sensor (TES) and the commissioning of ALPS-II. Therefore, it has to be understood in all details. The results are presented in Chap. 5 of this thesis. The characterization includes a measurement of the quantum efficiency for a wavelength of 1066.7 nm near the wavelength used in ALPS-II (1064 nm). It was found to be $\eta = (1.208 \pm 0.002(\mathrm{stat}) \pm 0.079(\mathrm{syst}))\,\%$. Additionally, the fixed pattern noise (FPN) and the associated read-out noise was determined. It was found that clock-induced charges cause a spatial variation of the FPN and the read-out noise, which is higher for pixels located farther away from the read-out structure. Furthermore, the dark count rate due to thermally produced electron-hole pairs was precisely measured. It shows spatial variations, too. The highest dark count rate is found near the read-out structure. Discussion with the vendor indicate that components of camera control electronics are not properly switched off during an exposure. These active components cause a thermal load on the imaging area of the CCD which is the reason for this high dark count rate. In the remaining parts of the imaging area, the dark count rate is of the order of the value specified by the vendor ($8 \times 10^{-4}\,\mathrm{e}^-/(\mathrm{px\,s})$) or below this value. From the measured data, the gain has also been estimated and found to agree with the value specified by the vendor ($1.02\,\mathrm{e}^-/\mathrm{ADU}$).

In preparation of a possible installation of the PIXIS CCD as detector in ALPS-II, I developed and implemented an algorithm for the analysis. As an improvement over the analysis algorithm used in ALPS-I, the algorithm developed here takes into account the existing nuisance parameters. The hybrid

resampling method is used to construct an efficient algorithm avoiding explicitly integrating over the space of nuisance parameters. The coverage of the confidence intervals yielded by this algorithm have been tested for various numerical values of the relevant parameters. In all tests, the observed coverage agrees with the targeted confidence level or is slightly above. Hence, a mild overcoverage is found. The sensitivity of the CCD if used as detector in ALPS-II was calculated and compared with a TES and a EMCCD detector. The sensitivity on the incident photon rate of the CCD is four orders of magnitude worse than the forecasted sensitivity of the TES, which results in a sensitivity on the ALP-photon coupling decreased by one order of magnitude if the CCD is used. The different sensitivity is caused in equal parts by the large difference of the quantum efficiencies for 1064 nm light and the different dark count rates of the two detectors.

With its improved sensitivity, ALPS-II will probe a very interesting region of the ALP parameter space that is favoured by the hints from white dwarf cooling and TeV transparency. It will be able to confirm the limit derived from X-rays from α-Ori and, for small masses, it will improve the limits from CAST and horizontal branch stars. The chase for WISPs continues and ALPS-II is one of the most promising tools.

Appendix

A.1 Acronyms

ADC analog-to-digital converter

AIST National Institute of Advanced Industrial Science and Technology

ALPS Any-Light-Particle Search

ALP axion-like particle

AOM acousto-optical modulator

BBN Big Bang nucleosynthesis

CAST CERN Axion Solar Telescope

CCD charge-coupled device

CDM cold dark matter

CERN Conseil Européen pour la Recherche Nulcléaire

CIC clock-induced charges

CL confidence level

CMB cosmic microwave background

DESY Deutsches Elektronen Synchrotron

DE dark energy

DM dark matter

DWS differential wave-front sensing

EMCCD electron multiplying charge-coupled device

FPN fixed pattern noise

FWHM full width half maximum

GMF galactic magnetic field

HERA Hadron-Electron Ring Accelerator

HP hidden photon

ISM interstellar medium

LHC Large Hadron Collider
LSS large-scale structures
LSW light shining through a wall
MFO micro focus optic
MIS metal-insulator-semiconductor
MOPA master-oscillator power amplifier
MOSFET metal-oxide-semiconductor field effect transistor
ND neutral density filter
NEG non-evaporable getter
NIST National Institute of Standards and Technology
PC production cavity
PDF probability density function
PDH Pound-Drever-Hall scheme
PIMMS Portable, Interactive Multi-Mission Simulator
PMS pre-main-sequence star
PSF point-spread function
PZT piezo-electric transducer
QCD quantum chromo dynamics
QED quantum electro dynamics
QPD quadrant photo-diode
RGB red giant branch
RC regeneration cavity
ROI region of interest
RSG red supergiant
SCCD surface channel CCD
SGB subgiant branch
SHG second harmonic generation
SM Standard Model of Particle Physics
SQUID superconducting quantum interference device
TES transition edge sensor
WIMP weakly interacting massive particle
WISP weakly interacting slim particle
ZAMS zero-age main sequence

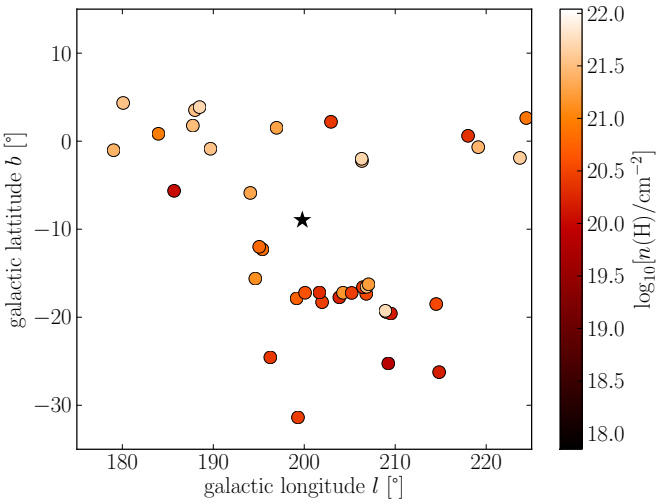

Figure A.1: Map of stars with valid $n(\mathrm{H})$ measurements around α-Ori. The $n(\mathrm{H})$ values are indicated by the color of the dots. α-Ori's position is marked by an asterisk.

A.2 Neutral-hydrogen Column Density for α-Ori

Gudennavar et al. [157] compiled a database of interstellar column densities based on absorption line data for 3008 stars. Fig. A.1 shows a subsample of stars listed in Tab. 2 of Gudennavar et al. [157] that are near α-Ori and have valid values for the neutral-hydrogen density, $n(\mathrm{H})$, and their distance, d. The neutral-hydrogen density along the line of sight to α-Ori was estimated by calculating the average of the ratio of $n(\mathrm{H})/d$,

$$\left\langle \frac{n(\mathrm{H})}{d} \right\rangle = \frac{1}{\sum\limits_{i:\delta_i<\Delta} 1} \sum_{i:\delta_i<\Delta} \frac{n(\mathrm{H})_i}{d_i} \,, \tag{A.1}$$

where i runs over all stars with an angular distance $\delta_i < \Delta$. Tab. A.1 lists $\langle n(\mathrm{H})/d \rangle$ for various values of Δ. The results in Tab. A.1 show a systematic trend with maximal $\langle n(\mathrm{H})/d \rangle$ for $\Delta \approx 30°$. This trend is caused by the substructure of the ISM, which is concentrated in the spiral arms within the galactic plane of the Milky Way (e.g. [115, Sec. 8.2]). Taking this into account and, hence, requiring $\Delta \lesssim 10°$ to keep the contribution of the galactic plane minimal, a rough estimate for $\langle n(\mathrm{H})/d \rangle$ along the line of sight to α-Ori of

$$\left\langle \frac{n(\mathrm{H})}{d} \right\rangle \approx 1.7 \times 10^{21}\,\mathrm{cm}^{-2}\,\mathrm{kpc}^{-1}$$

is reasonable. For a distance to α-Ori of $d = 197\,\mathrm{pc}$ [123], this corresponds to

$$n(\mathrm{H})_{\alpha\text{-Ori}} \approx 3.3 \times 10^{20}\,\mathrm{cm}^{-2} \,.$$

Δ [°]	Sample size	$\left\langle \frac{n(\mathrm{H})}{d} \right\rangle$ [$10^{21}\,\mathrm{cm}^{-2}\,\mathrm{kpc}^{-1}$]
8	3	1.67
10	13	1.64
12	19	2.65
15	25	3.58
20	32	3.96
25	39	4.10
30	45	5.19
60	76	4.07
90	138	2.82

Table A.1: Dependence of the mean of $n(\mathrm{H})/d$ on the maximal angular distance, Δ, of included stars. Listed are the maximal angular distance, the number of stars inside the acceptance region and the resulting average, $\langle n(\mathrm{H})/d \rangle$ (cf. Eq. (A.1)).

A.3 Equations of Stellar Evolution

The "Evolve ZAMS" code [116, 117] that was used in this work to model the interior of α-Ori is based on the code by Eggleton [118–121]. The equations of stellar evolution that need to be solved are [118, 119]

$$\frac{\mathrm{d}\log P}{\mathrm{d}m} = -\frac{G\,m}{4\pi\,r^4\,P} \tag{A.2}$$

$$\frac{\mathrm{d}\log T}{\mathrm{d}m} = \frac{\mathrm{d}\log P}{\mathrm{d}m} \cdot \nabla \tag{A.3}$$

$$\frac{\mathrm{d}\log r}{\mathrm{d}m} = \frac{1}{4\pi\,r^3\,\rho} \tag{A.4}$$

$$\frac{\mathrm{d}L}{\mathrm{d}m} = -\frac{\mathrm{D}u}{\mathrm{D}t} + \frac{P}{\rho^2}\frac{\mathrm{D}\rho}{\mathrm{D}t} - \epsilon_\nu + \epsilon_X \tag{A.5}$$

$$\frac{\mathrm{d}X}{\mathrm{d}m} = \xi \tag{A.6}$$

$$\frac{\mathrm{d}}{\mathrm{d}m}\sigma\xi = \frac{\mathrm{D}X}{\mathrm{D}t} + X\,R_X\ . \tag{A.7}$$

The mass $m(R) = \int_0^R 4\pi\,r^2\,\rho\,\mathrm{d}r$ is used as independent variable. P is the pressure, G the gravitational constant, r the radial coordinate, T the temperature, ∇ the logarithmic gradient of T against P, ρ the density, u the internal energy density, ϵ_ν the energy loss density due to neutrinos and ϵ_X the energy production rate due to nuclear burning of species X. The time derivatives $\mathrm{D}/\mathrm{D}t$ are taken at constant mass coordinate. X represents the mass fraction of species X and σ is the diffusion coefficient. The energy released by burning species X is given by

$$\epsilon_X = X\,R_X\,E_X\ ,$$

where R_X is the rate at which species X is burned and E_X the energy released by this reaction.

In principle, a pair of Eqs. (A.6) and (A.7), is necessary for each nuclear species X. But because typically one nuclear reaction dominates at each mass

coordinate, it is sufficient to have only one pair of equations and X representing the respective significant species [119].

Let s be the set of functions which describe the structure (Eqs. (A.2) to (A.5)) and c the set describing the composition (Eqs. (A.6) to (A.7)). For a fixed time-step Δt, Eqs. (A.2) to (A.7) can be approximated in an "explicit" fashion [119],

$$\Delta s = f[s, c]\,\Delta t\ , \qquad \Delta c = g[s, c]\,\Delta t\ ,$$

or in an "implicit" fashion,

$$\Delta s = f[s + \Delta s, c + \Delta c]\,\Delta t\ , \qquad \Delta c = g[s + \Delta s, c + \Delta c]\,\Delta t\ , \tag{A.8}$$

where f and g represent Eqs. (A.2) to (A.5) and Eqs. (A.6) to (A.7), respectively. The implicit method is used to find the Evolve ZAMS code.

The mesh points in terms of the mass coordinate are given by points which are evenly spaced in terms of

$$q \propto -0.02 \log P + 0.1X + \left(\frac{m}{M}\right)^{2/3}\ ,$$

where M is the total stellar mass [119]. This choice ensures that the mesh points are densely located in regions where the composition, X, or the pressure, P, change rapidly. During the evolution, the next stellar model is obtained by solving Eqs. (A.8) at the mesh points defined by the current model. The time-step, $\Delta t = 0.01 \min_X t_{\mathrm{nuc},X}$, is given by the nuclear time scales $t_{\mathrm{nuc},X} = E_X\, X\, M / L_X$ with L_X the luminosity due to burning species X except during phases of rapid core contraction [118].

A.4 Error Analysis for Quantum Efficiency Measurements

According to Eqs. (5.3), (5.4) and (5.6), the quantum efficiency is given by

$$\eta = \frac{\dot{N}_\mathrm{e}}{T\, P_\gamma / E_\gamma} = \frac{\dot{N}_\mathrm{e}\, R\, S\, E_\gamma}{\prod_i T_i \cdot (U_\mathrm{lc} - U_\mathrm{dark})}\ ,$$

with

$$T = \prod_i T_i = \prod_i \frac{U_i - U_\mathrm{dark}}{U_{i0} - U_\mathrm{dark}}\ ,$$

and where U_lc is the voltage measurement of the laser calibration, U_dark the voltage of a dedicated dark measurement. The product runs over the transmissions, T_i, of all used attenuators and filters and U_i (U_{i0}) are the voltage measurements with (without) attenuator (or filter).

Let $i(a)$ identify the set of transmissions used in quantum efficiency measurement a and assuming Gaussian error propagation, the uncertainty on the average of n measurements

$$\bar{\eta} = \frac{1}{n} \sum_{a=1}^{n} \eta^{(a)} = \frac{R\, S\, E_\gamma}{n\,(U_\mathrm{lc} - U_\mathrm{dark})} \sum_{a=1}^{n} \dot{N}_\mathrm{e}^{(a)} \prod_{i(a)} \underbrace{\frac{U_{i0} - U_\mathrm{dark}}{U_i - U_\mathrm{dark}}}_{=1/T_i} \tag{A.9}$$

is given by

$$\Delta\bar{\eta}^2 = \sum_{\mu,\nu} \frac{\partial\bar{\eta}}{\partial\mu} \frac{\partial\bar{\eta}}{\partial\nu} \operatorname{cov}(\mu,\nu) \,, \tag{A.10}$$

where μ and ν are the measured quantities and

$$\operatorname{cov}(\mu,\nu) = \Delta\mu\,\Delta\nu\,\rho_{\mu\nu}$$

their covariance with $\rho_{\mu\nu}$ their correlation coefficient.

To estimate both the statistical and systematic uncertainty, Eq. (A.10) is used. The statistical uncertainties are assumed to be uncorrelated,

$$\rho_{\mu\nu}^{(\mathrm{stat})} = 0 \,. \tag{A.11}$$

The systematic uncertainties of different voltage measurements U_α, U_β are considered to be either fully correlated if they were measured using the same range of the Amprobe AM-18 multi meter, or uncorrelated otherwise,

$$\rho_{U_\alpha U_\beta}^{(\mathrm{syst})} = \begin{cases} 1 & \text{if } U_\alpha \text{ and } U_\beta \text{ in the same multi-meter range} \\ 0 & \text{otherwise.} \end{cases} \tag{A.12}$$

For $\mu = R, U_{\mathrm{lc}}$, the derivatives $\partial\bar{\eta}/\partial\mu$ are trivial,

$$\frac{\partial\bar{\eta}}{\partial R} = \frac{\bar{\eta}}{R} \,, \qquad\qquad \frac{\partial\bar{\eta}}{\partial U_{\mathrm{lc}}} = -\frac{\bar{\eta}}{(U_{\mathrm{lc}} - U_{\mathrm{dark}})} \,.$$

For $\mu = U_{\mathrm{dark}}, U_i, U_{i0}$ the possible contributions to the products in Eq. (A.9) have to be considered. Using

$$\frac{\partial}{\partial U_{\mathrm{dark}}} \frac{1}{T^{(a)}} = \sum_{i(a)} \frac{T_i}{T^{(a)}} \frac{\partial}{\partial U_{\mathrm{dark}}} \frac{1}{T_i} = \sum_{i(a)} \frac{1}{T^{(a)}} \frac{1}{U_i - U_{\mathrm{dark}}} (1 - T_i) \,,$$

$$\frac{\partial}{\partial U_i} \frac{1}{T^{(a)}} = -\frac{1}{T^{(a)}} \frac{1}{U_{i0} - U_{\mathrm{dark}}} \,,$$

and

$$\frac{\partial}{\partial U_{i0}} \frac{1}{T^{(a)}} = \frac{T_i}{T^{(a)}} \frac{1}{U_{i0} - U_{\mathrm{dark}}}$$

we find

$$\frac{\partial\bar{\eta}}{\partial U_{\mathrm{dark}}} = \frac{\bar{\eta}}{(U_{\mathrm{lc}} - U_{\mathrm{dark}})} + \sum_{a=1}^{n} \dot{N}_{\mathrm{e}}^{(a)} \frac{1}{T^{(a)}} \sum_{i(a)} \frac{1}{U_i - U_{\mathrm{dark}}} (1 - T_i) \,,$$

$$\frac{\partial\bar{\eta}}{\partial U_i} = -\sum_{a(i)} \dot{N}_{\mathrm{e}}^{(a)} \frac{1}{T^{(a)}} \frac{1}{U_{i0} - U_{\mathrm{dark}}}$$

and

$$\frac{\partial\bar{\eta}}{\partial U_{i0}} = \sum_{a(i0)} \dot{N}_{\mathrm{e}}^{(a)} \frac{1}{T^{(a)}} \frac{T_i}{U_{i0} - U_{\mathrm{dark}}} \,,$$

to be used in Eq. (A.10) together with Eqs. (A.11) and (A.12) where $a(i)$ and $a(i0)$ represent all quantum efficiency measurements that use U_i and U_{i0} respectively.

Bibliography

[1] G. Aad et al. "Observation of a new particle in the search for the Standard Model Higgs boson with the ATLAS detector at the LHC." *Physics Letters B* 716 (2012), pp. 1–29. DOI: 10.1016/j.physletb.2012.08.020. arXiv:1207.7214 [hep-ex].

[2] S. Chatrchyan et al. "Observation of a new boson at a mass of 125 GeV with the CMS experiment at the LHC." *Physics Letters B* 716 (2012), pp. 30–61. DOI: 10.1016/j.physletb.2012.08.021. arXiv:1207.7235 [hep-ex].

[3] A. Riotto and M. Trodden. "Recent progress in baryogenesis." *Annual Review of Nuclear and Particle Science* 49 (1999), pp. 35–75. DOI: 10.1146/annurev.nucl.49.1.35. arXiv:hep-ph/9901362 [hep-ph].

[4] L. Bergström. "Nonbaryonic dark matter: observational evidence and detection methods." *Reports on Progress in Physics* 63 (2000), p. 793. DOI: 10.1088/0034-4885/63/5/2r3. arXiv:hep-ph/0002126 [hep-ph].

[5] G. Bertone, D. Hooper, and J. Silk. "Particle dark matter: evidence, candidates and constraints." *Physics Reports* 405.5-6 (2005), pp. 279 – 390. DOI: http://dx.doi.org/10.1016/j.physrep.2004.08.031. arXiv:hep-ph/0404175 [hep-ph]. URL: http://www.sciencedirect.com/science/article/pii/S0370157304003515.

[6] S. Weinberg. "The cosmological constant problem." *Reviews of Modern Physics* 61 (1 Jan. 1989), pp. 1–23. DOI: 10.1103/RevModPhys.61.1. URL: http://link.aps.org/doi/10.1103/RevModPhys.61.1.

[7] K. Bamba, S. Capozziello, S. Nojiri, and S. D. Odintsov. "Dark energy cosmology: the equivalent description via different theoretical models and cosmography tests." *Astrophysics and Space Science* 342.1 (2012), pp. 155–228. DOI: 10.1007/s10509-012-1181-8.

[8] M. Pospelov and A. Ritz. "Electric dipole moments as probes of new physics." *Annals of Physics* 318 (2005), pp. 119–169. DOI: 10.1016/j.aop.2005.04.002. arXiv:hep-ph/0504231 [hep-ph].

[9] M. Le Dall and A. Ritz. "CP-violation and electric dipole moments." *Hyperfine Interactions* 214.1-3 (2013), pp. 87–95. DOI: 10.1007/s10751-013-0801-1.

[10] R. D. Peccei and H. R. Quinn. "CP conservation in the presence of pseudoparticles." *Physical Review Letters* 38 (25 June 1977), pp. 1440–1443. DOI: 10.1103/PhysRevLett.38.1440.

[11] R. D. Peccei and H. R. Quinn. "Constraints imposed by CP conservation in the presence of pseudoparticles." *Physical Review D* 16 (6 Sept. 1977), pp. 1791–1797. DOI: 10.1103/PhysRevD.16.1791.

[12] S. Weinberg. "A new light boson?" *Physical Review Letters* 40 (4 Jan. 1978), pp. 223–226. DOI: 10.1103/PhysRevLett.40.223.

[13] F. Wilczek. "Problem of strong P and T invariance in the presence of instantons." *Physical Review Letters* 40 (5 Jan. 1978), pp. 279–282. DOI: 10.1103/PhysRevLett.40.279.

[14] B. Povh, K. Rith, C. Scholz, and F. Zetsche. *Particles and Nuclei*. 5th ed. Springer Berlin Heidelberg, 2006.

[15] C. Wu et al. "Experimental test of parity conservation in beta decay." *Physical Review* 105 (1957), pp. 1413–1414. DOI: 10.1103/PhysRev.105.1413.

[16] J. H. Christenson, J. W. Cronin, V. L. Fitch, and R. Turlay. "Evidence for the 2π decay of the K_2^0 meson." *Physical Review Letters* 13 (4 July 1964), pp. 138–140. DOI: 10.1103/PhysRevLett.13.138.

[17] C. Geweniger et al. "A new determination of the $\mathrm{K}^0 \to \pi^+\pi^-$ decay parameters." *Physics Letters* 48B.5 (Mar. 1974), p. 487. DOI: 10.1016/0370-2693(74)90385-2.

[18] D. H. Perkins. *Introduction to High Energy Physics*. 3rd ed. Addison-Wesley, 1986.

[19] E. Abouzaid et al. "Precise measurements of direct CP violation, CPT symmetry, and other parameters in the neutral kaon system." *Physical Review D* 83 (9 May 2011), p. 092001. DOI: 10.1103/PhysRevD.83.092001.

[20] B. Aubert et al. "Direct CP violating asymmetry in $B^0 \to K^+\pi^-$ decays." *Physical Review Letters* 93 (13 Sept. 2004), p. 131801. DOI: 10.1103/PhysRevLett.93.131801.

[21] R. Aaij et al. "Evidence for CP violation in time-integrated $D^0 \to h^-h^+$ decay rates." *Physical Review Letters* 108 (11 Mar. 2012), p. 111602. DOI: 10.1103/PhysRevLett.108.111602.

[22] S. Weinberg. *The Quantum Theory of Fields*. Vol. II Modern Applications. Cambridge University Press, 2005.

[23] R. D. Peccei. "The strong CP problem and axions." *Lecture Notes in Physics* 741 (2008), pp. 3–17. DOI: 10.1007/978-3-540-73518-2_1. arXiv:hep-ph/0607268 [hep-ph].

[24] S. Durr et al. "Lattice QCD at the physical point: light quark masses." *Physics Letters B* 701 (2011), pp. 265–268. DOI: 10.1016/j.physletb.2011.05.053. arXiv:1011.2403 [hep-lat].

[25] F. A. Wilczek. *Asymptotic Freedom: From Paradox to Paradigm*. Nobel Lecture. 2004. URL: http://www.nobelprize.org/nobel_prizes/physics/laureates/2004/wilczek-lecture.pdf.

[26] G. G. Raffelt. *Stars as Laboratories for Fundamental Physics*. The University of Chicago Press, 1996.

[27] T. Donnelly et al. "Do axions exist?" *Physical Review D* 18 (1978), p. 1607. DOI: 10.1103/PhysRevD.18.1607.

[28] J. E. Kim. "Light pseudoscalars, particle physics and cosmology." *Physics Reports* 150.1-2 (1987), pp. 1 –177. DOI: http://dx.doi.org/10.1016/0370-1573(87)90017-2. URL: http://www.sciencedirect.com/science/article/pii/0370157387900172.

[29] J. Beringer et al. "Review of particle physics." *Physical Review D* 86 (2012), p. 010001. DOI: 10.1103/PhysRevD.86.010001.

[30] M. Srednicki. "Axions: past, present, and future." In: *Continuous advances in QCD 2002*. Ed. by M. A. Shifman and M. B. Voloshin. World Scientific Publishing, 2003, pp. 509–520. arXiv:hep-th/0210172 [hep-th].

[31] J. E. Kim. "Weak interaction singlet and strong CP invariance." *Physical Review Letters* 43 (1979), p. 103. DOI: 10.1103/PhysRevLett.43.103.

[32] M. A. Shifman, A. Vainshtein, and V. I. Zakharov. "Can confinement ensure natural CP invariance of strong interactions?" *Nuclear Physics B* 166 (1980), p. 493. DOI: 10.1016/0550-3213(80)90209-6.

[33] A. Zhitnitsky. "On possible suppression of the axion hadron interactions. (in russian)." *Sov.J.Nucl.Phys.* 31.2 (1980), pp. 260–263.

[34] M. Dine, W. Fischler, and M. Srednicki. "A simple solution to the strong CP problem with a harmless axion." *Physics Letters B* 104 (1981), p. 199. DOI: 10.1016/0370-2693(81)90590-6.

[35] M. Srednicki. "Axion couplings to matter. 1. CP conserving parts." *Nulcear Physics B* 260 (1985), p. 689. DOI: 10.1016/0550-3213(85)90054-9.

[36] H. Leutwyler. "The masses of the light quarks." *Physics Letters B* 378.1–4 (1996), pp. 313–318. DOI: 10.1016/0370-2693(96)00386-3. arXiv:hep-ph/9602255 [hep-ph].

[37] D. B. Kaplan. "Opening the Axion Window." *Nuclear Physics B* 260 (1985), p. 215. DOI: 10.1016/0550-3213(85)90319-0.

[38] E. Witten. "Some properties of O(32) superstrings." *Physics Letters B* 149 (1984), pp. 351–356. DOI: 10.1016/0370-2693(84)90422-2.

[39] J. P. Conlon. "The QCD axion and moduli stabilisation." *Journal of High Energy Physics* 0605 (2006), p. 078. DOI: 10.1088/1126-6708/2006/05/078. arXiv:hep-th/0602233 [hep-th].

[40] P. Svrcek and E. Witten. "Axions in string theory." *Journal of High Energy Physics* 0606 (2006), p. 051. DOI: 10.1088/1126-6708/2006/06/051. arXiv:hep-th/0605206 [hep-th].

[41] A. Arvanitaki et al. "String axiverse." *Physical Review D* 81 (2010), p. 123530. DOI: 10.1103/PhysRevD.81.123530. arXiv:0905.4720 [hep-th].

[42] B. S. Acharya, K. Bobkov, and P. Kumar. "An M Theory solution to the strong CP problem and constraints on the axiverse." *Journal of High Energy Physics* 1011 (2010), p. 105. DOI: 10.1007/JHEP11(2010)105. arXiv:1004.5138 [hep-th].

[43] M. Cicoli et al. "The type IIB string axiverse and its low-energy phenomenology." *Journal of High Energy Physics* 1210 (2012), p. 146. DOI: 10.1007/JHEP10(2012)146. arXiv:1206.0819 [hep-th].

[44] A. Ringwald. "Exploring the role of axions and other WISPs in the dark universe." *Physics of the Dark Universe* 1 (2012), pp. 116–135. DOI: 10.1016/j.dark.2012.10.008. arXiv:1210.5081 [hep-ph].

[45] J. Jaeckel and A. Ringwald. "The low-energy frontier of particle physics." *Annual Review of Nuclear and Particle Science* 60 (2010), pp. 405–437. DOI: 10.1146/annurev.nucl.012809.104433. arXiv:1002.0329v1 [hep-ph].

[46] M. Goodsell and A. Ringwald. "Light hidden-sector U(1)s in string compactifications." *Fortschritte der Physik* 58 (2010), pp. 716–720. DOI: 10.1002/prop.201000026. arXiv:1002.1840 [hep-th].

[47] B. Holdom. "Two U(1)'s and epsilon charge shifts." *Physics Letters B* 166 (1986), p. 196. DOI: 10.1016/0370-2693(86)91377-8.

[48] P. Arias, J. Jaeckel, J. Redondo, and A. Ringwald. "Optimizing light-shining-through-a-wall experiments for axion and other WISP searches." *Physical Review D* 82 (2010), p. 115018. DOI: 10.1103/PhysRevD.82.115018. arXiv:1009.4875 [hep-ph].

[49] G. Raffelt and L. Stodolsky. "Mixing of the photon with low mass particles." *Physical Review D* 37 (1988), p. 1237. DOI: 10.1103/PhysRevD.37.1237.

[50] Y. Grossman, S. Roy, and J. Zupan. "Effects of initial axion production and photon axion oscillation on type ia supernova dimming." *Physics Letters B* 543 (2002), pp. 23–28. DOI: 10.1016/S0370-2693(02)02448-6. arXiv:hep-ph/0204216 [hep-ph].

[51] K. Ehret et al. "New ALPS results on hidden-sector lightweights." *Physics Letters B* 689.4-5 (May 2010), pp. 149–155. DOI: 10.1016/j.physletb.2010.04.066.

[52] J. W. Brockway, E. D. Carlson, and G. G. Raffelt. "SN1987A gamma-ray limits on the conversion of pseudoscalars." *Physics Letters B* 383 (1996), pp. 439–443. DOI: 10.1016/0370-2693(96)00778-2. arXiv:astro-ph/9605197 [astro-ph].

[53] J. Grifols, E. Masso, and R. Toldra. "Gamma-rays from SN1987A due to pseudoscalar conversion." *Physical Review Letters* 77 (1996), pp. 2372–2375. DOI: 10.1103/PhysRevLett.77.2372. arXiv:astro-ph/9606028 [astro-ph].

[54] E. Arik et al. "Probing eV-scale axions with CAST." *Journal of Cosmology and Astroparticle Physics* 0902 (2009), p. 008. DOI: 10.1088/1475-7516/2009/02/008. arXiv:0810.4482 [hep-ex].

[55] M. Arik et al. "Search for sub-eV mass solar axions by the CERN Axion Solar Telescope with ^{3}He buffer gas." *Physical Review Letters* 107 (26 Dec. 2011), p. 261302. DOI: 10.1103/PhysRevLett.107.261302.

[56] K. Barth et al. "CAST constraints on the axion-electron coupling." *Journal of Cosmology and Astroparticle Physics* 2013.05 (2013), p. 010. URL: http://stacks.iop.org/1475-7516/2013/i=05/a=010.

[57] S. Asztalos et al. "A SQUID-based microwave cavity search for dark-matter axions." *Physical Review Letters* 104 (2010), p. 041301. DOI: 10.1103/PhysRevLett.104.041301. arXiv:0910.5914 [astro-ph.CO].

[58] J. Isern, E. García-Berro, S. Torres, and S. Catalán. "Axions and the cooling of white dwarf stars." *The Astrophysical Journal Letters* 682 (Aug. 2008), pp. L109–L112. DOI: 10.1086/591042. arXiv:0806.2807.

[59] M. Meyer, D. Horns, and M. Raue. "First lower limits on the photon-axion-like particle coupling from very high energy gamma-ray observation." *Physical Review D* 87 (3 Feb. 2013), p. 035027. DOI: 10.1103/PhysRevD.87.035027. arXiv:1302.1208 [astro-ph.HE].

[60] D. Bartlett and S. Loegl. "Limits on an electromagnetic fifth force." *Physical Review Letters* 61 (1988), pp. 2285–2287. DOI: 10.1103/PhysRevLett.61.2285.

[61] J. Jaeckel, J. Redondo, and A. Ringwald. "Signatures of a hidden cosmic microwave background." *Physical Review Letters* 101.13 (Sept. 2008), p. 131801. DOI: 10.1103/PhysRevLett.101.131801. arXiv:0804.4157v1 [astro-ph].

[62] A. Mirizzi, J. Redondo, and G. Sigl. "Microwave background constraints on mixing of photons with hidden photons." *Journal of Cosmology and Astroparticle Physics* 0903 (2009), p. 026. DOI: 10.1088/1475-7516/2009/03/026. arXiv:0901.0014 [hep-ph].

[63] P. Arias et al. "WISPy cold dark matter." *Journal of Cosmology and Astroparticle Physics* 1206 (2012), p. 013. DOI: 10.1088/1475-7516/2012/06/013. arXiv:1201.5902 [hep-ph].

[64] H. An, M. Pospelov, and J. Pradler. "New stellar constraints on dark photons" (2013). arXiv:1302.3884 [hep-ph].

[65] J. Redondo and G. Raffelt. "Solar constraints on hidden photons revisited" (2013). arXiv:1305.2920 [hep-ph].

[66] J. Redondo and A. Ringwald. "Light shining through walls." *Contemporary Physics* 52 (Nov. 2010), pp. 211–236. DOI: 10.1080/00107514.2011.563516. arXiv:1011.3741v1 [hep-ph].

[67] P. Ade et al. "Planck 2013 results. XVI. Cosmological parameters" (2013). Submitted to A&A. arXiv:1303.5076 [astro-ph.CO].

[68] E. Aprile. "The XENON1T dark matter search experiment" (2012). arXiv:1206.6288 [astro-ph.IM].

[69] G. Bertone. "The moment of truth for WIMP Dark Matter." *Nature* 468 (2010), pp. 389–393. DOI: 10.1038/nature09509. arXiv:1011.3532 [astro-ph.CO].

[70] P. Sikivie. "Axion cosmology." In: *Axions*. Ed. by M. Kuster, G. Raffelt, and B. Beltrán. Vol. 741. Lecture Notes in Physics. Springer Berlin Heidelberg, 2008. Chap. 2, pp. 19–50. DOI: 10.1007/978-3-540-73518-2_2.

[71] R. Catena and P. Ullio. "A novel determination of the local dark matter density." *Journal of Cosmology and Astroparticle Physics* 1008 (2010), p. 004. DOI: 10.1088/1475-7516/2010/08/004. arXiv:0907.0018 [astro-ph.CO].

[72] P. Sikivie. "Experimental tests of the invisible axion." *Physical Review Letters* 51 (1983). Erratum ibid. 52 (1984) 695, p. 1415. DOI: 10.1103/PhysRevLett.51.1415.

[73] S. De Panfilis et al. "Limits on the abundance and coupling of cosmic axions at $4.5 < m_a < 5\mu$eV." *Physical Review Letters* 59 (1987), p. 839. DOI: 10.1103/PhysRevLett.59.839.

[74] W. Wuensch et al. "Results of a laboratory search for cosmic axions and other weakly coupled light particles." *Physical Review D* 40 (1989), p. 3153. DOI: 10.1103/PhysRevD.40.3153.

[75] C. Hagmann, P. Sikivie, N. Sullivan, and D. Tanner. "Results from a search for cosmic axions." *Physical Review D* 42 (1990), pp. 1297–1300. DOI: 10.1103/PhysRevD.42.1297.

[76] S. J. Asztalos et al. "Large scale microwave cavity search for dark matter axions." *Physical Review D* 64 (2001), p. 092003. DOI: 10.1103/PhysRevD.64.092003.

[77] D. Horns et al. "Searching for WISPy cold dark matter with a dish antenna." *Journal of Cosmology and Astroparticle Physics* 1304 (2013), p. 016. DOI: 10.1088/1475-7516/2013/04/016. arXiv:1212.2970 [hep-ph].

[78] A. Mirizzi, J. Redondo, and G. Sigl. "Constraining resonant photon-axion conversions in the Early Universe." *Journal of Cosmology and Astroparticle Physics* 0908 (2009), p. 001. DOI: 10.1088/1475-7516/2009/08/001. arXiv:0905.4865 [hep-ph].

[79] K. Ichikawa, T. Sekiguchi, and T. Takahashi. "Probing the effective number of neutrino species with cosmic microwave background." *Physical Review D* 78 (2008), p. 083526. DOI: 10.1103/PhysRevD.78.083526. arXiv:0803.0889 [astro-ph].

[80] S. Hannestad, A. Mirizzi, and G. Raffelt. "New cosmological mass limit on thermal relic axions." *Journal of Cosmology and Astroparticle Physics* 0507 (2005), p. 002. DOI: 10.1088/1475-7516/2005/07/002. arXiv:hep-ph/0504059 [hep-ph].

[81] A. Melchiorri, O. Mena, and A. Slosar. "Improved cosmological bound on the thermal axion mass." *Physical Review D* 76 (4 Aug. 2007), p. 041303. DOI: 10.1103/PhysRevD.76.041303.

[82] S. Hannestad, A. Mirizzi, G. G. Raffelt, and Y. Y. Wong. "Cosmological constraints on neutrino plus axion hot dark matter." *Journal of Cosmology and Astroparticle Physics* 0708 (2007), p. 015. DOI: 10.1088/1475-7516/2007/08/015. arXiv:0706.4198 [astro-ph].

[83] P. Gondolo and G. Raffelt. "Solar neutrino limit on axions and keV-mass bosons." *Physical Review D* 79 (2009), p. 107301. DOI: 10.1103/PhysRevD.79.107301. arXiv:0807.2926 [astro-ph].

[84] A. Friedland, M. Giannotti, and M. Wise. "Constraining the axion-photon coupling with massive stars." *Physical Review Letters* 110 (2013), p. 061101. DOI: 10.1103/PhysRevLett.110.061101. arXiv:1210.1271 [hep-ph].

[85] D. Lazarus et al. "A search for solar axions." *Physical Review Letters* 69 (1992), pp. 2333–2336. DOI: 10.1103/PhysRevLett.69.2333.

[86] S. Moriyama et al. "Direct search for solar axions by using strong magnetic field and x-ray detectors." *Physics Letters B* 434 (1998), p. 147. DOI: 10.1016/S0370-2693(98)00766-7. arXiv:hep-ex/9805026 [hep-ex].

[87] Y. Inoue et al. "Search for sub-electronvolt solar axions using coherent conversion of axions into photons in magnetic field and gas helium." *Physics Letters B* 536 (2002), pp. 18–23. DOI: 10.1016/S0370-2693(02)01822-1. arXiv:astro-ph/0204388 [astro-ph].

[88] Y. Inoue et al. "Search for solar axions with mass around 1 eV using coherent conversion of axions into photons." *Physics Letters B* 668 (2008), pp. 93–97. DOI: 10.1016/j.physletb.2008.08.020. arXiv:0806.2230 [astro-ph].

[89] K. Zioutas et al. "First results from the CERN Axion Solar Telescope (CAST)." *Physical Review Letters* 94 (2005), p. 121301. DOI: 10.1103/PhysRevLett.94.121301. arXiv:hep-ex/0411033 [hep-ex].

[90] J. Redondo. "Helioscope bounds on hidden sector photons." *Journal of Cosmology and Astroparticle Physics* 0807 (2008), p. 008. DOI: 10.1088/1475-7516/2008/07/008. arXiv:0801.1527 [hep-ph].

[91] M. Schwarz et al. "Solar hidden photon search." In: *Axions, WIMPs and WISPs*. Ed. by M. Schumann and K. Zioutas. Proceedings, 7th Patras Workshop, PATRAS 2011. June 2011, pp. 129–132. DOI: 10.3204/DESY-PROC-2011-04/schwarz_matthias. arXiv:1111.5797 [astro-ph.IM].

[92] T. Mizumoto et al. "Experimental search for solar hidden photons in the eV energy range using kinetic mixing with photons." *Journal of Cosmology and Astroparticle Physics* 07 (2013), p. 013. DOI: 10.1088/1475-7516/2013/07/013. arXiv:1302.1000 [astro-ph.SR].

[93] K. Arisaka et al. "Expected sensitivity to galactic/solar axions and bosonic super-WIMPs based on the axio-electric effect in liquid xenon dark matter detectors." *Astroparticle Physics* 44 (2013), pp. 59–67. DOI: 10.1016/j.astropartphys.2012.12.009. arXiv:1209.3810 [astro-ph.CO].

[94] G. G. Raffelt. "Astrophysical axion bounds." In: *Axions*. Ed. by M. Kuster, G. Raffelt, and B. Beltrán. Vol. 741. Lecture Notes in Physics. Springer Berlin Heidelberg, 2008, pp. 51–71. DOI: 10.1007/978-3-540-73518-2_3.

[95] H. Schlattl, A. Weiss, and G. Raffelt. "Helioseismological constraint on solar axion emission." *Astroparticle Physics* 10 (1999), pp. 353–359. DOI: 10.1016/S0927-6505(98)00063-2. arXiv:hep-ph/9807476 [hep-ph].

[96] M. Ahlers, J. Jaeckel, J. Redondo, and A. Ringwald. "Probing hidden sector photons through the Higgs window." *Physical Review D* 78.7 (Oct. 2008), p. 075005. DOI: 10.1103/PhysRevD.78.075005. arXiv:0807.4143v2 [hep-ph].

[97] F. Hoogeveen and T. Ziegenhagen. "Production and detection of light bosons using optical resonators." *Nuclear Physics B* 358 (1991), pp. 3–26. DOI: 10.1016/0550-3213(91)90528-6.

[98] P. Sikivie, D. Tanner, and K. van Bibber. "Resonantly enhanced axion-photon regeneration." *Physical Review Letters* 98 (2007), p. 172002. DOI: 10.1103/PhysRevLett.98.172002. arXiv:hep-ph/0701198 [HEP-PH].

[99] A. S. Chou et al. "Search for axion-like particles using a variable baseline photon regeneration technique." *Physical Review Letters* 100 (2008), p. 080402. DOI: 10.1103/PhysRevLett.100.080402. arXiv:0710.3783 [hep-ex].

[100] A. Afanasev et al. "New experimental limit on optical photon coupling to neutral, scalar bosons." *Physical Review Letters* 101 (2008), p. 120401. DOI: 10.1103/PhysRevLett.101.120401. arXiv:0806.2631 [hep-ex].

[101] C. Robilliard et al. "No light shining through a wall." *Physical Review Letters* 99 (2007), p. 190403. DOI: 10.1103/PhysRevLett.99.190403. arXiv:0707.1296 [hep-ex].

[102] P. Pugnat et al. "First results from the OSQAR photon regeneration experiment: no light shining through a wall." *Physical Review D* 78 (2008), p. 092003. DOI: 10.1103/PhysRevD.78.092003. arXiv:0712.3362 [hep-ex].

[103] P. Pugnat et al. "Results and perspectives for laboratory search of weakly interacting sub-eV particles with the OSQAR experiment" (2013). arXiv:1306.0443 [hep-ex].

[104] K. Ehret et al. "Resonant laser power build-up in ALPS – a "light-shining-through-walls" experiment." *Nuclear Instruments and Methods A* 612.1 (May 2009), pp. 83 –96. DOI: http://dx.doi.org/10.1016/j.nima.2009.10.102. arXiv:0905.4159v1 [physics.ins-det].

[105] M. Betz and F. Caspers. "A microwave paraphoton and axion detection experiment with 300 dB electromagnetic shielding at 3 GHz." In: *Proceedings of 3rd International Conference on Particle accelerator (IPAC 2012)*. Ed. by V. Suller. IEEE, 2012, pp. 3320–3322. arXiv:1207.3275 [physics.ins-det].

[106] S. L. Adler. "Photon splitting and photon dispersion in a strong magnetic field." *Annals of Physics* 67 (1971), pp. 599–647. DOI: 10.1016/0003-4916(71)90154-0.

[107] L. Maiani, R. Petronzio, and E. Zavattini. "Effects of nearly massless, spin zero particles on light propagation in a magnetic field." *Physics Letters B* 175 (1986), p. 359. DOI: 10.1016/0370-2693(86)90869-5.

[108] Y. Semertzidis et al. "Limits on the production of light scalar and pseudoscalar particles." *Physical Review Letters* 64 (1990), pp. 2988–2991. DOI: 10.1103/PhysRevLett.64.2988.

[109] R. Cameron et al. "Search for nearly massless, weakly coupled particles by optical techniques." *Physical Review D* 47 (1993), pp. 3707–3725. DOI: 10.1103/PhysRevD.47.3707.

[110] E. Zavattini et al. "Experimental observation of optical rotation generated in vacuum by a magnetic field." *Physical Review Letters* 96 (2006). Erratum ibid. 99(2007)129901(E), p. 110406. DOI: 10.1103/PhysRevLett.96.110406. arXiv:hep-ex/0507107 [hep-ex].

[111] E. Zavattini et al. "New PVLAS results and limits on magnetically induced optical rotation and ellipticity in vacuum." *Physical Review D* 77 (2008), p. 032006. DOI: 10.1103/PhysRevD.77.032006. arXiv:0706.3419 [hep-ex].

[112] E. Williams, J. Faller, and H. Hill. "New experimental test of Coulomb's law: A laboratory upper limit on the photon rest mass." *Physical Review Letters* 26 (1971), pp. 721–724. DOI: 10.1103/PhysRevLett.26.721.

[113] E. Carlson. "Pseudoscalar conversion and x-rays from stars." *Physics Letters B* 344 (1995), pp. 245–251. DOI: 10.1016/0370-2693(94)01529-L.

[114] B. W. Carroll and D. A. Ostlie. *An Introduction to Modern Astrophysics*. Ed. by A. R. S. Black. 2nd ed. Pearson Education, 2007.

[115] J. Binney and M. Merrifield. *Galactic Astronomy*. Princeton University Press, 1998.

[116] R. Townsend. *EZ-Web*. Last accessed: August, 18 2013. URL: http://www.astro.wisc.edu/~townsend/static.php?ref=ez-web.

[117] B. Paxton. "EZ to evolve ZAMS stars: A program derived from Eggleton's stellar evolution code." *Publications of the Astronomical Society of the Pacific* 116.821 (2004), pp. 699–701. DOI: 10.1086/422345. URL: http://www.jstor.org/stable/10.1086/422345.

[118] P. P. Eggleton. "The evolution of low mass stars." *Monthly Notations of the Royal Astronomical Society* 151 (1971), p. 351.

[119] P. P. Eggleton. "Composition changes during stellar evolution." *Monthly Notations of the Royal Astronomical Society* 156 (1972), p. 361.

[120] P. P. Eggleton. "A numerical treatment of double shell source stars." *Monthly Notations of the Royal Astronomical Society* 163 (1973), p. 279.

[121] P. P. Eggleton, J. Faulkner, and B. P. Flannery. "An approximate equation of state for stellar material." *Astronomy & Astrophysics* 23 (Mar. 1973), p. 325.

[122] CDS. *SIMBAD entry for Betelgeuse*. Last accessed August, 20 2013. URL: http://simbad.u-strasbg.fr/simbad/sim-id?Ident=betelgeuse.

[123] G. M. Harper, A. Brown, and E. F. Guinan. "A new VLA-Hipparcos distance to Betelgeuse and its implications." *The Astronomical Journal* 135.4 (Apr. 2008), pp. 1430–1440. DOI: 10.1088/0004-6256/135/4/1430.

[124] F. van Leeuwen. "Validation of the new Hipparcos reduction." *Astronomy & Astrophysics* 474 (2007), pp. 653–664. DOI: 10.1051/0004-6361:20078357. arXiv:0708.1752 [astro-ph].

[125] G. Perrin et al. "Interferometric observations of the supergiant stars Alpha Orionis and Alpha Herculis with FLUOR at IOTA." *Astronomy & Astrophysics* 418 (2004), pp. 675–685. DOI: 10.1051/0004-6361:20040052. arXiv:astro-ph/0402099 [astro-ph].

[126] M. Hünsch, J. H. M. M. Schmitt, K.-P. Schroder, and F.-J. Zickgraf. "On the X-ray emission from M-type giants." *Astronomy & Astrophysics* 330 (Feb. 1998), pp. 225–231.

[127] S. Mohamed, J. Mackey, and N. Langer. "3D simulations of Betelgeuse's bow shock." *Astronomy & Astrophysics* 541, A1 (May 2012), A1. DOI: 10.1051/0004-6361/201118002. arXiv:1109.1555 [astro-ph.SR].

[128] N. Smith, K. Hinkle, and N. Ryde. "Red supergiants as potential type IIn supernova progenitors: spatially resolved 4.6 μm CO emission around VY CMa and Betelgeuse." *The Astronomical Journal* 137.3 (Mar. 2009), pp. 3558–3573. DOI: 10.1088/0004-6256/137/3/3558. arXiv:0811.3037.

[129] S. Ramírez et al. "Stellar iron abundances at the galactic center." *The Astrophysical Journal* 537.1 (July 2000), pp. 205–220. DOI: 10.1086/309022. eprint: arXiv:astro-ph/0002062.

[130] G. Meynet et al. "The past and future evolution of a star like Betelgeuse." *EAS Publications Series* 60 (Jan. 2013), pp. 17–28. DOI: 10.1051/eas/1360002. URL: http://www.eas-journal.org/article_S1633476060000021.

[131] M. Asplund, N. Grevesse, and A. Sauval. "The new solar abundances - Part I: the observations." *Communications in Asteroseismology* 147 (Jan. 2006), pp. 76–79. DOI: 10.1553/cia147s76.

[132] D. Lambert, J. Brown, K. Hinkle, and H. Johnson. "Carbon, nitrogen, and oxygen abundances in Betelgeuse." *The Astrophysical Journal* 284 (Sept. 1984), pp. 223–237. DOI: 10.1086/162401.

[133] M. C. Weisskopf et al. "An overview of the performance and scientific results from the Chandra x-ray observatory." *Publications of the Astronomical Society of the Pacific* 114.791 (2002), pp. 1–24. URL: http://www.jstor.org/stable/10.1086/338108.

[134] Chandra X-ray Center. *The Chandra Proposers' Observatory Guide*. Last accessed: August, 15 2013. Dec. 2012. URL: http://cxc.harvard.edu/proposer/POG/.

[135] J. Posson-Brown, V. L. Kashyap, D. O. Pease, and J. J. Drake. "Dark supergiant: Chandra's limits on X-rays from Betelgeuse" (Dec. 2007). arXiv:astro-ph/0606387v2 [astro-ph].

[136] G. Feldman and R. Cousins. "Unified approach to the classical statistical analysis of small signals." *Physical Review D* 57.7 (Apr. 1998), pp. 3873–3889. DOI: 10.1103/PhysRevD.57.3873. arXiv:physics/9711021v2 [physics.data-an].

[137] R. Beck and R. Wielebinski. "Magnetic fields in galaxies." In: *Planets, Stars and Stellar Systems*. Ed. by T. D. Oswalt and G. Gilmore. Vol. 5. Springer Netherlands, 2013. Chap. 13, pp. 641–723. DOI: 10.1007/978-94-007-5612-0_13.

[138] R. Beck. "Galactic and extragalactic magnetic fields." In: *HIGH ENERGY GAMMA-RAY ASTRONOMY: Proceedings of the 4th International Meeting on High Energy Gamma-Ray Astronomy*. Ed. by F. A. Aharonian, W. Werner Hofmann, and F. Rieger. Vol. 1085. 1. AIP, 2008, pp. 83–96. DOI: 10.1063/1.3076806. URL: http://link.aip.org/link/?APC/1085/83/1.

[139] X. H. Sun, W. Reich, A. Waelkens, and T. A. Enßlin. "Radio observational constraints on galactic 3D-emission models." *Astronomy & Astrophysics* 477.2 (2008), pp. 573–592. DOI: 10.1051/0004-6361:20078671. arXiv:0711.1572 [astro-ph].

[140] H. Men, K. Ferrière, and J. L. Han. "Observational constraints on models for the interstellar magnetic field in the galactic disk." *Astronomy & Astrophysics* 486 (Aug. 2008), pp. 819–828. DOI: 10.1051/0004-6361:20078683. arXiv:0805.3454.

[141] J.-L. Han, K. Ferriere, and R. Manchester. "The spatial energy spectrum of magnetic fields in our galaxy." *The Astrophysical Journal* 610 (2004), pp. 820–826. DOI: 10.1086/421760. arXiv:astro-ph/0404221 [astro-ph].

[142] A. H. Minter and S. R. Spangler. "Observation of turbulent fluctuations in the interstellar plasma density and magnetic field on spatial scales of 0.01 to 100 parsecs." *The Astrophysical Journal* 458 (Feb. 1996), p. 194. DOI: 10.1086/176803.

[143] E. G. Zweibel and C. Heiles. "Magnetic fields in galaxies and beyond." *Nature* 385 (Jan. 1997), pp. 131–136. DOI: 10.1038/385131a0.

[144] N. Duric. "Equipartition: fact or fiction." IAU Symposium 140 (1990). Ed. by R. Beck, R. Wielebinski, and P. Kronberg, p. 235.

[145] R. J. Rand and S. R. Kulkarni. "The local galactic magnetic field." *The Astrophysical Journal* 343 (Aug. 1989), pp. 760–772. DOI: 10.1086/167747.

[146] J. L. Han et al. "Pulsar rotation measures and the large-scale structure of the galactic magnetic field." *The Astrophysical Journal* 642 (May 2006), pp. 868–881. DOI: 10.1086/501444. arXiv:astro-ph/0601357.

[147] R. Beck. "Galactic and extragalactic magnetic fields." *Space Science Reviews* 99 (Oct. 2001), pp. 243–260. eprint: arXiv:astro-ph/0012402.

[148] X. Sun and W. Reich. "The galactic halo magnetic field revisited." *Research in Astronomy and Astrophysics* 10 (2010), pp. 1287–1297. DOI: 10.1088/1674-4527/10/12/009. arXiv:1010.4394 [astro-ph.GA].

[149] R. Jansson and G. R. Farrar. "The galactic magnetic field." *The Astrophysical Journal Letters* 761 (2012), p. L11. DOI: 10.1088/2041-8205/761/1/L11. arXiv:1210.7820 [astro-ph.GA].

[150] NASA / JPL-Caltech / R. Hurt (SSC-Caltech). *Annotated Roadmap of the Milky Way*. Last accessed: August, 16. 2013. NASA, 2008. URL: http://www.spitzer.caltech.edu/images/1925-ssc2008-10b-A-Roadmap-to-the-Milky-Way-Annotated-.

[151] C. Heiles. "A comprehensive view of the galactic magnetic field, especially near the Sun." In: *Polarimetry of the Interstellar Medium*. Ed. by W. G. Roberge and D. C. B. Whittet. Vol. 97. Astronomical Society of the Pacific Conference Series. 1996, p. 457.

[152] Y. Xu et al. "On the nature of the local spiral arm of the Milky Way." *The Astrophysical Journal* 769 (2013), p. 15. DOI: 10.1088/0004-637X/769/1/15. arXiv:1304.0526 [astro-ph.GA].

[153] J. M. Cordes and T. Lazio. "NE2001. 1. A new model for the galactic distribution of free electrons and its fluctuations" (2002). arXiv:astro-ph/0207156 [astro-ph].

[154] S. A. Lamb, I. Iben Jr., and W. M. Howard. "On the evolution of massive stars through the core carbon-burning phase." *The Astrophysical Journal* 207 (July 1976), pp. 209–232. DOI: 10.1086/154486.

[155] K. Mukai. *PIMMS - Portable, Interactive Multi-Mission Simulator version 4.6b*. Last accessed: August, 19 2013. Jan. 2013. URL: https://heasarc.gsfc.nasa.gov/docs/software/tools/pimms.html.

[156] A. Levine et al. "The HEAO 1 A-4 catalog of high-energy X-ray sources." *The Astrophysical Journal Supplement Series* 54 (Apr. 1984), pp. 581–617. DOI: 10.1086/190944.

[157] S. B. Gudennavar, S. G. Bubbly, K. Preethi, and J. Murthy. "A compilation of interstellar column densities." *The Astrophysical Journal Supplement Series* 199.1, 8 (Mar. 2012), p. 8. DOI: 10.1088/0067-0049/199/1/8.

[158] F. Harrison et al. "The Nuclear Spectroscopic Telescope Array (NuSTAR) high-energy x-ray mission." *The Astrophysical Journal* 770, 103 (June 2013), p. 103. DOI: 10.1088/0004-637X/770/2/103. arXiv:1301.7307 [astro-ph.IM].

[159] Princeton Instruments. *PIXIS: 1024*. Last accessed: August, 27 2013. Aug. 2012. URL: http://www.princetoninstruments.com/Uploads/Princeton/Documents/Datasheets/PIXIS/Princeton_Instruments_PIXIS_1024_eXcelon_rev_N3_8.21.2012.pdf.

[160] R. Bähre et al. "Any Light Particle Search II – Technical design report." *Journal of Instrumentation* 8.9 (2013), T09001. DOI: 10.1088/1748-0221/8/09/T09001. arXiv:1302.5647 [physics.ins-det]. URL: http://stacks.iop.org/1748-0221/8/i=09/a=T09001.

[161] M. Frede et al. "Fundamental mode, single-frequency laser amplifier for gravitational wave detectors." *Optics Express* 15.2 (2007), pp. 459–465. DOI: 10.1364/OE.15.000459.

[162] K. Ehret et al. "Production and detection of axion-like particles in a HERA dipole magnet: Letter-of-intent for the ALPS experiment" (2007). arXiv:hep-ex/0702023 [HEP-EX].

[163] P. W. Milonni. "Laser principles." In: *Springer Handbook of Atomic, Molecular and Optical Physics*. Ed. by G. W. F. Drake. Springer, 2006. Chap. 70.

[164] A. E. Siegman. *Lasers*. Sausalito: University Science Books, 1986.

[165] E. D. Black. "An introduction to Pound–Drever–Hall laser frequency stabilization." *American Journal of Physics* 69.1 (2001), p. 79. DOI: 10.1119/1.1286663.

[166] E. Morrison, B. J. Meers, D. I. Robertson, and H. Ward. "Automatic alignment of optical interferometers." *Applied Optics* 33.22 (Aug. 1994), pp. 5041–5049. DOI: 10.1364/AO.33.005041. URL: http://ao.osa.org/abstract.cfm?URI=ao-33-22-5041.

[167] J. A. Stone and A. Stejskal. "Using helium as a standard of refractive index: correcting errors in a gas refractometer." *Metrologia* 41.3 (2004), p. 189. URL: http://stacks.iop.org/0026-1394/41/i=3/a=012.

[168] P. A. J. de Korte et al. "TES x-ray calorimeter-array for imaging spectroscopy." In: *X-Ray and Gamma-Ray Telescopes and Instruments for Astronomy*. Vol. 4851. The International Society for Optical Engineering, 2003, pp. 779–789. DOI: 10.1117/12.461170. URL: http://doc.utwente.nl/62301/.

[169] J. Dreyling-Eschweiler et al. "Detecting an infrared photon within an hour – Transition-Edge Detector at ALPS-II" (Sept. 2013). arXiv:1309.5024 [physics.ins-det].

[170] A. E. Lita, A. J. Miller, and S. W. Nam. "Counting near-infrared single-photons with 95% efficiency." *Optics Express* 16.5 (Mar. 2008), pp. 3032–3040. DOI: 10.1364/OE.16.003032.

[171] D. Fukuda et al. "Titanium-based transition-edge photon number resolving detector with 98% detection efficiency with index-matched small-gap fiber coupling." *Optics Express* 19.2 (Jan. 2011), pp. 870–875. DOI: 10.1364/OE.19.000870. URL: http://www.opticsexpress.org/abstract.cfm?URI=oe-19-2-870.

[172] A. J. Miller et al. "Compact cryogenic self-aligning fiber-to-detector coupling with losses below one percent." *Optics Express* 19.10 (May 2011), 9102–9110.

[173] W. Boyle and G. Smith. "Charge coupled semiconductor devices." *Bell System Technical Journal* 49 (1970), pp. 587–593.

[174] G. F. Amelio, M. F. Tompsett, and G. E. Smith. "Experimental verification of the charge coupled device concept." *Bell System Technical Journal* 49.4 (1970), pp. 593–600.

[175] J. Janesick and T. Elliott. "History and advancement of large array scientific CCD imagers." In: *Astronomical CCD Observing and Reduction Techniques*. Ed. by S. Howell. Vol. 23. Astronomical Society of the Pacific Conference Series. 1992, p. 1.

[176] A. Theuwissen. *Solid-State Imaging with Charge-Coupled Devices*. 1st. Kluwer Academic Publishers, 1995. URL: http://books.google.de/books/about/Solid_State_Imaging_with_Charge_Coupled.html?id=2uhUlcuxWiAC&pgis=1.

[177] W. Bludau, A. Onton, and W. Heinke. "Temperature dependence of the band gap of silicon." *Journal of Applied Physics* 45.4 (1974), pp. 1846–1848. DOI: 10.1063/1.1663501. URL: http://link.aip.org/link/?JAP/45/1846/1.

[178] e2v technologies. *CCD47-10 AIMO Back Illuminated Compact Pack High Performance CCD Sensor*. 2006. URL: http://www.e2v.com/products-and-services/high-performance-imaging-solutions/imaging-solutions-cmos-ccd-emccd/datasheets/.

[179] S. Madan, B. Bhaumik, and J. Vasi. "Experimental observation of avalanche multiplication in charge-coupled devices." *IEEE Transactions on Electron Devices* 30.6 (1983), pp. 694–699. DOI: 10.1109/T-ED.1983.21191.

[180] M. Robbins and B. Hadwen. "The noise performance of electron multiplying charge-coupled devices." *IEEE Transactions on Electron Devices* 50.5 (2003), pp. 1227–1232. DOI: 10.1109/TED.2003.813462.

[181] O. Daigle, C. Carignan, and S. Blais-Ouellette. "Faint flux performance of an EMCCD." In: *Society of Photo-Optical Instrumentation Engineers (SPIE) Conference Series*. Vol. 6276. Society of Photo-Optical Instrumentation Engineers (SPIE) Conference Series. July 2006. DOI: 10.1117/12.669433. eprint: arXiv:astro-ph/0606203.

[182] O. Daigle et al. "Extreme faint flux imaging with an EMCCD." *Publications of the Astronomical Society of the Pacific* 121 (Aug. 2009), pp. 866–884. DOI: 10.1086/605449. arXiv:0908.0528v1 [astro-ph.IM].

[183] e2v technologies. *e2v | High Performance Imaging Solutions | Datasheets*. Last accessed: July, 12 2013. URL: http://www.e2v.com/products-and-services/high-performance-imaging-solutions/imaging-solutions-cmos-ccd-emccd/datasheets/.

[184] Princeton Instruments. *Certificate of Performance*. Aug. 2008.

[185] Amprobe Instrument. *Operating Instructions for AMPROBE® Digital Multimeters Models AM-16 AM-17 AM-18*. Last accessed: July, 18 2013. URL: http://content.amprobe.com/manualsA/AM18.pdf.

[186] Thorlabs. "Absorbtive neutral density filters: 400 - 700 nm." In: *Catalog V21*. Last accessed: August, 20 2013. 2011, pp. 828–829. URL: http://www.thorlabs.de/catalogpages/V21/829.PDF.

[187] H. T. Diehl et al. "Characterization of DECam focal plane detectors." *Proc.SPIE Int.Soc.Opt.Eng.* 7021 (2008), p. 702107. DOI: 10.1117/12.790053. URL: http://lss.fnal.gov/archive/preprint/fermilab-conf-08-196-a.shtml.

[188] Andor Technology. *CCD Detectors*. Last accessed: August, 20 2013. Nov. 2003. URL: http://www.lot-qd.de/files/downloads/andor/en/cc_notesccd_deen.pdf.

[189] A. Lindner. Private communication. 2012.

[190] B. Sen, M. Walker, and M. Woodroofe. "On the unified method with nuisance parameters." *Statistica Sinica* 19.1 (2009), pp. 301–314.

[191] C.-S. Chuang and T. L. Lai. "Hybrid resampling methods for confidence intervals." *Statistica Sinica* 10.1 (2000), pp. 1–50.

[192] J. Neyman. "Outline of a theory of statistical estimation based on the classical theory of probability." *Philosophical Transactions of the Royal Society of London. Series A, Mathematical and Physical Sciences* 236.767 (1937), pp. 333–380. URL: http://www.jstor.org/stable/91337.

[193] G. J. Feldman. *Multiple Measurements and Parameters in the Unified Approach*. Talk at FermiLab Workshop on Confidence Limits. May 2000. URL: http://conferences.fnal.gov/cl2k/copies/feldman2.pdf.

[194] C.-S. Chuang and T. L. Lai. "Resampling methods for confidence intervals in group sequential trials." *Biometrika* 85.2 (1998), pp. 317–332. DOI: 10.1093/biomet/85.2.317. URL: http://biomet.oxfordjournals.org/content/85/2/317.abstract.

[195] G. v. Rossum et al. *The Python Language Reference*. Last accessed: August, 27 2013. 2013. URL: http://docs.python.org/2.7/.

[196] T. E. Oliphant. "Python for scientific computing." *Computing in Science & Engineering* 9.3 (2007), pp. 10–20. URL: http://link.aip.org/link/?CSX/9/10/1.

[197] E. Jones, T. Oliphant, P. Peterson, et al. *SciPy: Open source scientific tools for Python*. 2001–2013. URL: http://www.scipy.org/.

[198] S. Behnel et al. "Cython: The best of both worlds." *Computing in Science & Engineering* 13.2 (Mar. 2011), pp. 31 –39. DOI: 10.1109/MCSE.2010.118. URL: http://folk.uio.no/dagss/cython_cise.pdf.

[199] M. Galassi et al. *GNU Scientific Library: Reference Manual*. Network Theory Ltd., Feb. 1, 2003. URL: http://www.gnu.org/software/gsl/.

[200] Princeton Instruments. *Introduction to scientific InGaAs FPA cameras*. 2012. URL: http://www.princetoninstruments.com/Uploads/Princeton/Documents/TechNotes/InGaAs_Tech_Note_Princeton_InstrumentsrevB0.pdf.

Acknowledgments

This work would not have been possible without the help of many people. I want to thank my supervisor Dieter Horns and Axel Lindner for their time and constant support. My study of the CCD was supported by Günter Wiedemann, Matthias Schwarz and Christian Lippe from the Hamburger Sternwarte and Armin Spikofsky from the electronics workshop of the University Hamburg. I am happy that I could contribute to the ALPS-II project and I am thankful for having worked together with the members of the ALPS group. I am grateful to the astroparticle physics group at the University Hamburg for their kind hospitality and Carsten Richter for a large number of refreshing and interesting lunch breaks. I want to thank Babette Döbrich, Friederike Januschek and Axel Lindner for helpful comments and discussions during our regular early-Friday meetings.

For proof-reading of this thesis, I am indebted to Babette Döbrich, Friederike Januschek, Sebastian Krause, Dieter Trines and Anke Vollmer for their valuable comments and corrections.

This research has made use of the SIMBAD database, operated at CDS, Strasbourg, France, and NASA's Astrophysics Data System Bibliographic Services.

My time here in Hamburg would not have been as pleasant as it was if I hadn't met so many kind people. Especially my former flat mate and now good friend Jonas Franke, who helped me many times to feel at home in Hamburg. I also want to thank my family and friends and, above all, my dear Anke. Without her constant support, encouragement and patience, nothing of this would have happened.